

ISSN • 2708-6437 (Online)
• 2708-6429 (Print)

Journal of Engineering Advancements

Editor-in-Chief:

Prof. Dr. Mohammad Mashud

Volume 01 Issue 02



Published by:
SciEn Publishing Group

Journal of Engineering Advancements

Apt. # 6 C-D, House # 191
Road # 9/A, Dhanmondi R/A
Dhaka-1209, Bangladesh

Email: jea@scienpg.com

Website: www.scienpg.com/jea/

Editor-in-Chief

Prof. Dr. Mohammad Mashud
Khulna University of Engineering & Technology
Khulna-9203, Bangladesh.
Tel: +880-41-769468 Ext. 405
Email: mdmashud@me.kuet.ac.bd

Executive Editor

Dr. Md. Arifuzzaman
Khulna University of Engineering & Technology
Khulna-9203, Bangladesh.
Tel: +880-41-769468 Ext. 431
Email: arif48@me.kuet.ac.bd

Journal of Engineering Advancements Editorial Board Member

Dr. Abul Mukid Mohammad Mukaddes
Shahjalal University of Science and Technology
Email: mukaddes1975@gmail.com
Bangladesh

Dr. Chu Chi Ming
University Malaysia Sabah
Email: chrischu@ums.edu.my
Malaysia

Dr. Mohammad H. Rahman
University of Wisconsin-Milwaukee
Email: rahmanmh@uwm.edu
USA

Dr. Sivakumar Kumaresan
University Malaysia Sabah
Email: shiva@ums.edu.my
Malaysia

Dr. Md. Mizanur Rahman
World University of Bangladesh
Email: mizanur.rahman@mte.wub.edu.bd
Bangladesh

Dr. Riaz U. Ahmed
University of Wisconsin-Green Bay
Email: ahmedm@uwgb.edu
USA

Dr. Kazi Mostafijur Rahman
Khulna University of Engineering & Technology
Email: mostafij@me.kuet.ac.bd
Bangladesh

Dr. Md. Rashedul H. Sarker
University of Indianapolis
Email: sarkerm@uindy.edu
USA

Dr. Seock Sam Kim
University Malaysia Sabah
Email: sskim@ums.edu.my
Malaysia

Dr. Sabuj Mallik
University of Derby
Email: s.mallik@derby.ac.uk
UK

Dr. Mohd Suffian Bin Misaran
University Malaysia Sabah
Email: suffian@ums.edu.my
Malaysia

Dr. Zahir Uddin Ahmed
Khulna University of Engineering & Technology
Email: zuahmed@me.kuet.ac.bd
Bangladesh

Dr. Mohammad Ilias Inam
Khulna University of Engineering & Technology
Email: iliasinam@me.kuet.ac.bd
Bangladesh

Dr. Md. Mahfuz Sarwar
AECOM
Email: mahfuzsarwar@yahoo.com
Australia

Dr. Md. Shariful Islam
Khulna University of Engineering & Technology
Email: msislam@me.kuet.ac.bd
Bangladesh

Dr. Md. Abdullah Al Bari
Khulna University of Engineering & Technology
Email: abdullahalbari@me.kuet.ac.bd
Bangladesh



Published in: July 2020
Published by: SciEnPG

Price: Each Issue BDT 200.00 (US\$ 15)

ISSN: 2708-6437 (Online) 2708-6429 (Print)

Journal of Engineering Advancements

Volume 01, Issue 02

July 2020

CONTENTS

Original Articles

01. Numerical Analysis of the Aerodynamic Characteristics of NACA-4312 Airfoil
Md Rhyhanul Islam Pranto and Mohammad Ilias Inam..... 29
02. Effect of Chemical Treatment on the Mechanical Properties of Luffa Fiber Reinforced Epoxy Composite
Dipto Chakrabarti, Md Shariful Islam, Kazi Jubair and Md Rashedul H Sarker..... 37
03. Near-wall and Turbulence Behavior of Swirl Flows through an Aerodynamic Nozzle
Md. Tanvir Khan, Sharif M. Islam, and Zahir U. Ahmed..... 43
04. Thermal Hydraulic Analysis of a Nuclear Reactor due to Loss of Coolant Accident with and without Emergency Core Cooling System
Pronob Deb Nath, Kazi Mostafijur Rahman and Md. Abdullah Al Bari..... 53
05. The Effect of Various Types of Constant and Time Dependent Heating on Human Tissue: A Finite Element Approach
Mridul Sannyal and Abul Mukid Md. Mukaddes..... 61

This page is intentionally left blank.

Journal of Engineering Advancements

Editor-in-Chief

Prof. Dr. Mohammad Mashud

Department of Mechanical Engineering,
Khulna University of Engineering & Technology, Khulna, Bangladesh

Executive Editor

Dr. Md. Arifuzzaman

Department of Mechanical Engineering,
Khulna University of Engineering & Technology, Khulna, Bangladesh



Published by: SciEn Publishing Group

Apt. # 6 C-D, House # 191, Road # 9/A
Dhanmondi, Dhaka-1209, Bangladesh
Email Address: jea@scienpg.com

www.scienpg.com/jea/

This page is intentionally left blank

Numerical Analysis of the Aerodynamic Characteristics of NACA-4312 Airfoil

Md Rhyhanul Islam Pranto, Mohammad Ilias Inam*

Department of Mechanical Engineering, Khulna University of Engineering & Technology, Khulna-9203, BANGLADESH

Received: May 12, 2020, Revised: June 17, 2020, Accepted: June 18, 2020, Available Online: June 24, 2020

ABSTRACT

The aim of the work is to investigate the aerodynamic characteristics such as lift coefficient, drag coefficient, pressure distribution over a surface of an airfoil of NACA-4312. A commercial software ANSYS Fluent was used for these numerical simulations to calculate the aerodynamic characteristics of 2-D NACA-4312 airfoil at different angles of attack (α) at fixed Reynolds number (Re), equal to 5×10^5 . These simulations were solved using two different turbulence models, one was the Standard $k - \epsilon$ model with enhanced wall treatment and other was the SST $k - \omega$ model. Numerical results demonstrate that both models can produce similar results with little deviations. It was observed that both lift and drag coefficient increase at higher angles of attack, however lift coefficient starts to reduce at $\alpha = 13^\circ$ which is known as stalling condition. Numerical results also show that flow separations start at rare edge when the angle of attack is higher than 13° due to the reduction of lift coefficient.

Keywords: Airfoil; CFD; RANS; Lift Coefficient; Drag Coefficient.



This work is licensed under a [Creative Commons Attribution-NonCommercial 4.0 International](https://creativecommons.org/licenses/by-nc/4.0/)

1. Introduction

Aerodynamics is defined as a study of the resulting effects of relative motion between air molecules and body surfaces [1]. Understanding the air flow behavior around a moving body is very important because we can control the air flow to our advantage in the case of aircraft, wind turbine, drone, and many more. Aerodynamics focuses on studying this phenomenon by applying basic physics laws such as Newton's laws and the Navier-Stokes equation. To study the aerodynamic profile of a particular object, it is necessary to define the object's shape, where the airfoil or the wing cross-section is used in the case of an airplane. The cross-section of the typical aircraft wing is an airfoil and is largely responsible for producing the forces that sustain the aircraft in flight [2]. Airfoil is known as the cross-sectional shape of a wing, blade (of a propeller, rotor, or turbine) which is placed in an airstream in order to generate useful aerodynamic forces. An airfoil's aerodynamic profile can be examined in two ways, one experimentally and other computationally. The aerodynamic characteristics of an airfoil are obtained in the experimental method by placing the airfoil (or wing model) in a controlled wind tunnel and recording the velocity and pressure distribution around the airfoil. The same experiment can be done in the computational approach using a CFD code. Both approaches are usually complementary to each other and can help us design a specific purpose for the airfoil [3].

In the early 1800s, it was discovered that a curved surface produces more lift than a similar size flat plate by Sir George Cayley [4]. The most effective way to do this is to use an airfoil. In the Langley two-dimensional low turbulence tunnels tests a considerable amount of airfoil data has been accumulated by National Advisory Committee for Aeronautics (NACA) in the United States. The development of NACA airfoils which are now in common use was started in 1929 with a systematic investigation of a family of airfoils in the Langley variable-density tunnel [5]. Airfoils of this family are designated by numbers having four digits. Experiments were performed to test

different airfoils and to determine the lift and drag coefficient for different airfoils and to report their results. Jacobs et al. (1933) performed a wide variety of experiments comparing the geometric airfoil parameters and angle of attack and wind speed for different NACA airfoils and published the results of the lift and drag coefficient for 78 different NACA airfoils [6]. Since these experiments were carried out in a wind tunnel with a relatively high free-stream turbulence intensity of about 2%, the results are expected to vary from low free-stream turbulence conditions. NACA airfoils have been used extensively as aerodynamic test models. NACA-0012 and NACA-4412 profiles are arguably the most studied airfoils. Ravi et al. [7] predicted numerically a transition model of an incompressible laminar to turbulent flow over NACA-4412 airfoil at Reynolds number of 3×10^6 . Eleni et al. [8] also carried out studies on the variation of lift and drag coefficients from flow around NACA-0012 airfoil at Reynolds number of 3×10^6 for different turbulence models. In addition to the results available for a NACA-0012 and NACA-4412 airfoil profile, a substantial experimental or numerical database is not available for NACA-4312 airfoil. This study is motivated by the need to complement the presently limited body of knowledge for NACA-4312 airfoil. Thus, the present investigation is focused on examining the effect of the Reynolds number and the angle of attack on the performance characteristics of a NACA-4312 airfoil and relating the performance characteristics.

In this study, CFD approach is used to determine the aerodynamic profiles of the NACA-4312 airfoil. The CFD packages contain three main elements which are Pre-processor, Solver and Post-processor [9]. Recently CFD has been the method of choice in the aerospace, automotive and many industrial components. CFD is vastly used in the field of aerodynamics because it is cheaper than experimental process and also gives more accurate results. The transition from the laminar to the turbulent flow phase plays a very important role in simulating the flow over an airfoil. The fluid flow over the airfoil exerts a pressure force perpendicular to the upper and lower

*Corresponding Author Email Address: rhyhanulislam.me21@gmail.com

surfaces along with shear force which is parallel to the surfaces. The resultant of these two forces is the area of interest. The normal component of the force is known as lift force and the force which is acting in the flow direction is known as drag [10].

It was observed from the previous literature review that there is a lack of understanding of the characteristics of NACA-4312 airfoil. In this paper a series of numerical simulations were carried out to analyze the characteristics of NACA-4312 airfoil with cord length of 1000 mm and Reynolds number of 5×10^5 . ANSYS Fluent was used to solve the steady-state RANS (Reynolds Average Navier-Stokes) equation with two different turbulence models.

2. Methodology

2.1 Airfoil

In this paper, NACA-4312 airfoil was selected for the simulations, the profile is shown in Fig. 1. The NACA-4312 airfoil means that it has a maximum camber equal to 4% of the cord which is located at 30% of the cord from the leading edge with a maximum thickness of 12% of the chord. In this paper, cord length was considered 1000 mm. Airfoil was created by ANSYS design modeler by importing coordinate file of NACA-4312.

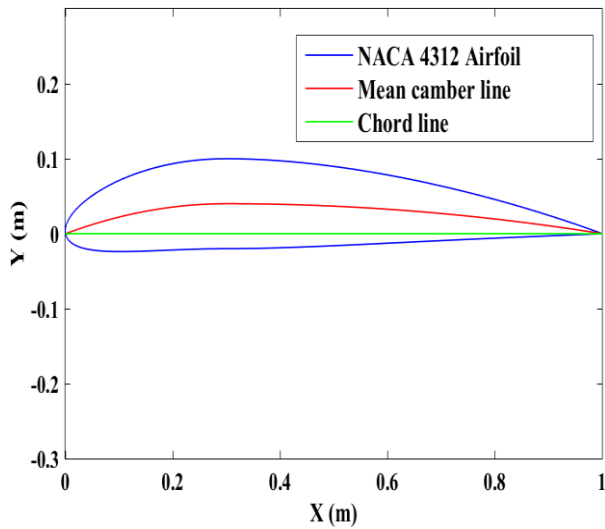


Fig. 1 Geometry of NACA-4312 airfoil.

2.2 Computational Method

These simulations were conducted by ANSYS Fluent. The problem was solved in steady-state with two turbulence models. These simulations were conducted at fixed Reynolds number (Re), equal to 5×10^5 , to show the effect at the transition region [11]. Air was assumed as working medium with a constant density (ρ) and viscosity (μ), whereas $\rho = 1.225 \text{ kg/m}^3$, and $\mu = 1.7894 \times 10^{-5} \text{ kg/ms}$ [12]. The steady-state RANS (Reynolds Average Navier-Stokes) equation was solved using the Green-Gauss cell based gradient option and pressure based solver was selected as the flow is incompressible. The RANS equations are time-averaged equations of motion for fluid flow, as bellows:

$$\frac{\partial}{\partial x_i}(\rho u_i) = 0 \quad (1)$$

$$\begin{aligned} \frac{\partial}{\partial x_j}(\rho u_i u_j) = & \frac{\partial p}{\partial x_i} + \frac{\partial}{\partial x_j} \left[\mu \left(\frac{\partial u_i}{\partial x_j} + \frac{\partial u_j}{\partial x_i} - \frac{2}{3} \delta_{ij} \frac{\partial u_l}{\partial x_l} \right) \right] + \frac{\partial}{\partial x_j} (-\rho \overline{u'_i u'_j}) \end{aligned} \quad (2)$$

where ρ indicates density, u indicates velocity and μ indicates dynamic viscosity of the fluid. The left side of this equation describes the fluid element's mean momentum change to the flow instability and convection by the mean flow. This adjustment is regulated by the mean body force, the isotropic stress due to the mean pressure field, the viscous stresses, and visible stress due to the fluctuating velocity field, commonly referred to as the Reynolds stress ($-\rho \overline{u'_i u'_j}$). This nonlinear stress term requires additional modeling to solve the RANS equations and has resulted in many different turbulence models [13].

In this paper, the Standard $k - \varepsilon$ model and the SST $k - \omega$ model are used to predict the effects of turbulence in flow over the airfoil.

2.2.1 Standard k-ε Model

K-epsilon ($k - \varepsilon$) turbulence model is the most common model used in Computational Fluid Dynamics (CFD) for simulating flow characteristics for turbulent flow conditions. It is a two-equation model, which provides a general definition of turbulence via solving two transport equations (PDEs) one for the turbulence kinetic energy (k) and the other is its dissipation rate (ε) [13]. The turbulent kinetic energy k and dissipation ε are obtained from the following transport equations (3) and (4):

$$\begin{aligned} \frac{\partial}{\partial x_i}(\rho k u_i) = & \frac{\partial}{\partial x_j} \left[\left(\mu + \frac{\mu_t}{\sigma_k} \right) \frac{\partial k}{\partial x_j} \right] + G_k + G_b - \rho \varepsilon - Y_M + S_k \end{aligned} \quad (3)$$

$$\begin{aligned} \frac{\partial}{\partial x_i}(\rho \varepsilon u_i) = & \frac{\partial}{\partial x_j} \left[\left(\mu + \frac{\mu_t}{\sigma_\varepsilon} \right) \frac{\partial \varepsilon}{\partial x_j} \right] \\ & + C_{1\varepsilon} \frac{\varepsilon}{k} (G_k + C_{3\varepsilon} G_b) - C_{2\varepsilon} \rho \frac{\varepsilon^2}{k} + S_\varepsilon \end{aligned} \quad (4)$$

In these equations,

G_k = Generation of turbulence kinetic energy due to mean velocity gradient

Y_M = Fluctuation in compressible turbulence to overall dissipation rate

$C_{1\varepsilon}, C_{2\varepsilon}, C_{3\varepsilon}$ = Constants

$\sigma_k, \sigma_\varepsilon$ = Turbulent Prandtl number for k and ε

S_k, S_ε = User defined source terms

Here turbulent viscosity $\mu_t = \rho C_\mu \frac{k^2}{\varepsilon}$; where is C_μ a constant.

2.2.2 SST k-ω Model

In CFD analysis SST (Shear Stress Transport) $k - \omega$ is a widely used and two-equation eddy-viscosity turbulence model. It provides a general solution for the turbulence kinetic energy (k) and specific dissipation rate of eddy viscosity (ω). This model gives more accurate results in numerical flow

analysis of airfoil than the standard $k - \omega$ turbulence model as it includes transportation of turbulence shear stress. The proper transport behavior can be obtained to the formulation of eddy-viscosity [14]. The turbulent kinetic energy k and dissipation rate of eddy viscosity ω are obtained from the following transport equations (5) and (6):

$$\frac{\partial}{\partial x_i} (\rho k u_i) = \frac{\partial}{\partial x_j} [(\mu + \sigma_k \mu_t) \frac{\partial k}{\partial x_j}] + G_k - Y_k + S_k \quad (5)$$

$$\frac{\partial}{\partial x_i} (\rho \omega u_i) = \frac{\partial}{\partial x_j} [(\mu + \sigma_\omega \mu_t) \frac{\partial \omega}{\partial x_j}] + G_\omega - Y_\omega + S_\omega \quad (6)$$

In these equations,

G_k = Generation of turbulence kinetic energy due to mean velocity gradient

G_ω = Generation of ω

Y_k, Y_ω = The dissipation of k and ω

σ_k, σ_ω = Turbulent Prandtl number for k and ω

S_k, S_ω = User defined source terms

Here turbulent viscosity $\mu_t = \frac{\rho k}{\omega} \frac{1}{\max[\frac{1}{\alpha^*}, \frac{SF_2}{\alpha_1 \omega}]}$; where S is the

strain rate magnitude, F_2 is a constant, and

α = Angle of attack.

2.3 Boundary Condition with domain

For these simulations, a computation domain was created around the NACA-4312 airfoil, shown in Fig. 1. Chord length of NACA-4312 airfoil was assumed to be equal to 1000 mm. To minimize the boundary effect, the domain was extended 12.5C (C indicated chord length) along the upstream and 20C along downstream from the trailing edge, like Fig. 2 [15]. In the domain, airfoil surface was assumed no-slip boundary condition, BAFED was assumed constant velocity inlet and pressure outlet at BCD. For this fixed Re , the inlet velocity u , was assumed to be 7.5 m/s. In these simulation angle of attack (α) was changed by changing flow direction instead of rotating airfoil which produced the same effect on the airfoil. The velocity components along x and y direction were calculated by $u \cos \alpha$ and $u \sin \alpha$, respectively, for different angle of attack (α).

2.4 Mesh generation and Wall Treatment

The C-type structural mesh was created for better convergence and control of the wall function, shown in Fig. 3 and Fig. 4. Fig. 3 depicts the structural meshing with quadrilateral elements which was done by ANSYS Meshing whereas Fig. 4 illustrates the meshing quality around the airfoil profile.

The application of wall functions near the wall region may significantly reduce the processing and storage requirements while producing an acceptable degree of solution. To ensure sufficient boundary layer modeling the inflation was set to 1.15.

The effectiveness of $k - \varepsilon$ model is beyond $y^+ = 30$. The non-dimensional wall parameter is defined as:

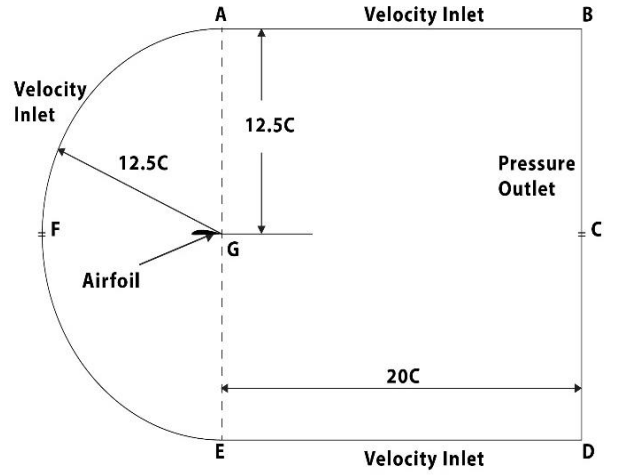


Fig. 2 Computation domain with boundary conditions.

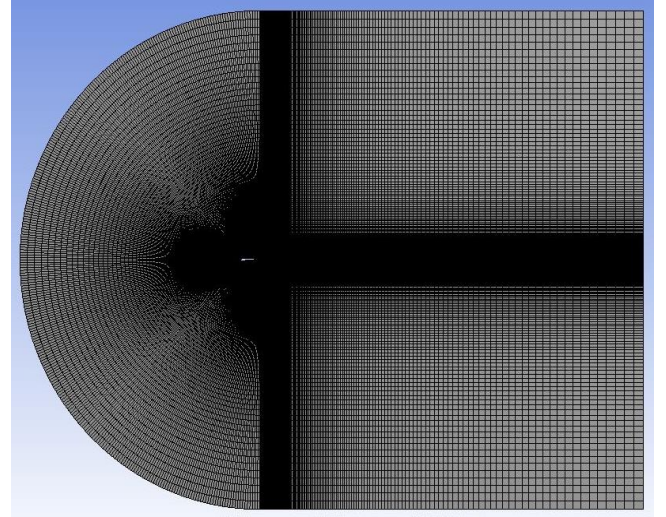


Fig. 3 Mesh among the whole domain.

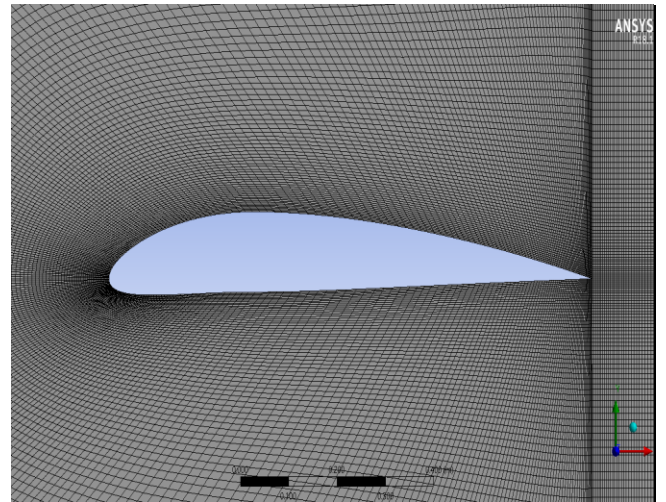


Fig. 4 Mesh around the NACA-4312 airfoil.

$$y^+ = y \times \frac{\sqrt{(\tau\omega / \rho)}}{\mu}$$

Here y is the distance from the wall to the centroid of the first fluid cell. It was observed for all simulations that the value of y^+ was higher than 30 and lower than 60.

2.5 Mesh Independence Test

A series of simulations were conducted for mesh independency tests. A different number of meshes were created by dividing circular and rectangular sections with different numbers. **Fig. 5** depicts the variation of lift coefficient for different numbers of elements of the mesh for an angle of attack 5° . It is observed from figure that meshes with higher than 105000 number of elements can produce accurate results with minimum deviation. As a result mesh with element number 105000 were selected for further simulation.

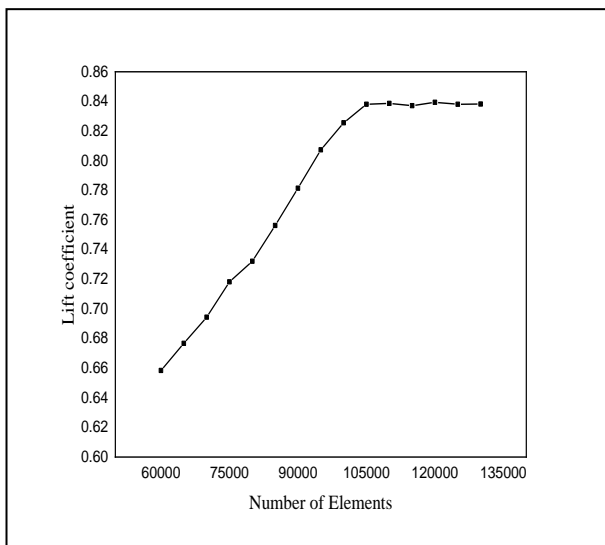


Fig. 5 Variation of coefficient of lift with no. of element.

3. Results and Discussion

Fig. 6 depicts the variation of lift coefficient for different angles of attack for two different turbulence models. It is observed that the lift coefficients are almost equal for both models up to $\alpha = 6^\circ$, however, the SST $k - \omega$ model predicts higher lift coefficient compared to the standard $k - \varepsilon$ model when $\alpha > 6^\circ$. **Fig. 6** also shows that the lift coefficient increases with angle of attack, for both models, up to 12° . Later on, it decreases with α due to the flow separation at the trailing edge, which indicated stalling occurs at the range of $12^\circ \sim 13^\circ$. From 0° angle of attack to 12° angle of attack the lift curve is almost linear.

Fig. 7 shows the effect of the angle of attack (α) on the drag coefficient for two different turbulence method. It is observed that the drag coefficient estimates higher values with the standard $k - \varepsilon$ model compared to the SST $k - \omega$ because of the transportation of the shear viscosity. For both models, the drag coefficient increase with α , however, the increment rate is higher at higher α due to the flow separation at trailing edge. The drag coefficient still increases after the stalling angle however lift coefficient decreases.

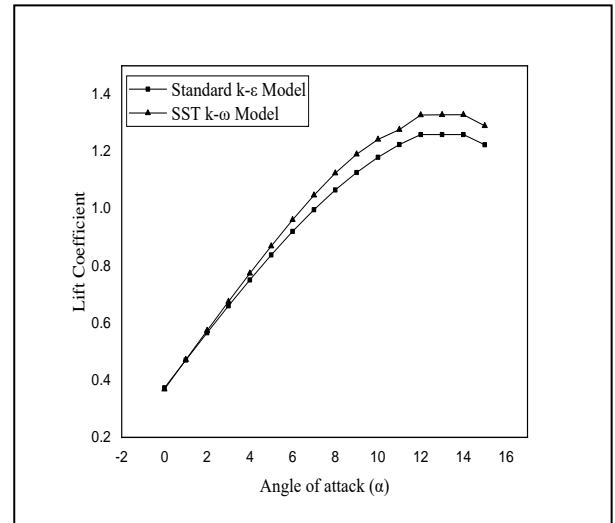


Fig. 6 Lift coefficient vs angle of attack.

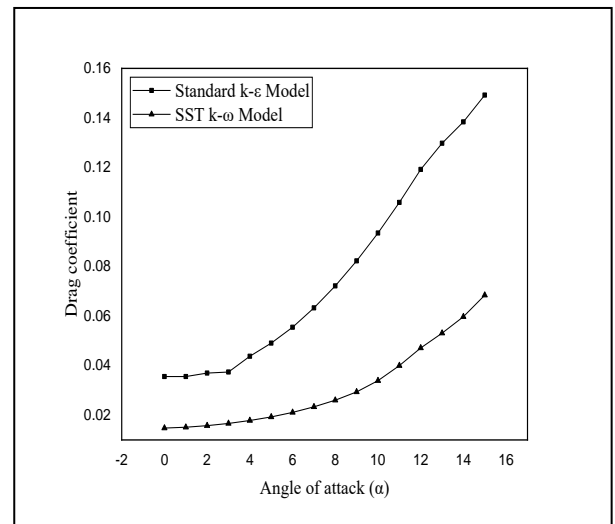


Fig. 7 Drag coefficient vs angle of attack.

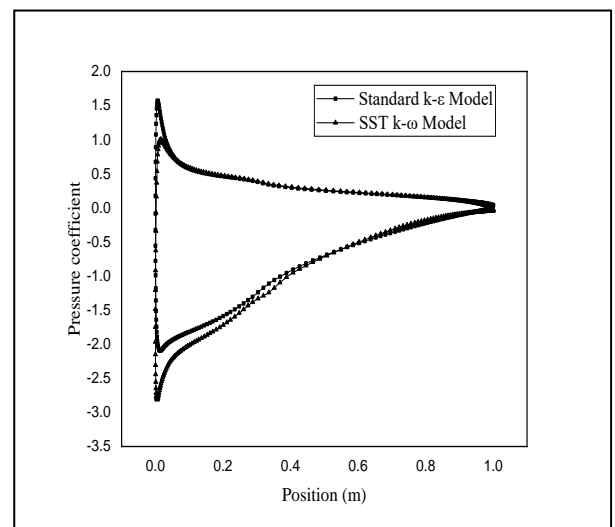


Fig. 8 Pressure coefficient on the airfoil surface at 10° angle of attack.

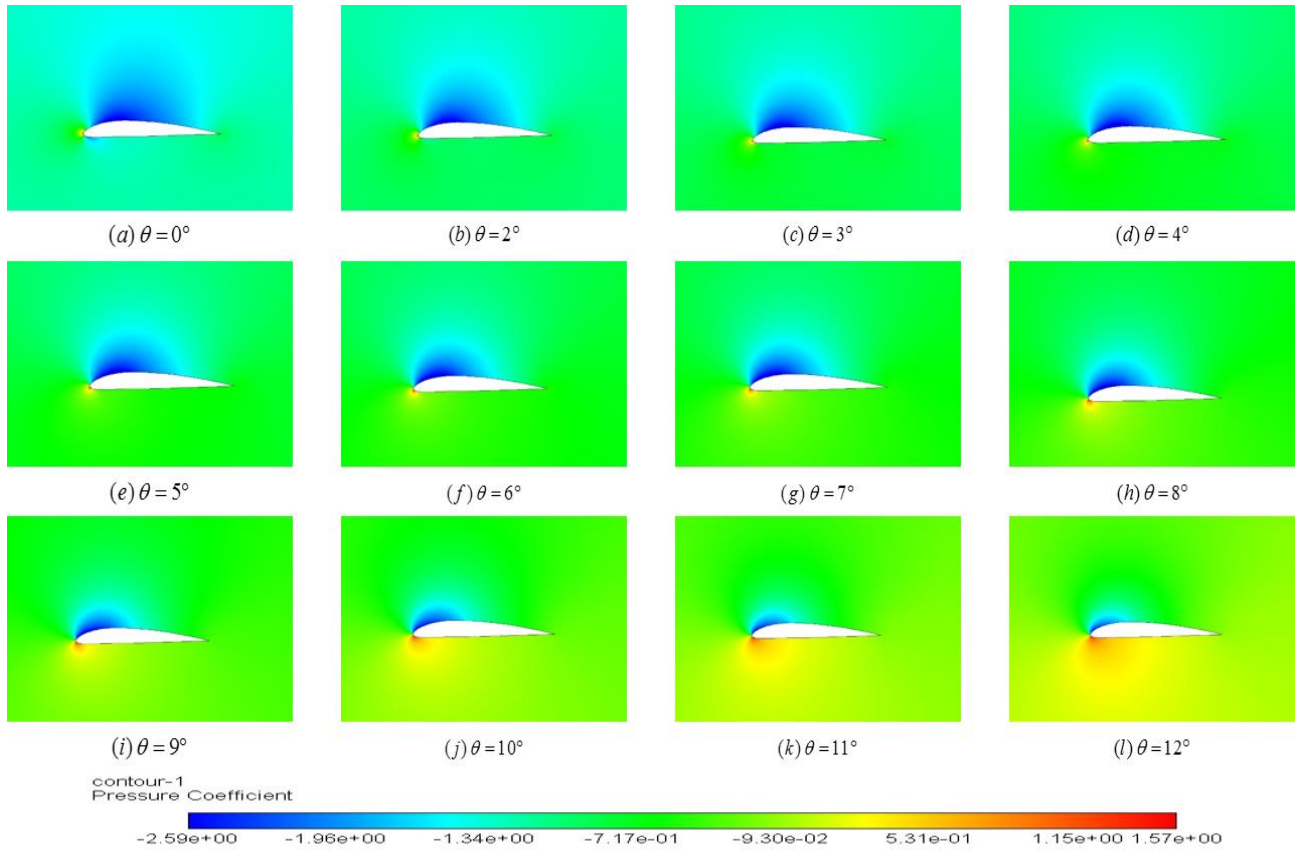


Fig. 9 Contours of pressure with the Standard k- ϵ model for different angles of attack of NACA-4312 airfoil.

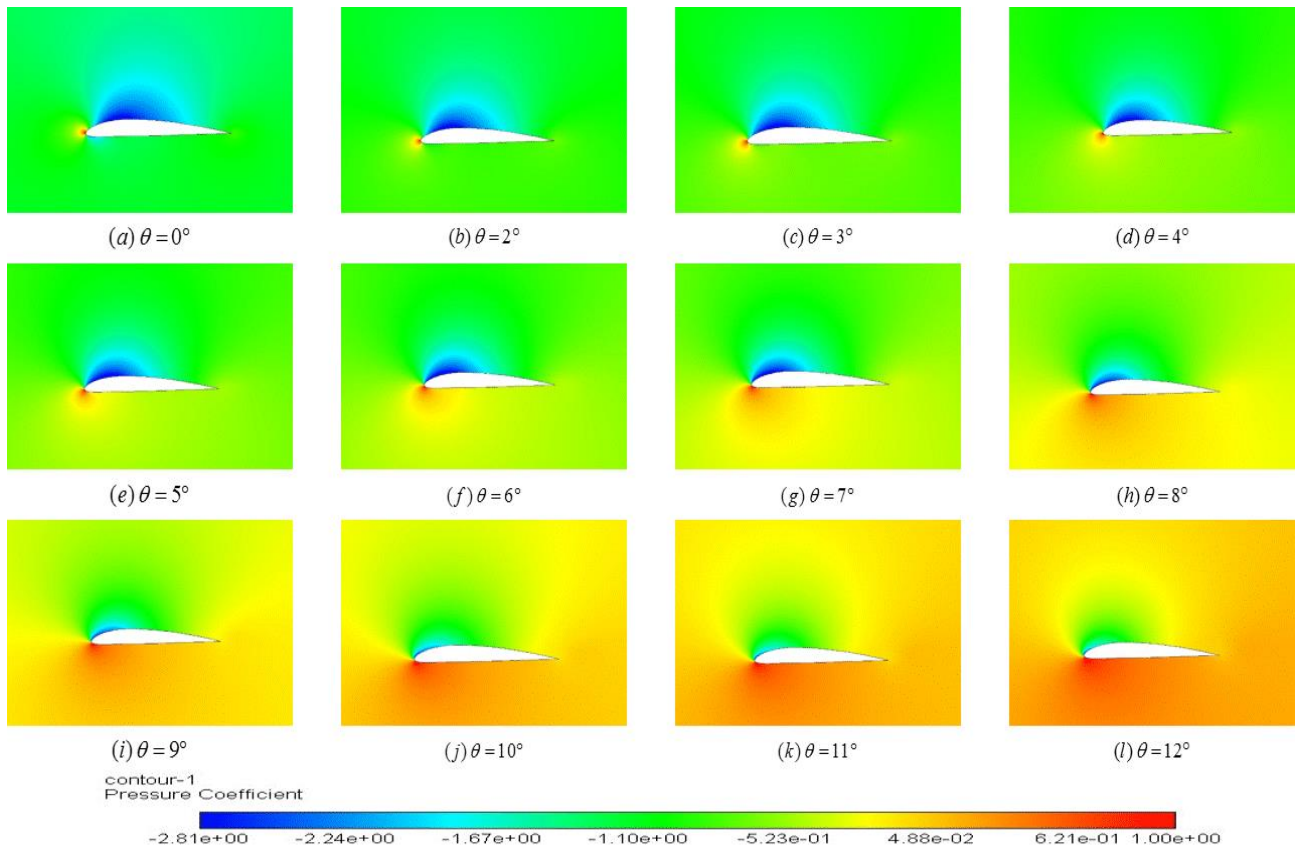


Fig. 10 Contours of pressure with the SST k- ω model for different angles of attack of NACA-4312 airfoil.

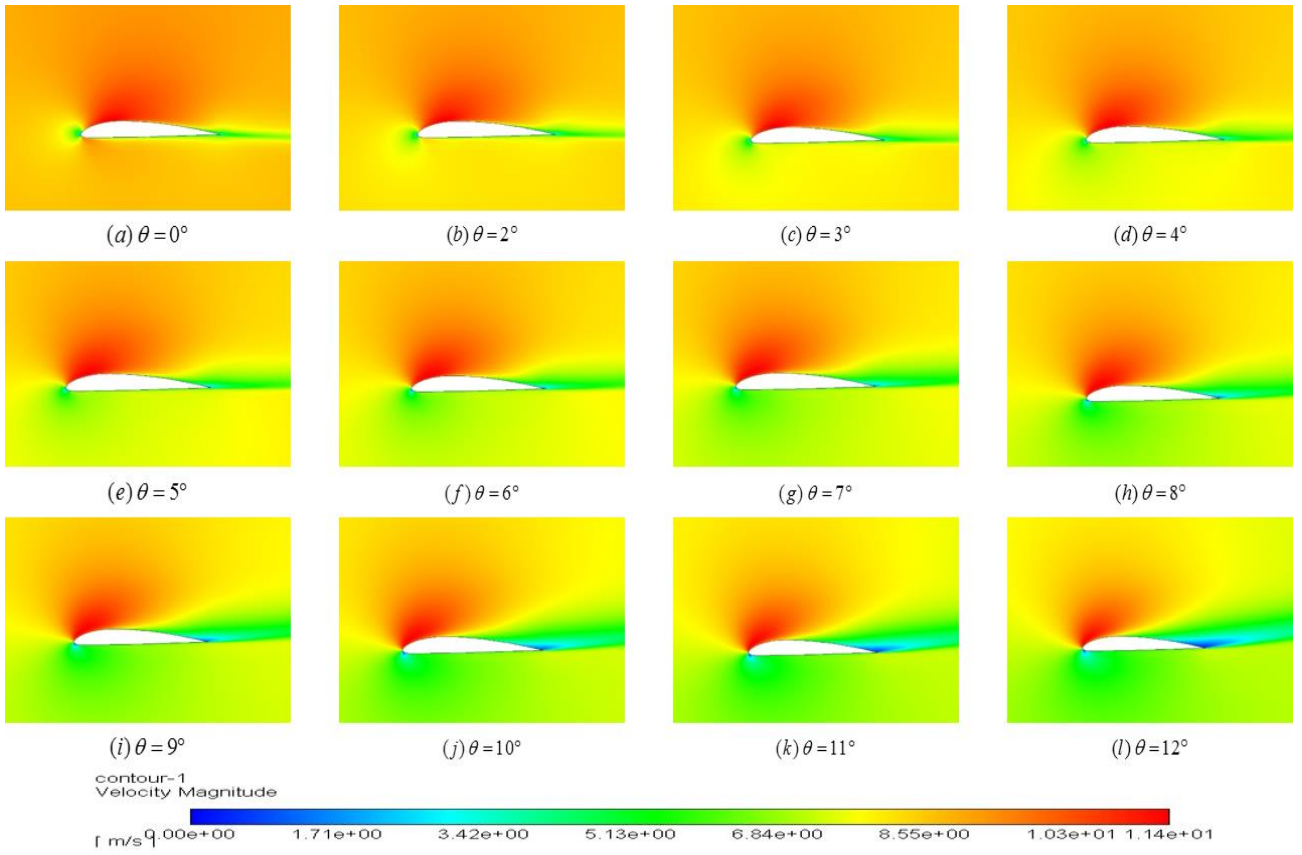


Fig. 11 Velocity contours with the Standard k- ϵ model

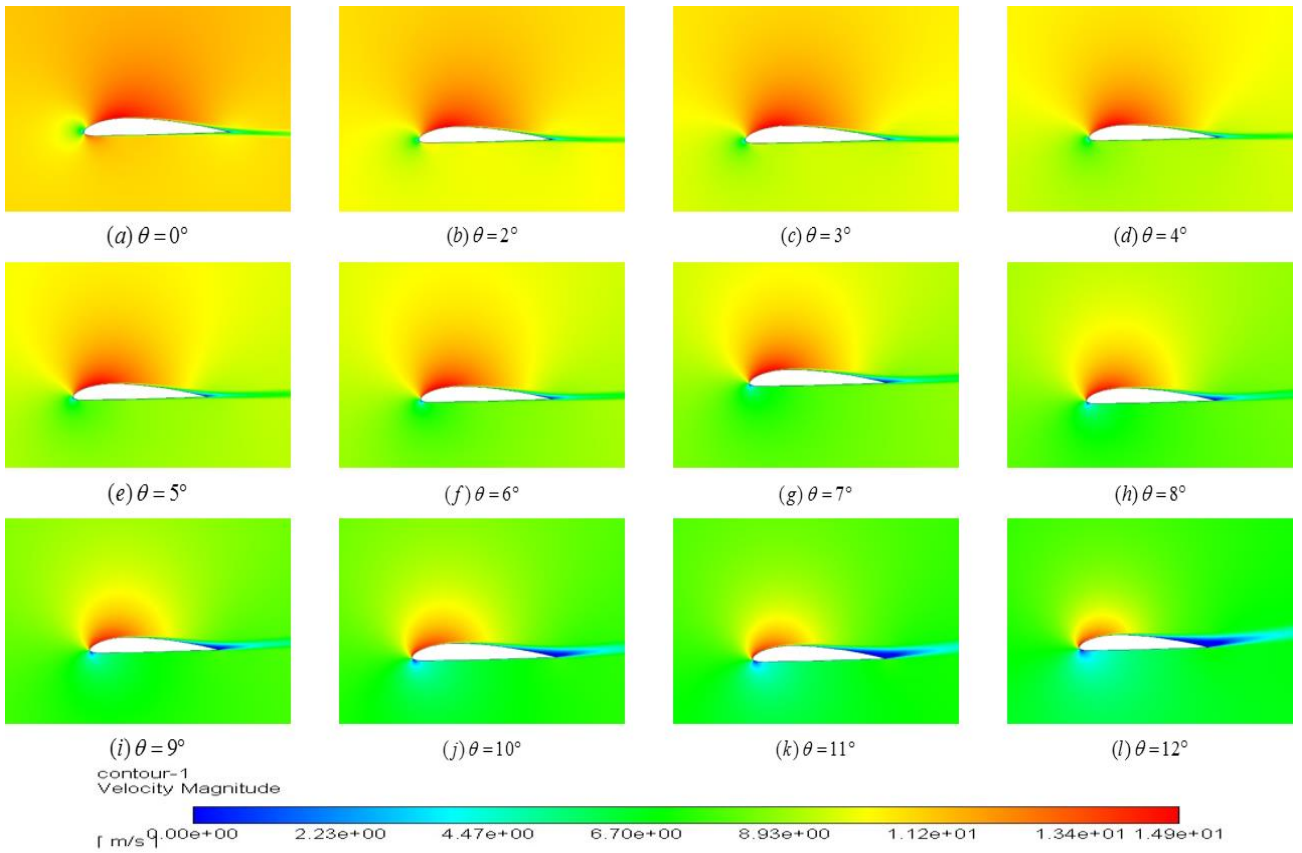


Fig. 12 Velocity contours with the SST k- ω model

Fig. 8 demonstrates pressure distribution on the airfoil surface for both models at an angle of attack $\alpha = 10^\circ$. The upper and lower portion of the graph represent pressure coefficient distribution on the lower surface and upper surface of the airfoil, respectively. It is observed that the upper surface have lower pressure and lower surface have higher pressure which produces lift. Maximum lower and higher pressure observed near to the leading of the lower and upper surface, respectively, which starts to reduce along the trailing edge.

3.1 Pressure Contours

Fig. 9 and **Fig. 10** presents pressure contours for the Standard $k - \varepsilon$ turbulence model and the SST $k - \omega$ turbulence model, respectively, at different angle of attack. In these two figures, the effect of angles of attack is shown by changing the flow directions instead of rotating airfoil, which gives the same effect on airfoil. Similar pressure distribution pattern is observed for the Standard $k - \varepsilon$ and SST $k - \omega$ turbulence model, present in **Fig. 9** and **Fig. 10**, respectively at lower angle of attack, whereas slightly varies in magnitude at higher angle of attack though the pattern of pressure distribution is similar. It is clearly observed from both figures that the upper surface has lower pressure and the lower surface has higher pressure. It is also observed from both figures that negative pressure region on the upper surface which is situated almost around the whole surface which starts to decrease with the increase of angle of attack, however pressure on the lower surfaces increases with angle of attack. Though pressure difference between lower and upper surface increase until flow separates on the upper surface at a certain angle of attack. The lift coefficient increases in both turbulence model with the increase of angle of attack and it reaches the stalling position near 13° angle of attack. Between the two turbulence models, it is observed that the pressure difference in the SST $k - \omega$ model is slightly higher than the Standard $k - \varepsilon$ model which is clearly observed in **Fig. 8** also.

3.2 Velocity Contours

Fig. 11 and **Fig. 12** depict velocity contours for the Standard $k - \varepsilon$ turbulence model and SST $k - \omega$ turbulence model, respectively, at different angles of attack. In these two figures, the effect of angle of attack is shown by changing the flow directions instead of rotating airfoil, which gives the same effect on airfoil. Similar velocity distribution pattern is observed for the Standard $k - \varepsilon$ and SST $k - \omega$ turbulence model, present in **Fig. 11** and **Fig. 12**, respectively at lower angle of attack, whereas slightly varies in magnitude at higher angle of attack though patter of velocity distribution is similar. It is clearly observed from both figures that velocity above the upper is higher than the velocity below the lower surface. This happens due to the Bournollie's principle. It is also observed from both figures that at lower angle of attack flow is attached to upper surface and lower surface as a result there is no zone of zero velocity which indicates flow separation happens. When the angle attack reaches to the value of 10° flow starts to

separate, see **Fig. 11**, at the trailing edges which starts to move towards the leading edges at higher angles of attack. A similar pattern is also observed for the SST $k - \omega$ model, see **Fig. 12**, however, flow separation is identified comparative lower angle of at 8° compare to the Standard $k - \varepsilon$ model. Due to this flow separation, lift coefficient starts to decrease after a certain angle of attack.

4. Conclusion

In this paper aerodynamic characteristics of NACA-4312 airfoil have been studied using ANSYS Fluent by the Standard $k - \varepsilon$ model and SST $k - \omega$ model turbulence model. At lower angles of attack both methods produce similar results however at higher angles of attack results vary in magnitude slightly though nature is similar. It is observed that the lift and drag coefficient increase with angle of attack though the lift coefficient shows a decreasing trend beyond the angle of attack 13° .

References

- [1] Fearn, R.L., 2008. Airfoil aerodynamics using panel methods. *The Mathematica Journal*, 10(4), p.15.
- [2] Triet, N.M., Viet, N.N. and Thang, P.M., 2015. Aerodynamic analysis of aircraft wing. *VNU Journal of Science: Mathematics-Physics*, 31(2).
- [3] Sumaryada, T., Jaya, A.M. and Kartono, A., 2018. Simulating the Aerodynamics Profiles of NACA 4312 Airfoil in Various Incoming Airspeed and Gurney Flap Angle. *Omega: Jurnal Fisika dan Pendidikan Fisika*, 4(1), pp.1-1.
- [4] Ackroyd, J.A.D., 2011. Sir George Cayley: the invention of the aeroplane near Scarborough at the time of Trafalgar. *Journal of Aeronautical History Paper No*, p.6.
- [5] Oppermann, R.H., 1938. National advisory committee for aeronautics: Report No. 624, Two-Dimensional Subsonic Compressible Flow Past Elliptic Cylinders, by Carl Kaplan. 8 pages, illustrations, 23× 29 cms. Washington, Government Printing Office, 1938. Price 10 cents.
- [6] Jacobs, E.N., Ward, K.E. and Pinkerton, R.M., 1933. *The Characteristics of 78 related airfoil section from tests in the Variable-Density Wind Tunnel* (No. 460). US Government Printing Office.
- [7] Ravi, H.C., Madhukeshwara, N. and Kumarappa, S., 2013. Numerical investigation of flow transition for NACA-4412 airfoil using computational fluid dynamics. *International Journal of Innovative Research in Science Engineering and Technology*, 2(7), pp.2778-2785.
- [8] Eleni, D.C., Athanasios, T.I. and Dionissios, M.P., 2012. Evaluation of the turbulence models for the simulation of the flow over a National Advisory Committee for Aeronautics (NACA) 0012 airfoil. *Journal of Mechanical Engineering Research*, 4(3), pp.100-111.
- [9] Versteeg, H.K. and Malalasekera, W., 2007. *An introduction to computational fluid dynamics: the finite volume method*. Pearson education.

- [10] Cengel, Y.A. and Cimbala, J.M., 2012. *Fluid Mechanics Fundamental and Application Third Edition*.
- [11] Incropera, F. P., DeWitt, D. P., Bergman, T. L. and Lavine, A. S., 2007. *Fundamentals of Heat and Mass Transfer(6th edition)*.
- [12] Marshall, J. and Plumb, R.A., 2008. *Atmosphere, ocean and climate dynamics*.
- [13] Launder, B.E., 2015. First steps in modelling turbulence and its origins: a commentary on Reynolds (1895)'On the dynamical theory of incompressible viscous fluids and the determination of the criterion'. *Philosophical Transactions of the Royal Society A: Mathematical, Physical and Engineering Sciences*, 373(2039), p.20140231.
- [14] Menter, F.R., 1994. Two-equation eddy-viscosity turbulence models for engineering applications. *AIAA journal*, 32(8), pp.1598-1605.
- [15] Verhoff, A., Stookesberry, D. and Agrawal, S., 1992. Far-field computational boundary conditions for two-dimensional external flow problems. *AIAA journal*, 30(11), pp.2585-2594.

Effect of Chemical Treatment on the Mechanical Properties of Luffa Fiber Reinforced Epoxy Composite

Dipto Chakrabarti¹, Md Shariful Islam^{1}, Kazi Jubair¹ and Md Rashedul H Sarker²*

¹Department of Mechanical Engineering, Khulna University of Engineering & Technology, Khulna-9203, BANGLADESH

²R.B. Annis School of Engineering, University of Indianapolis, IN 46227, USA

Received: June 13, 2020, Revised: June 23, 2020, Accepted: June 23, 2020, Available Online: June 27, 2020

ABSTRACT

Novel luffa fiber reinforced epoxy composites are prepared and their mechanical properties are investigated before and after chemical treatment. The unique natural knitting structure of luffa provides an excellent reinforcement to the epoxy matrix. Knowing that the fiber-matrix bond gets stronger and imparts more strength to the composite when chemical treatment is done on fibers, composites are manufactured by untreated and treated luffa fiber using epoxy as a matrix. Luffa fiber is treated using benzoyl chloride and NaOH. Tensile and flexural tests are conducted on composites to investigate the effect of chemical treatment. Test results have shown that the chemical treatment on fibers improved the tensile strength, tensile modulus, flexural strength and flexural modulus by 27.21%, 49.37%, 41.84% and 6.44% respectively. Tensile modulus of luffa fiber composite is found to be higher compared with commonly used natural fiber composites. The experimental investigation suggests that, chemically treated luffa fiber reinforced epoxy composites could be a potential lightweight material in various applications.

Keywords: Luffa Fiber; Benzoyl Chloride Treatment; Mechanical Properties; Natural Fiber Composite



This work is licensed under a [Creative Commons Attribution-NonCommercial 4.0 International](https://creativecommons.org/licenses/by-nc/4.0/)

1. Introduction

In the recent time, composite materials have gained huge attention to the researchers due to its superior mechanical properties like strength to weight proportion, crack durability, better physical, chemical and electrical properties etc. [1]-[3]. In composite materials, fibers are used as reinforcement while the matrix conforms the shape of the material which also transfers the load between fibers. Fibers could be synthetic (glass, carbon, nylon etc.) or natural (jute, bamboo, luffa etc.). Although, synthetic fibers have better strength, natural fiber are comparatively cheaper, abundant in nature and renewable sources of fiber [4]. Despite the fact that, the strength of the natural fiber is lower than the synthetic fiber, natural fibers are used in automobile industries and many other products like ball point pen, fishing hook, tennis racket, bicycle etc. [5]-[6].

Previous researchers have studied mechanical properties of different natural fiber reinforced composites with or without fiber surface treatment. Akil et al. studied the water absorption of jute fiber reinforced polyester composites [7]. A.V.R. Prasad and K.M. Rao studied mechanical properties of jowar, sisal and bamboo fiber reinforced composites [8]. A lot of research has been carried out on bamboo fiber reinforced composites by different researchers [9]-[13]. Moisture absorption characteristics of sisal and roselle fiber reinforced hybrid composites were studied by Athijayamani et al. [14]. Dhakal et al. [15] studied the effect of water absorption on the mechanical properties of hemp fiber reinforced composites. Palm and coir fiber reinforced composites were studied by Haque et al. [16].

Luffa cylindrica is a natural fiber of less weight, low cost and useful mechanical property but also has an uncommon

woven form which is exceptional in other natural fibers. Although a lot of research about mechanical properties of natural fiber reinforced composites were found in the literature. However, mechanical properties of luffa fiber reinforced composites are scarce in literature. Different mechanical properties of luffa fiber reinforced composites were studied by N. Mohanta and S.K. Acharya [17]-[18]. In this paper, the tensile and flexural properties of natural Luffa fiber are reported. The effect of NaOH and benzoyl chloride treatment on fiber surface to enhance the mechanical properties of Luffa fiber reinforced polymer composite with four layers of fiber interface is analyzed.

2. Experimental Details

2.1 Materials

Luffa fiber is used as reinforcement and epoxy (LY 556/HY 951 hardener) is used as matrix material. The Luffa cylindrica is collected from local agricultural market of Bangladesh and later, this luffa cylindrica is used to extract luffa fiber as described in section 2.2. The hardener is mixed with resin at a ratio of 1:10 as suggested by the manufacturer. NaOH and Benzoyl chloride are used to treat the fiber surface.

2.2 Fiber Extraction

Luffa fiber is collected out of ripe Luffa (Fig. 1(a)). When Luffa is ripe the xylem fiber network is opened consisting of lignin and cellulose. The natural lignin-cellulose bond is weaker. To form a stronger bond lignin needs to separate out which acts as matrix here. The fiber is separated from lignin-cellulose bond by fermenting in fermented water for 15 days (Fig. 1(b)). The extracted fiber is then dried in atmospheric air (Fig. 1(c)).



Fig. 1 (a) Raw luffa, (b) Fermenting in water and (c) Drying in atmospheric air.

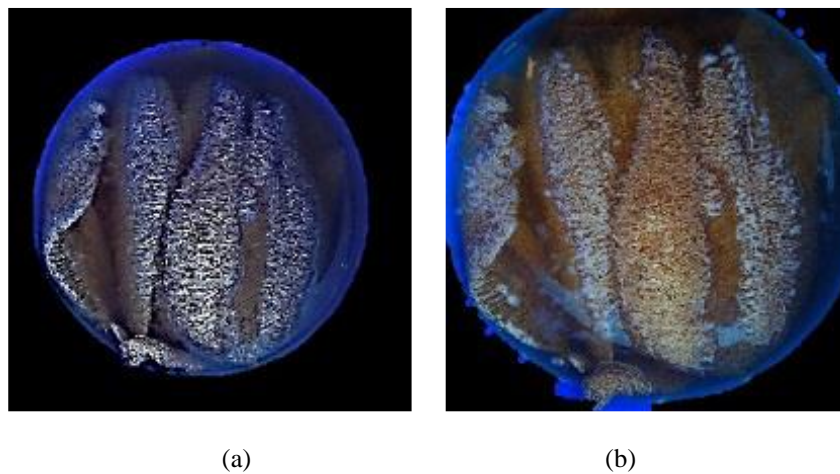


Fig. 2 (a) Fiber mixing with NaOH solution and (b) After 1h the NaOH and fiber mixture

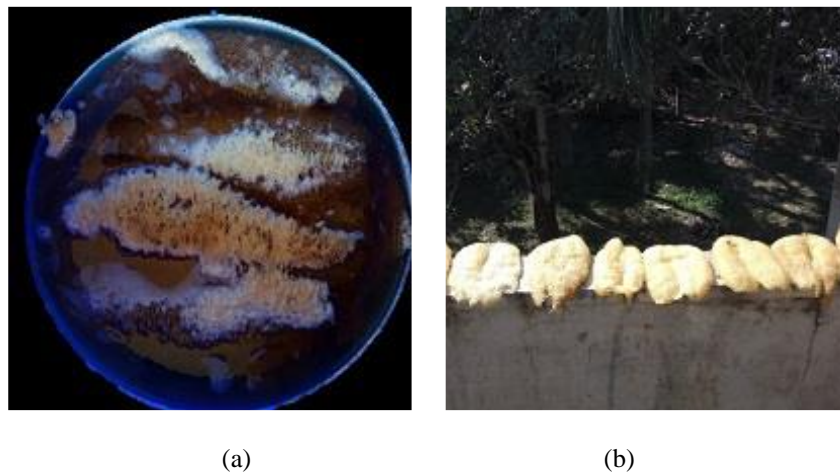


Fig. 3 (a) After 15 minutes continuous stirring the benzoyl chloride and fiber mix and (b) Drying in atmospheric air.

2.3 Chemical Treatment

To enact the hydroxyl bond of the cellulose and lignin, the strands are treated with 10% NaOH for 1 hour as shown in [Fig. 2](#). After that, the strands are kept in benzoyl chloride for 15 minutes with continuous stirring ([Fig. 3](#)). Benzoyl chloride removes the cellulose and lignin bond by creating cellulose and benzoyl chloride bond. The strands are then soaked in ethanol which weakens the benzoyl chloride-cellulose bond. It is necessary to weaken this benzoyl chloride-cellulose bond

because it reduces the fiber matrix interfacial strength. The strands are then washed properly using distilled water to remove any additional ethanol. Finally, the strands are dried in atmospheric air followed by oven drying at 70 °C for 6 hours [\[17\]](#).

2.4 Manufacturing Process

Hand lay-up method is used which is a very effective way to manufacture composite [\[19\]-\[20\]](#). Rectangular aluminum plate with a size of (300 mm × 300 mm) is used as mold plate.

Fig. 4 shows the schematic diagram of the lay-up. At first, the mold release is applied to the mold plate which facilitate the easy removal of composite after curing. The resin hardener mixer is then applied to the mold plate with a soft roller and brush. The first layer of fiber is then placed on the mold plate and applied resin hardener mixer with the brush and roller. The roller ensures uniform distribution of resin hardener mixer on the fiber layer and removes any air bubbles that formed. The next layer of fiber is then placed on top of the first layer and the procedure repeated. Top mold plate is placed on top of the top layer of fiber and a pressure of 100 MPa is applied which ensures the uniform thickness of the manufactured composite. At this stage, the composite is cured at room temperature for 24 hours. In this way, composites are manufactured by using both treated and untreated fiber. Untreated fiber is used as a baseline for the comparison of mechanical properties.

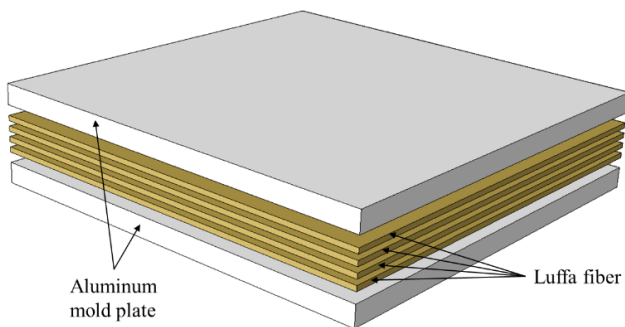


Fig. 4 Schematic diagram of lay-up.

2.5 Tensile Test

Tensile test on both type of composite (treated and untreated) are performed. Total 10 samples are tested among 5 are from untreated fiber and the remaining are from treated fiber composite. The specimens are cut from the composite plate manufactured following the standard ASTM D3039 [21] and the specimen size is 147 mm \times 20 mm \times 4.5 mm as shown in **Fig. 5**. During the test, the specimens are placed inside the hydraulic grip of universal testing machine at a loading rate of 2 mm/min. The load-displacement response are recorded and later these data are used to calculate stress and strain along with specimen width, thickness and a gauge length of 25 mm.

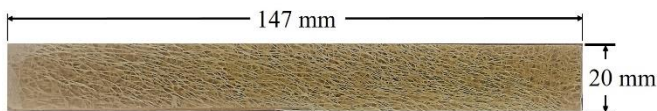


Fig. 5 Tensile test specimen.

2.6 Flexural Test

Three-point bending test is performed on the manufactured specimen to evaluate the flexural properties. Five specimen from the untreated and five specimen from the treated fiber are tested following the standard ASTM D7264 [22] and the specimen dimension is 133 mm \times 28 mm \times 4.5 mm as shown in **Fig. 6**. Three-point bending tests are carried out on the same universal testing machine with a loading rate of 1 mm/min. A constant span length to thickness of 32:1 is maintained during the test and for calculating the flexural chord modulus of

elasticity, 0.001 to 0.003 strain range is selected as suggested by ASTM D7264.

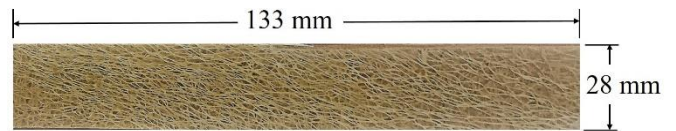
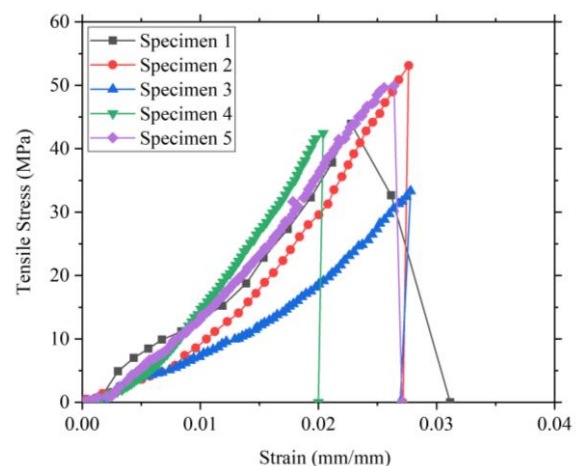


Fig. 6 Flexural test specimen.

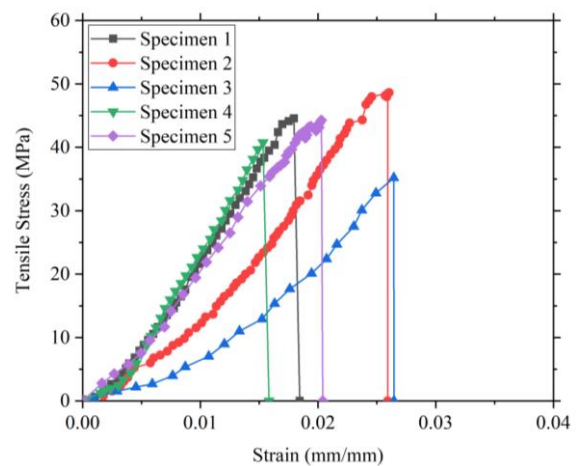
3. Results and Discussion

3.1 Tensile Test Results

As mentioned in section 2.5, tensile test is performed on luffa fiber reinforced epoxy composite for both untreated and treated fiber. **Fig. 7(a)** shows the stress-strain response for untreated fiber while **Fig. 7(b)** shows the same for the treated fiber. By comparing **Fig. 7(a)** and **Fig. 7(b)** it is observed that the maximum stress for treated fiber is higher compared to the untreated fiber which indicates that the strength of the composite manufactured from the treated fiber increases with fiber treatment. **Fig. 8(a)** confirms this statement, which is a bar chart showing the strength of untreated and treated fiber composite. The average tensile strength of untreated and treated fiber are 11.43 MPa and 14.54 MPa respectively, which suggests a 27.21% increase in the tensile strength as shown in **Table 1**.



(a)

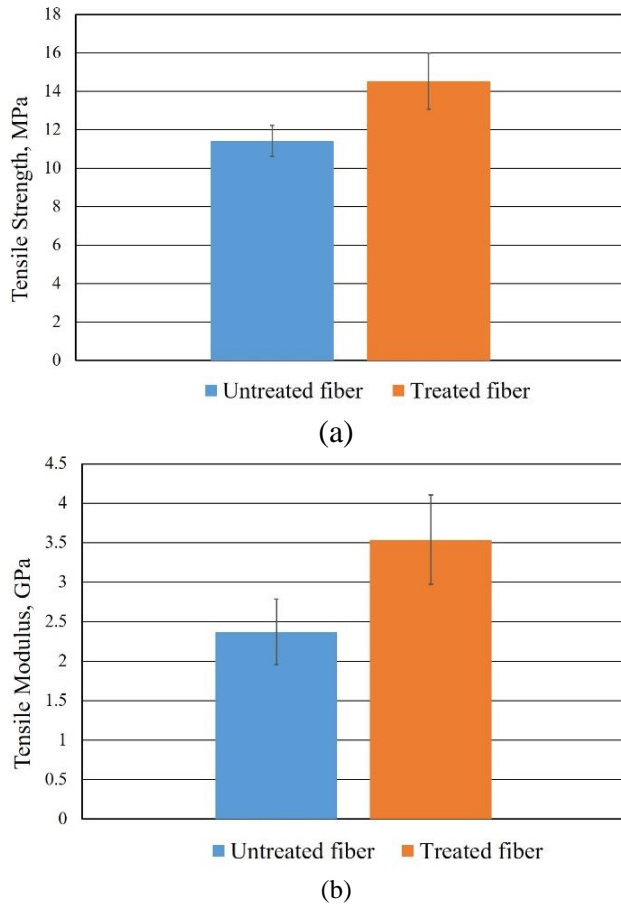


(b)

Fig. 7 Stress-strain diagram for the tensile test of (a) bamboo strip and (b) hybrid composite

Table 1 Tensile test results with standard deviation.

Condition	Tensile Strength (MPa)	% Increase	Tensile Modulus (GPa)	% Increase
Untreated	11.43 ± 0.81	-	2.37 ± 0.41	-
Treated	14.54 ± 1.43	27.21	3.54 ± 0.57	49.37

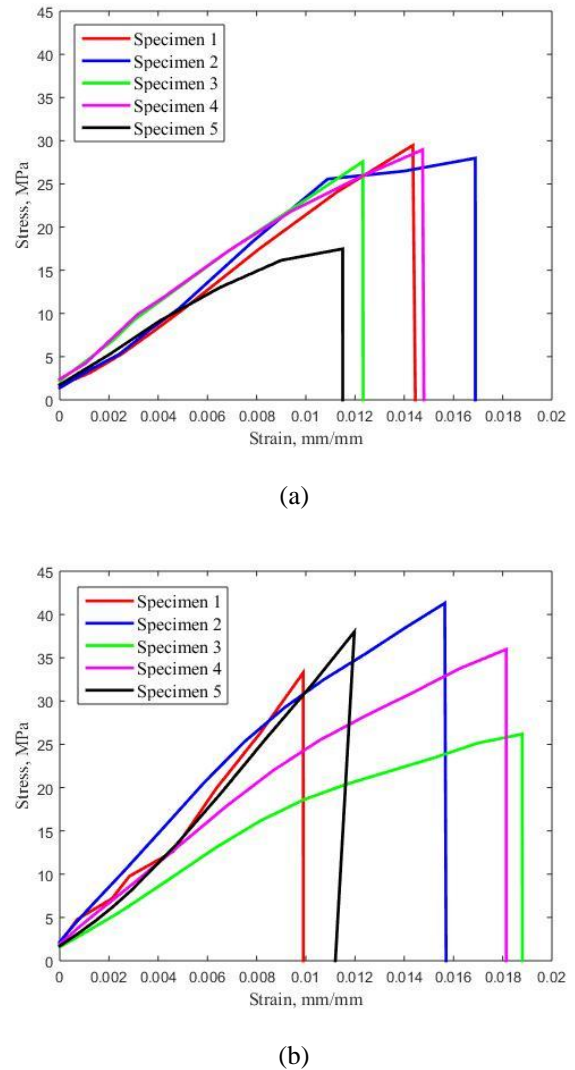
**Fig. 8** Effect of chemical treatment on (a) Tensile strength and (b) Tensile modulus.

It is also observed from **Fig. 7** that the slope of the stress-strain curve for treated fiber composite is higher compared to untreated fiber. This suggests that the tensile modulus increases with the treatment of fiber and is represented by **Fig. 8(b)**. Table 1 shows a comparative analysis of the tensile modulus for untreated and treated fiber. The average tensile modulus for untreated fiber is 2.37 GPa and for treated fiber is 3.54 GPa. So, the treatment of fiber increases the tensile modulus by 49.37%.

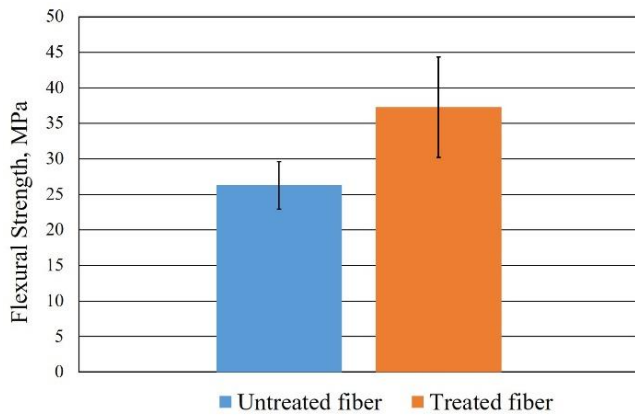
3.2 Flexural Test Results

Fig. 9 shows stress-strain response from the three point bending test for both untreated and treated fiber composites. It

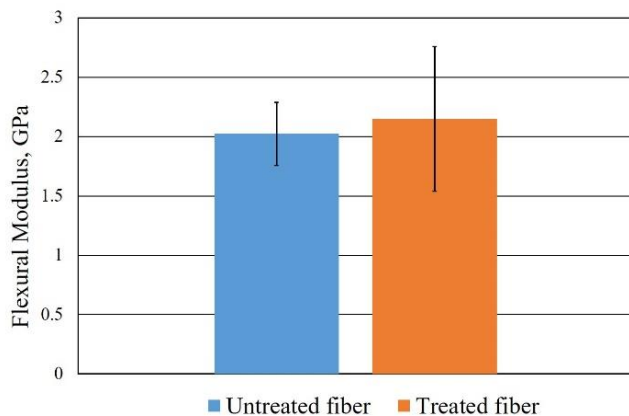
is observed from this figure that the maximum strength and slope of the curve of treated fiber (**Fig. 9(b)**) is higher compared to the untreated (**Fig. 9(a)**) one. This is represented in **Fig. 10** and **Table 2**. **Table 2** shows that the flexural strength and modulus of treated fiber is increased by 41.84% and 6.44% respectively compared to untreated fiber.

**Fig. 9** Stress-strain diagram of flexural test for (a) Untreated fibers and (b) Treated fibers.**Table 2** Flexural test results with standard deviation.

Condition	Flexural Strength (MPa)	% Increase	Flexural Modulus (GPa)	% Increase
Untreated	26.29 ± 3.36	-	2.02 ± 0.27	-
Treated	37.29 ± 7.09	41.84	2.15 ± 0.61	6.44



(a)



(b)

Fig. 10 Effect of chemical treatment on (a) Flexural strength and (b) Flexural modulus.

4. Conclusion

The mechanical properties of luffa fiber reinforced epoxy composite are investigated in this paper. Luffa fiber is treated with NaOH and benzoyl chloride and the mechanical properties are compared for untreated and treated fiber composites. It is found that the tensile strength and modulus for treated fiber are increased by 27.21 % and 49.37 % respectively. Flexural strength and modulus is increased by 41.84 % and 6.44 % respectively. It is found that the overall mechanical properties of the composites improved because of chemical treatment.

References

- [1] Islam, M.S., Melendez-Soto, E., Castellanos, A.G. and Prabhakar, P., 2015. Investigation of woven composites as potential cryogenic tank materials. *Cryogenics*, 72, pp.82-89.
- [2] Castellanos, A.G., Islam, M.S., Shuvo, M.A.I., Lin, Y. and Prabhakar, P., 2018. Nanowire reinforcement of woven composites for enhancing interlaminar fracture toughness. *Journal of Sandwich Structures & Materials*, 20(1), pp.70-85.
- [3] Islam, M.S. and Prabhakar, P., 2017. Interlaminar strengthening of multidirectional laminates using polymer additive manufacturing. *Materials & Design*, 133, pp.332-339.

- [4] Deshpande, A.P., Bhaskar Rao, M. and Lakshmana Rao, C., 2000. Extraction of bamboo fibers and their use as reinforcement in polymeric composites. *Journal of applied polymer science*, 76(1), pp.83-92.
- [5] Ochi, S., 2012. Tensile properties of bamboo fiber reinforced biodegradable plastics. *International Journal of Composite Materials*, 2(1), pp.1-4.
- [6] Ramesh, M., Palanikumar, K. and Reddy, K.H., 2013. Mechanical property evaluation of sisal-jute-glass fiber reinforced polyester composites. *Composites Part B: Engineering*, 48, pp.1-9.
- [7] Akil, H.M., Cheng, L.W., Ishak, Z.M., Bakar, A.A. and Rahman, M.A., 2009. Water absorption study on pultruded jute fibre reinforced unsaturated polyester composites. *Composites Science and Technology*, 69(11-12), pp.1942-1948.
- [8] Prasad, A.R. and Rao, K.M., 2011. Mechanical properties of natural fibre reinforced polyester composites: Jowar, sisal and bamboo. *Materials & Design*, 32(8-9), pp.4658-4663.
- [9] Mi, Y., Chen, X. and Guo, Q., 1997. Bamboo fiber-reinforced polypropylene composites: Crystallization and interfacial morphology. *Journal of applied polymer science*, 64(7), pp.1267-1273.
- [10] Tokoro, R., Vu, D.M., Okubo, K., Tanaka, T., Fujii, T. and Fujiura, T., 2008. How to improve mechanical properties of polylactic acid with bamboo fibers. *Journal of materials science*, 43(2), pp.775-787.
- [11] Chattopadhyay, S.K., Khandal, R.K., Uppaluri, R. and Ghoshal, A.K., 2011. Bamboo fiber reinforced polypropylene composites and their mechanical, thermal, and morphological properties. *Journal of applied polymer science*, 119(3), pp.1619-1626.
- [12] Chen, X., Guo, Q. and Mi, Y., 1998. Bamboo fiber-reinforced polypropylene composites: A study of the mechanical properties. *Journal of applied polymer science*, 69(10), pp.1891-1899.
- [13] Ismail, H., Shuhelmy, S. and Edyham, M.R., 2002. The effects of a silane coupling agent on curing characteristics and mechanical properties of bamboo fibre filled natural rubber composites. *European Polymer Journal*, 38(1), pp.39-47.
- [14] Athijayamani, A., Thiruchitrambalam, M., Natarajan, U. and Pazhanivel, B., 2009. Effect of moisture absorption on the mechanical properties of randomly oriented natural fibers/polyester hybrid composite. *Materials Science and Engineering: A*, 517(1-2), pp.344-353.
- [15] Dhakal, H.N., Zhang, Z.Y. and Richardson, M.O.W., 2007. Effect of water absorption on the mechanical properties of hemp fibre reinforced unsaturated polyester composites. *Composites science and technology*, 67(7-8), pp.1674-1683.
- [16] Haque, M.M., Hasan, M., Islam, M.S. and Ali, M.E., 2009. Physico-mechanical properties of chemically treated palm and coir fiber reinforced polypropylene composites. *Bioresource technology*, 100(20), pp.4903-4906.
- [17] Mohanta, N. and Acharya, S.K., 2016. Fiber surface treatment: Its effect on structural, thermal, and mechanical

- properties of Luffa cylindrica fiber and its composite. *Journal of composite materials*, 50(22), pp.3117-3131.
- [18] Mohanta, N. and Acharya, S.K., 2013. Tensile, flexural and interlaminar shear properties of Luffa cylindrica fibre reinforced epoxy composites. *Int. J. Macromol. Sci*, 3, pp.6-10.
- [19] Asif, M., Rahman, K.A., Faisal, M.O. and Islam, M.S., 2020. Comparative Study on Mechanical Properties of Bamboo Strip and Bamboo Strip-Glass Fiber Reinforced Hybrid Composites. *Journal of Engineering Advancements*, 01(01), pp.06-10.
- [20] Islam, M.S., Azmy, S. and Almamun, A., 2019. Comparative Study on Mechanical Properties of Banana and Rattan Fiber Reinforced Epoxy Composites. *American Journal of Engineering Research (AJER)*, 8(2), pp. 1-6.
- [21] Standard, A.S.T.M., 2008. Standard test method for tensile properties of polymer matrix composite materials. *ASTM D3039/D M*, 3039, p.2008.
- [22] ASTM D7264, 2007. Standard test method for flexural properties of polymer matrix composite materials. *American Society for Testing and Materials Annual Book of ASTM Standards*.

Near-wall and Turbulence Behavior of Swirl Flows through an Aerodynamic Nozzle

Md. Tanvir Khan, Sharif M. Islam, and Zahir U. Ahmed*

Department of Mechanical Engineering, Khulna University of Engineering & Technology, Khulna-9203, BANGLADESH

Received: June 04, 2020, Revised: June 21, 2020, Accepted: June 21, 2020, Available Online: June 28, 2020

ABSTRACT

It is often a challenge to achieve uniform flow in turbulent swirl flow and to predict the flow within the nozzle as measurement diagnostics face difficulty to capture both mean flow and turbulence. The purpose of this study is to numerically investigate the near wall flow characteristics and turbulent behavior for the effect of different tangential inlet numbers of an incompressible turbulent swirl air jet. In this regard, axial-plus-tangential flow based swirling nozzle is considered for the simulation using finite volume method, where turbulence is approximated by the Shear Stress Transport (SST) $k-\omega$ model. The results show that axial and tangential velocity at the wall vicinity response the most. Moreover, the turbulent flow characteristic for no swirl flow is nearly uniform, but for swirl flow it fluctuates abruptly near the inlet section where the swirl has introduced. The skin friction coefficient for 2TP is the maximum for swirl flow and for no swirl condition the skin friction coefficient is nearly uniform. Due to the swirl introduction the pressure drop characteristics near the nozzle center response quickly and near the wall vicinity this property changes slowly. The magnitude of swirl decay fluctuates before the nozzle converging section however after the nozzle converging section the swirl decay is nearly constant. The local swirl near the inlet is highly unpredictable although after the nozzle converging section the local swirl profile is nearly similar for 2TP, 3TP and 4TP.

Keywords: Turbulent; Nozzle; Swirl; Aerodynamic; CFD; Pressure.



This work is licensed under a [Creative Commons Attribution-NonCommercial 4.0 International](https://creativecommons.org/licenses/by-nc/4.0/)

1. Introduction

Swirl flows are a classical form of fluid flow and typically encountered in many engineering applications, such as gas turbine combustor and cyclonic separator, as well as in nature, such as tornado. In swirling flows generally two types of vortex emerge, namely solid body rotation and free vortex flow. However, in actual practice, a mixed of these two typically appears whereby azimuthal velocity increases with radius in the core and decreases afterwards. The academic and industrial research on swirling jets was found to be challenging due to their unique characteristics, such as flow reversal, vortex bubble and anisotropic turbulences in both free and impinging jets. The detailed flow physics, instability and above features of swirling flows are explicitly available in the literature [1]. The axial and radial pressure gradient in swirling flows affects downstream flow development and wall-bounded flows. Swirl flows are generated in different applications in many ways, such as rotating pipe, rotating vanes and twisted tapes inside stationary pipe, axial-plus-tangential entry [2]-[7]. The wide variations of generations can be divided into two broad groups: geometrical and aerodynamical. In geometrically generated swirl flows, for example rotating vanes or twisted tapes inside pipes, the flow is disturbed by such geometries or obstacles, which exacerbates the generality of the flow and difficult to draw a summative observation. On the other hand, aerodynamically generated swirl flows, such as rotating pipe or axial-plus-tangential entry flow, have better control of the flow and common flow physics may establish in different researches. Despite geometrically generated swirl flows are widely available in the literature and still progressing, fundamentals of aerodynamic swirl flows are currently being investigated in detail because of its prevalence to use recently in number heat treatment applications.

Yajnik and Subbaiah [8] experimentally studied the effects of swirl on internal turbulent flows by conducting experiments on turbulent pipe flow. They found that the mean velocity profiles close to and away from the wall admit similarity representations at sufficiently large Reynolds numbers and extended velocity defect law is sensitive to swirl as the wall law is not sensibly dependent on swirl. Chang and Dhir [9] found a flow reversal region in axial velocity profile in the central portion of an acrylic tube and an axial velocity increase near the wall. Kito and Kato [10] studied the near wall velocity distribution of turbulent swirling flow in circular pipes and concluded that the flow becomes three-dimensional after transitional swirl intensity. Later, Kito [11] investigated the turbulent behavior of free-vortex-type swirling flow through a long straight circular pipe and reported that the swirling component decays downstream as a result of wall friction. Buschmann et al. [12] explored the wall behavior, the location of the peak Reynolds shear stresses and the three normal stresses of turbulent channel/pipe flows, and stated that no scaling works equally for all parameters. Ahmed et al. [13] conducted measurements of mean velocity and turbulence of swirling flows using dual wire CTA probe both in the core and near-wall regions. However, the measurements were confined to the immediately above the nozzle exit plane. Effect of viscosity and surface tension of fluids and associated instabilities in annular flow were also analyzed in some studies [14]-[15].

Since both DNS and LES typically require sufficiently smaller sized mesh or large mesh quantity to resolve small-scale turbulence, Reynolds Averaged Navier-Stokes (RANS) were widely used in swirling flows by many investigators. Although it is believed that among various RANS models the Reynolds Stress Model (RSM) would perform better because of its ability to capture anisotropy of turbulent shear stress, this hypothesis

was not found to be universal in the past [16]-[17]. In fact, some studies revealed that two-equation models (based on Boussinesq approximation) can be applied with acceptable accuracy in comparison with experimental data for moderate swirl flows - [18]-[19]. Nouri-Borujerdi and Kebriaee [20] simulated the turbulent boundary layer of an incompressible viscous swirling flow through a conical chamber using finite volume method and reported that the boundary layer thickness is dependent on the velocity ratios, Reynolds number and nozzle angle. Najafi et al. [21] investigated turbulent swirling decay in a vertical straight fixed pipe where swirl is induced by rotating honeycombs. They showed RSM with two-layer zone model for different near wall approaches are fairly well to predict the swirling flow but fail to predict the pressure distribution along the pipe wall. Islam et al. simulated an aerodynamically generated swirl flow using SST k- ω model in the nozzle exit plane. The result showed centerline velocity [22] decay for introducing low levels of swirl into the impinging jet and a significant reduction in turbulent kinetic energy at the wall region. More recently, researchers [23]-[27] performed simulations of aerodynamic swirl flow using SST k- ω model and validated their results with the literature.

The above discussion revealed that although a significant amount of research available on swirling flows, they are mostly confined to gas turbine combustors, cyclonic separator, or geometry induced swirl flows. Relevant aerodynamically swirling flows are either classical in nature (experimental) with outdated experimental facility to resolve near-wall and turbulence behaviors inside the nozzle or tested robustness of various numerical schemes against experimental data with limited focus on flow behaviors. Thus, a detailed study for the effect of geometric parameters on near-wall and turbulence behaviors for an aerodynamic swirl nozzle appears to be limited in the literature. As such, the current numerical study will bridge this gap by investigating non-swirling and swirling flows from an aerodynamic nozzle for the same initial and flow conditions. The paper will examine the effect of number of tangential ports on mean and turbulence flow development along the length of the nozzle.

2. Methodology

2.1 Problem formulation

An aerodynamically generated swirl nozzle, which is capable of seamless transition from non-swirling to highly swirling jets, is considered in this study. The nozzle is axial-plus-tangential entry type and consists of three tangential around the nozzle periphery and an axial port at the bottom of the nozzle. Detailed dimension of this nozzle is available in [4],[28], hence is not repeated here for brevity. The uniform flow was ensured by the flow settling chamber with honeycomb. The aerodynamic swirl flow was generated when both the uniform axial and tangential flows from different number of circumferentially oriented and inclined ports mix together farther downstream. In this case, three variants of tangential ports: 2-Tangential ports (2TP), 3-Tangential ports (3TP) and 4-Tangential ports (4TP) are considered. The exit of the nozzle has diameter (D) 40 mm, with a total length of 577 mm. A three-dimensional view with the relative orientation of tangential ports is shown in Fig. 1.

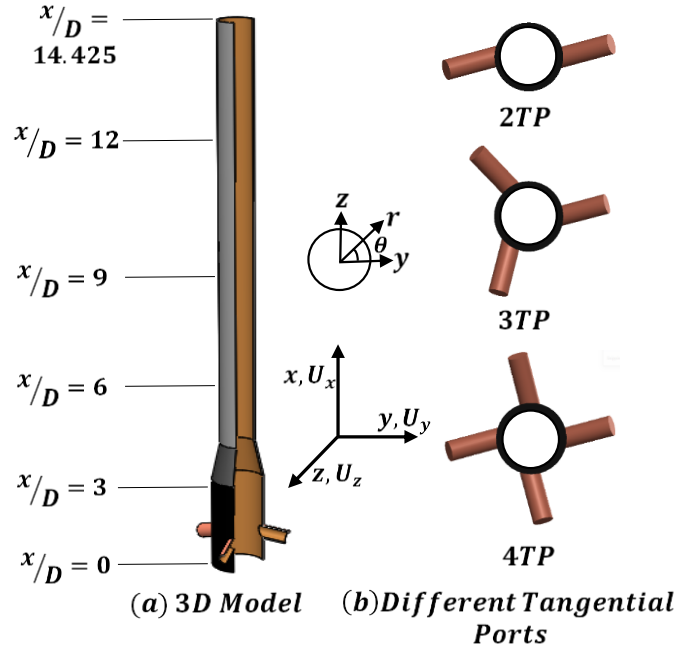


Fig. 1 (a) CAD view of the aerodynamic swirl nozzle (sliced to show the internal cavity), and (b): different number of tangential ports to impart azimuthal component.

2.2 Governing Equation and Boundary Conditions

The governing equations to solve the incompressible, steady-state flow characteristics within the aerodynamic swirl nozzle are the conservation of mass and momentum as follows:

$$\nabla \cdot \vec{V} = 0 \quad (1)$$

$$\rho (\vec{V} \cdot \nabla) \vec{V} = -\nabla \hat{P} + \mu \nabla^2 \vec{V} \quad (2)$$

Here, \vec{V} is the velocity vector, and ρ and μ are the density and dynamic viscosity of the fluid, respectively. Since the current problem is turbulent in nature, RANS approach is applied to solve the mean and turbulence quantities. In RANS approximation, each variable is composed of time-averaged part (steady) and turbulence part, as shown below:

$$\hat{\phi} = \phi + \phi' \quad (3)$$

where ϕ is a variable used in equations (1) and (2). Upon implementing the equation (3) into the governing equations and using equation (1) and setting time-average of turbulence equals to zero, the resulting RANS equations emerge. The RANS equations are similar to the governing equations, except an additional term $(\overline{\rho u' u'})$ in equation (2). This additional term is known as turbulent shear stress, which governs the turbulence characteristics. The shear stress components are determined via mean velocity gradients by the Boussinesq hypothesis:

$$\overline{u'_i u'_j} = \frac{2}{3} k \delta_{ij} - \mu_t \left(\frac{\partial u_i}{\partial x_j} + \frac{\partial u_j}{\partial x_i} \right) \quad (4)$$

Where, μ_t is the turbulent viscosity and is a function of k and ω , which are determined via an appropriate turbulence model. In this research, the SST k - ω model, proposed by Menter and Egorov [29], is chosen to model turbulence transport quantities: turbulence kinetic energy, k , and the specific dissipation rate, ω . SST k - ω model was found to be one of the best performing RANS models in swirling and wall-bounded flows [16],[30]-[31].

The boundary conditions considered in this problem are mass flow inlet at the axial and tangential ports, pressure outlet at the nozzle exit plane and wall at the nozzle wall. The inlet conditions are adopted from the study [4] for realistic predictions. For no-swirl flow, axial flows (only) are provided from the bottom of the nozzle, with no flows from tangential ports. Conversely, for the swirling flows, three tangential ports supply the same amount of mass flow, with no axial flow from the bottom of the nozzle. This ensures the same Reynolds number, where the average velocity in Reynolds number is determined by volume flow rate divided by nozzle exit area. The pressure outlet condition is applied at the nozzle exit with atmospheric pressure whereby turbulence is specified by 2% intensity and hydraulic diameter. Finally, no-slip condition at the nozzle wall with ambient temperature is used.

2.3 Numerical Settings and Model Validation

The above governing equations (1-4) and two transport equations (SST k - ω) are solved by finite volume based commercial software ANSYS Fluent v17. The pressure-based coupled algorithm is used to simultaneously solve the governing equations. For the pressure discretization PRESTO (PREssure STaggering Option) is applied, and the second-order central-differenced for diffusion terms and second-order upwind scheme for convective terms of the transport equations are used. Hexahedral mapped mesh type was used in multi-zone meshing with an element size 0.0025m. A typical mesh independence test is shown in Fig. 2 for 3TP. In this case, four different grid elements are tested, namely, 974001, 1310326, 1647089 and 1892870 elements. The results are found to be invariant, except the 974001 elements. As such, a mesh containing 1647k element is chosen in this study. Another testing is also done for first layer height on y^+ values and wall shear stress profiles, and is shown in Fig. 3. It appears the first layer cell height has little influence on those wall characteristics. As such, a first layer height of 0.05 mm is chosen in this study. The figure also shows that above settings ensured y^+ values less than 0.2 for the whole domain. The solution is assumed to be converged when the residuals of the flow parameters are less than 10^{-5} . Mass conservation is also checked between inlet ports and the nozzle exit for converged solutions and the difference between inlets and outlet is found close to zero. Cartesian coordinates are given by (x, y, z) with corresponding velocity components (U_x, U_y, U_z) . For convenience, results of this 3D simulation are presented by polar coordinates (x, r, θ) with x -axis coinciding for each system. In this regard, the corresponding axial (U) and tangential (W) velocity components are derived from the Cartesian coordinate data using the axes transformation rule.

2.4 Parameter Definition

The flow ratio Q_r is the ratio of total mass flow rate through tangential inlets to the total flow rates in the nozzle, i.e.

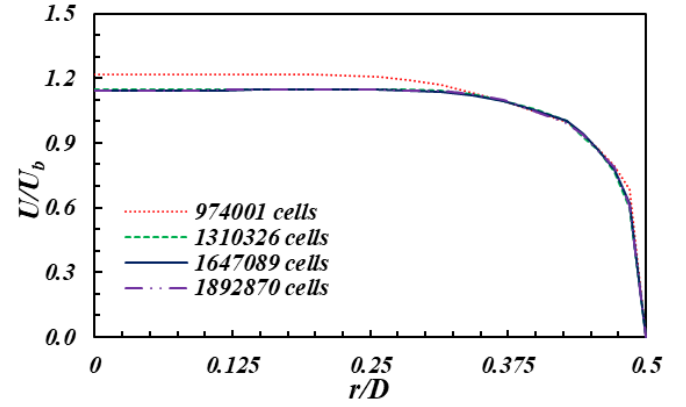


Fig. 2 Sensitivity of mesh elements for the case 3TP.

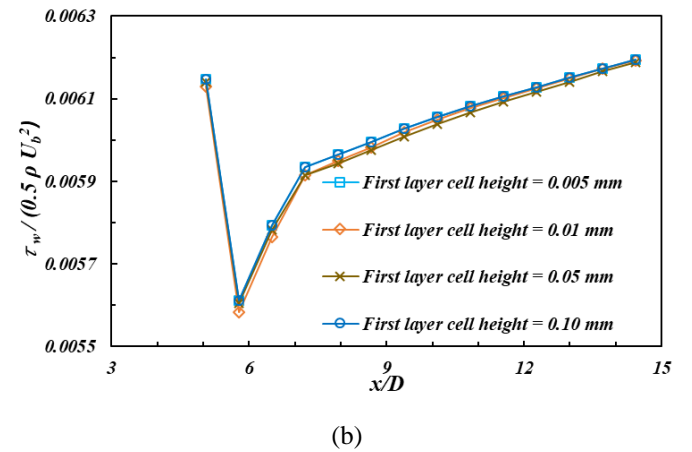
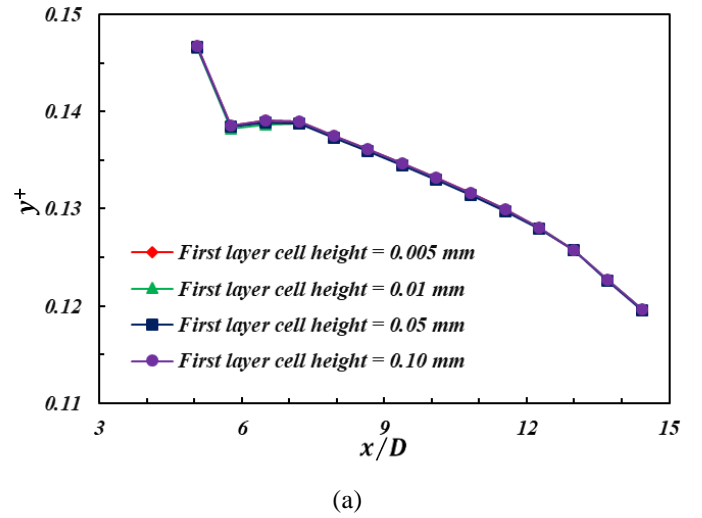


Fig. 3 Effect of first layer cell height on y^+ and normalized wall shear stress.

sum of flowrates through all axial and tangential inlets. Mathematically,

$$Q_r = \frac{Q_t}{Q_a + Q_t} = \frac{Q_t}{Q_T} \quad (5)$$

The Reynolds number is defined as,

$$Re = \frac{Q_T D}{Av} \quad (6)$$

Where, A is the nozzle area at the exit plane of the nozzle and ν is the dynamic viscosity of fluid. Two different swirl number definitions are common as the ratio of axial flux of tangential momentum to the axial flux of axial momentum:

$$S = \frac{2\pi\rho\int_0^R r^2 UW dr}{2\pi R\rho\int_0^R r(U^2 - 0.5W^2) dr} \quad (7)$$

$$S' = \frac{\int_0^R r^2 UW dr}{R\int_0^R r U^2 dr} \quad (8)$$

Finally, the local swirl number is defined as,

$$S^*(r) = \frac{W}{U} \quad (9)$$

2.5 Validation

The simulation data of the swirl nozzle is first tested with different turbulence models and validated by comparing with experimental data [4] at the nozzle outlet plane with three tangential ports for the case $Q_r = 0$ and 1 (Fig. 4). It appears that SST $k-\omega$ model predicts the flow behavior well for both non-swirling and swirling cases. As such, SST $k-\omega$ model will be used for the data presented in the ensuing results and discussion section. Fig. 4 also shows a good agreement between the numerical prediction and the experimental data for $Q_r = 0$. A slight deviation is observed for $Q_r = 1$, but importantly, the numerical data predicts well the profile behaviors and peak locations. The deviation is attributed to the possible measurement inaccuracy associated with CTA X-wire and experimental flow settings [13]. This results an overestimation of the mean velocity components than their corresponding true values. The deviations may also be partly attributed to the inability of RANS approach to accurately capture highly swirling flows.

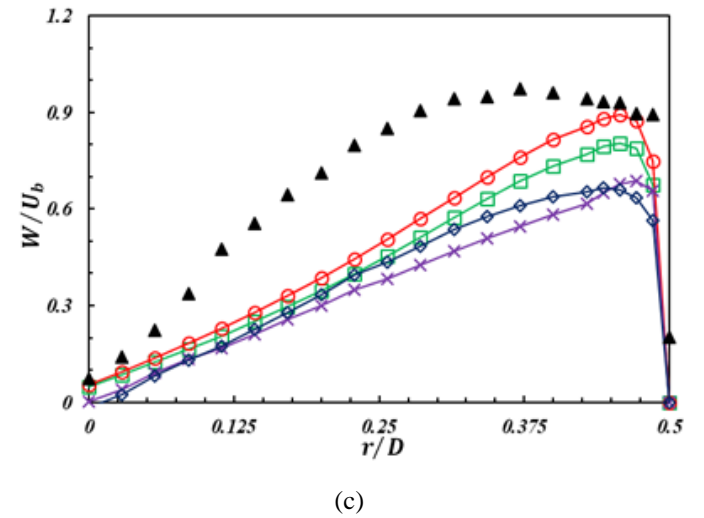
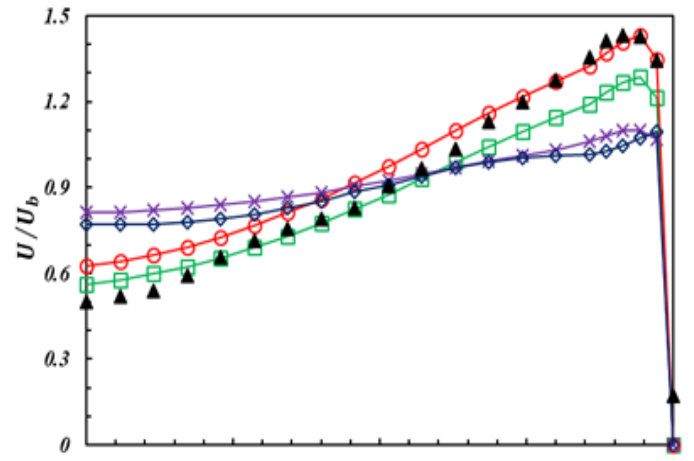
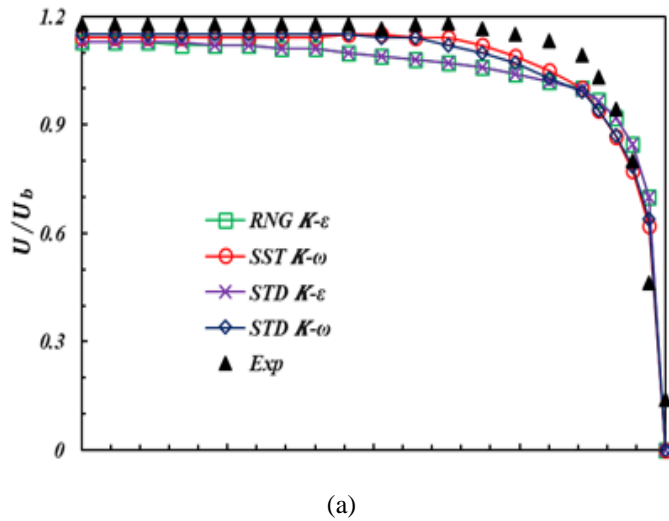


Fig. 4 Different turbulence models against experimental data [4] for (a) U/U_b for $Q_r = 0$, (b) U/U_b for $Q_r = 1$ and (c) W/U_b for $Q_r = 1$.

3. Results and Discussion

This section includes presentation of mean and turbulence controlling parameters, such as velocity, boundary layer thickness, pressure drop, wall shear stress and turbulent shear stress for the effect of different number of tangential ports at two flow conditions ($Q_r = 0$ and $Q_r = 1$).

Swirl decay along the length is shown in Fig. 5 for the 3TP case. The swirl number is calculated using the Equation (7) and Equation (8). It is observed that near the nozzle inlet the swirl number S is highly fluctuating and after the converging section, the swirl number is nearly constant. Initially, the swirl number decreases from the inlet. When the tangential port has introduced the value of swirl number increases and immediately after the increment the swirl number drops again. In the nozzle converging section the magnitude of the swirl number rises again at first and then the value decreases and finally increases before coming at a constant magnitude. In case of S' the values initially increasing from the nozzle inlet come to a constant magnitude after the nozzle converging section. It is evident that the swirl number S shows a very unpredictable nature before the nozzle converging section.

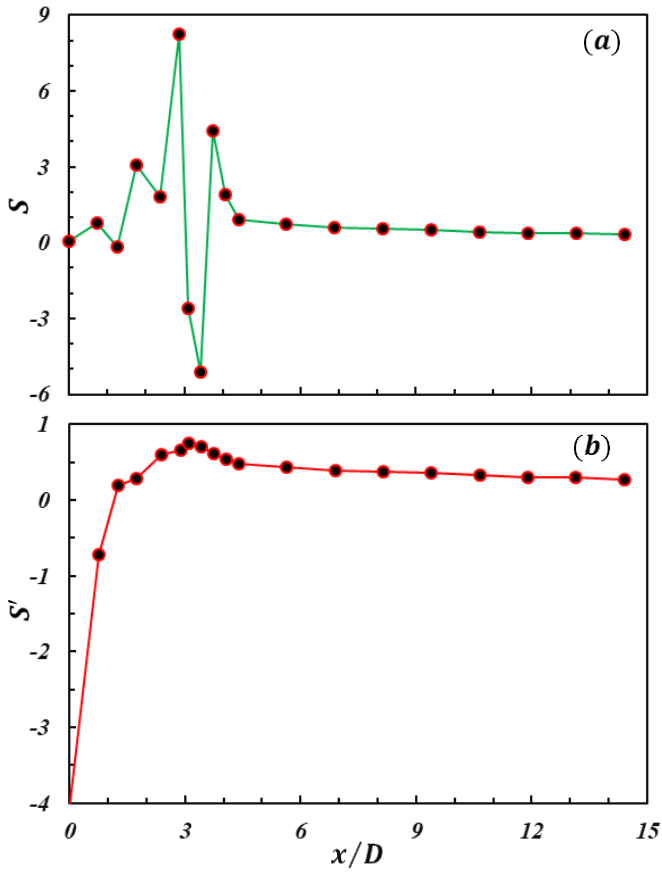


Fig. 5 Swirl decay along the length of the nozzle for 3TP case.

Fig. 6 shows the local swirl numbers along the radial location of the nozzle at the different axial positions ($x/D = 1.275, 3.1, 5.65, 9.4$, and 14.425) of the nozzle for three different numbers of tangential ports, namely, 2TP, 3TP, and 4TP. It is observed that the profile of local swirl at $x/D = 5.65, 9.4$, and 14.425 are almost the same in nature for all the cases. The local swirl increases gradually from the center of the nozzle toward the wall and near the wall, a sudden drop occurs. However, the local swirl profiles at $x/D = 3.1$ are similar for 2TP and 3TP although for 4TP the local swirl profile is parabolic from the nozzle center toward the nozzle wall. The value of local swirl near the inlet at $x/D = 1.275$ is highly unpredictable due to the swirl induction. The local swirl profile for 2TP and 3TP are nearly similar but for 4TP the profile is different. The local swirl near the nozzle wall suddenly increases and drops immediately after the increase and finally raise to the wall for both 2TP and 3TP. However, the local swirl profile at 4TP is like a bell shape; increasing from the nozzle center it becomes constant at $r/D = 0.2$ to $r/D = 0.35$ and then decreases again towards the nozzle wall. As the swirl is introduced at this location the local swirl profile becomes highly unpredictable.

The axial velocity vectors at five different axial locations ($x/D = 4.75, 7.50, 9.75, 12.5$ and 14.425) are presented in **Fig. 7** for non-swirling (**Fig. 7a**) and swirling (**Fig. 7b-d**) conditions. Velocity is found to be the almost uniform after the converging section for no swirl flow ($Q_r = 0$), but the magnitude is the highest near the exit plane, with a reduction towards the wall due to boundary layer formation. In contrast, for swirl flow ($Q_r = 1$), velocity magnitude is found to be the

higher near the inlet and towards the nozzle exit, the velocity magnitude decreases. The axial velocity magnitude is proportional to the number of tangential ports and the velocity magnitude is zero at the wall due to no-slip condition. The axial velocity vectors at $x/D = 4.75$ is symmetric from the centerline when swirl is induced (**Fig. 7b-d**), however, the velocity distribution becomes asymmetrical as the flow approaches the outlet. The velocity distribution is more symmetrical along the radial direction for 2TP than 3TP & 4TP with a slight decrease near the center except for exit plane. At $x/D = 14.425$, velocity reduction near the center is highest for 2TP.

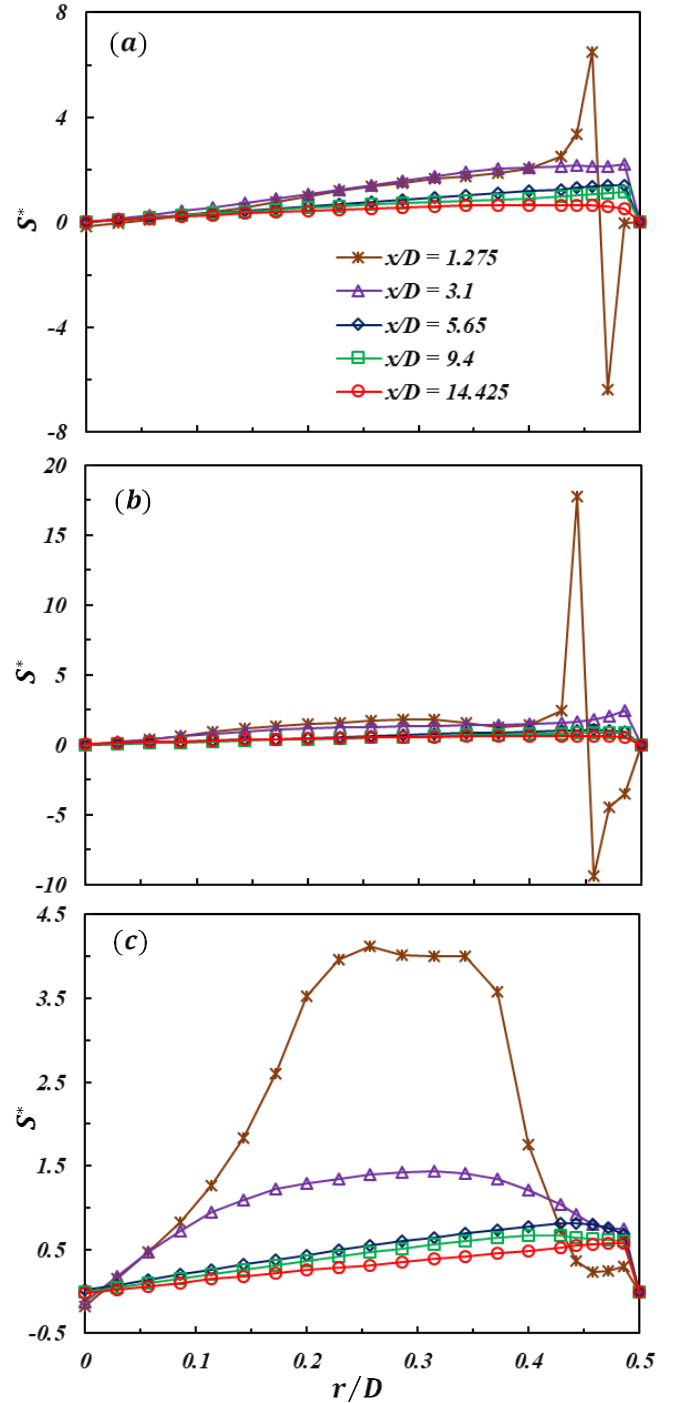


Fig. 6 Local swirl characteristics along the length of the nozzle (a) 2TP, (b) 3TP, (c) 4TP.

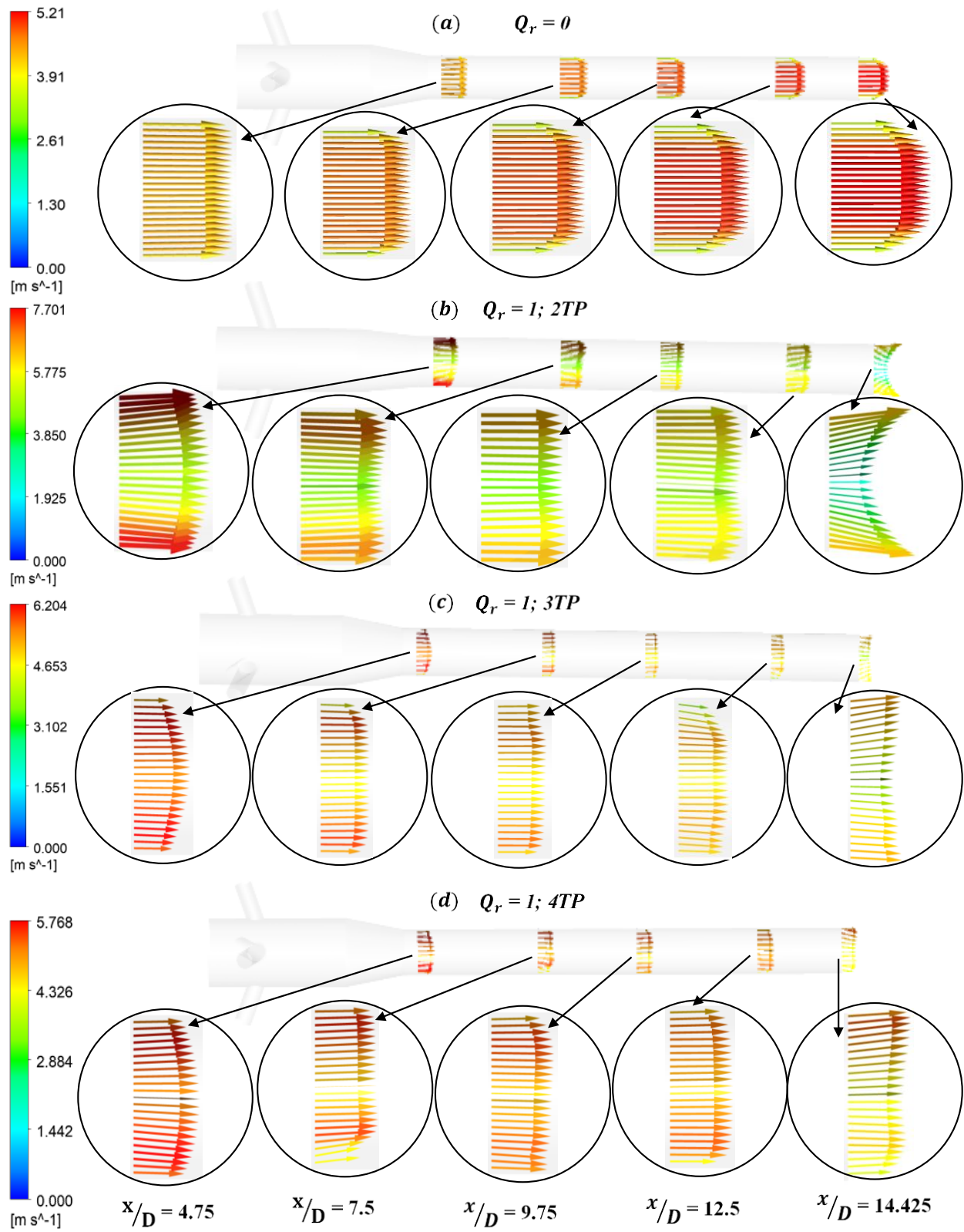


Fig. 7 Axial velocity vectors at different axial locations for non-swirling (a), and swirling flows: (b) 2TP, (c) 3TP and (d) 4TP.

Fig. 8 depicts the boundary layer thicknesses along the length of the nozzle for both non-swirl and swirling (2TP, 3TP and 4TP) conditions. It is observed that the magnitude of boundary layer thickness at 2TP is pretty low compare to the other. For swirl flow conditions the boundary layer thickness at the beginning is small and near the exit the boundary layer thickness increases. At the middle of the nozzle the boundary layer thickness is nearly constant. However, for no swirl flow condition the boundary layer thickness higher and then the boundary layer thickness gradually decreases towards nozzle exit.

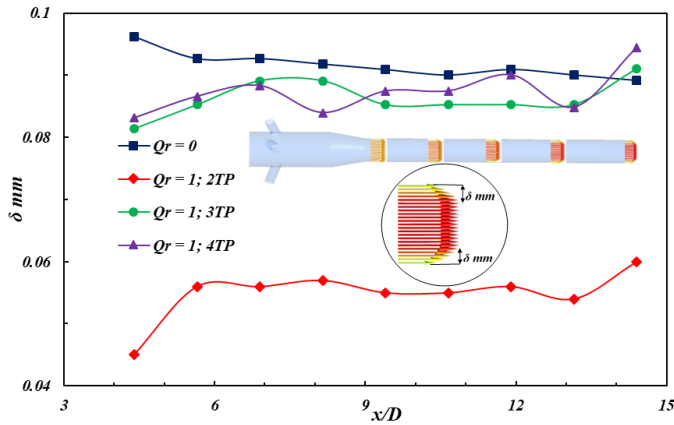


Fig. 8 Boundary layer thickness along the length of the nozzle.

Fig. 9 demonstrates the axial (U/U_b) and tangential (W/U_b) velocity components near the wall i.e. at $y/D = 0.01, 0.05$ and 0.1 for $Q_r = 0$ and $Q_r = 1$. In the figure, Y represents the distance from the wall of the swirl nozzle. It is observed that at for swirl condition the near-wall axial velocity profile is identical for all the location and it increases from the inlet to the nozzle converging section. Then, the velocity suddenly decreases at $Y = 0.01D$ immediately after the converging section. The axial velocity is then nearly constant for all the axial location of the nozzle. However, the axial velocity decreases very little after the nozzle convergence at $Y = 0.05D$ and $0.1D$, and no significant change occurs. For swirl flow condition the near-wall axial and tangential velocity increases after the swirl flow introduction. Then after the nozzle converging section the near-wall axial and tangential velocity show a very little deviation and along the nozzle axial location the velocity profile is nearly uniform at $Y = 0.05D$ and $Y = 0.1D$. However, the near-wall axial and tangential velocity profile at $Y = 0.01D$ is fluctuates highly along the length of the nozzle, especially the tangential velocity profile shows a totally unpredictable nature. The overall near-wall axial and tangential velocity distribution at $Y = 0.01D$ is low in magnitude than at $Y = 0.05D$ and $Y = 0.1D$. It can be observed that the velocity profile at the wall vicinity ($Y = 0.01D$) response highly than the other position.

The interplay between the number of tangential ports and the swirl intensity for the effect of skin friction coefficient along the length of the nozzle is shown in **Fig. 10**. It is observed that for no swirl condition the magnitude of Skin friction coefficient is very low and along the nozzle axial location no change occurs. However, the Skin friction coefficient at high swirl flow at 2TP is the maximum along the nozzle axial location although for 3TP and 4TP no significant deviation is

observed. In every case of swirl flow the Skin friction coefficient at the nozzle exit is the maximum. Although the Skin friction coefficient along the axial location is not significantly changing however, near the exit it suddenly increase. The overall distribution of the Skin friction coefficient is not similar for all the case.

Fig. 11 displays the pressure drop at different radial locations for swirling flow (3TP). The inlet pressure is taken at the reference pressure and pressure drop is calculated based on the pressure of the nozzle inlet. It is observed that the pressure

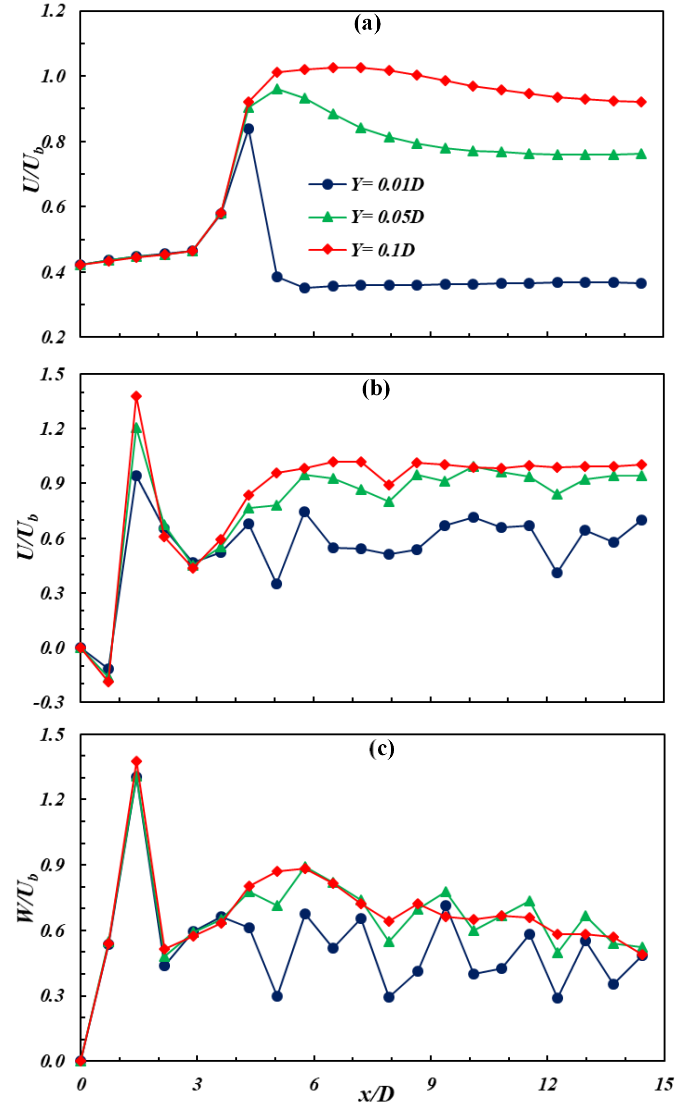


Fig. 9 Near-wall normalized axial (U/U_b) and tangential (W/U_b) velocity distribution along the nozzle length: $Q_r=0$ (a), and $Q_r=1$ (b and c).

drop at the center of the nozzle ($r/D = 0$) is greater than all other radial location in almost every axial position of the nozzle, however, near the nozzle outlet it suddenly reduces. While pressure drop at every radial location increase after the introduction of the tangential ports, at ($r/D = 0.4$) it suddenly decrease. Pressure drop near the wall is gradually increasing after the converging section of nozzle but pressure drop near the nozzle center is nearly constant. It can be concluded that Due to the tangential flow introduction the pressure drop characteristics near the nozzle center response quickly and near the wall vicinity this property change slowly.

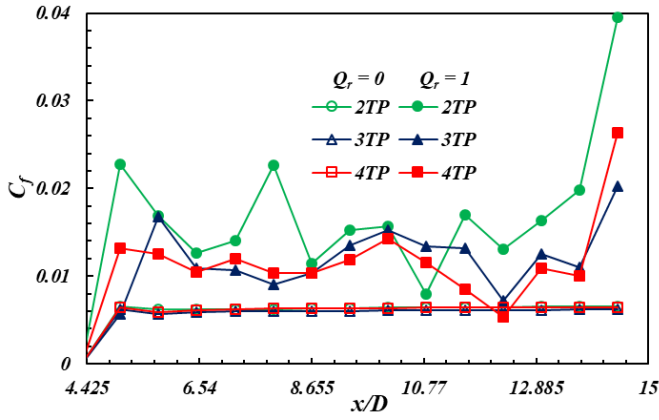


Fig. 10 Skin friction coefficient along the nozzle length.

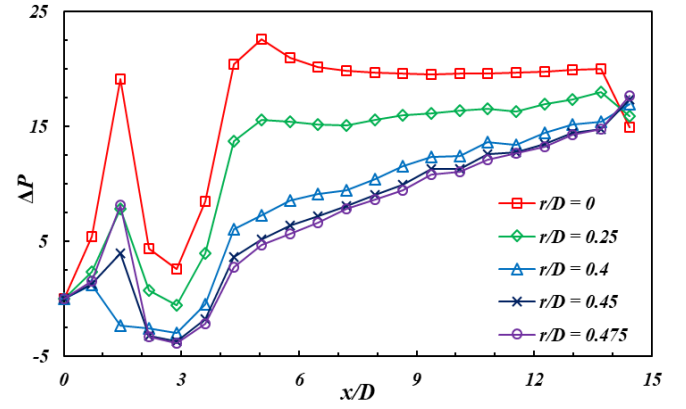


Fig. 11 Pressure drop along the nozzle length for swirling flow.

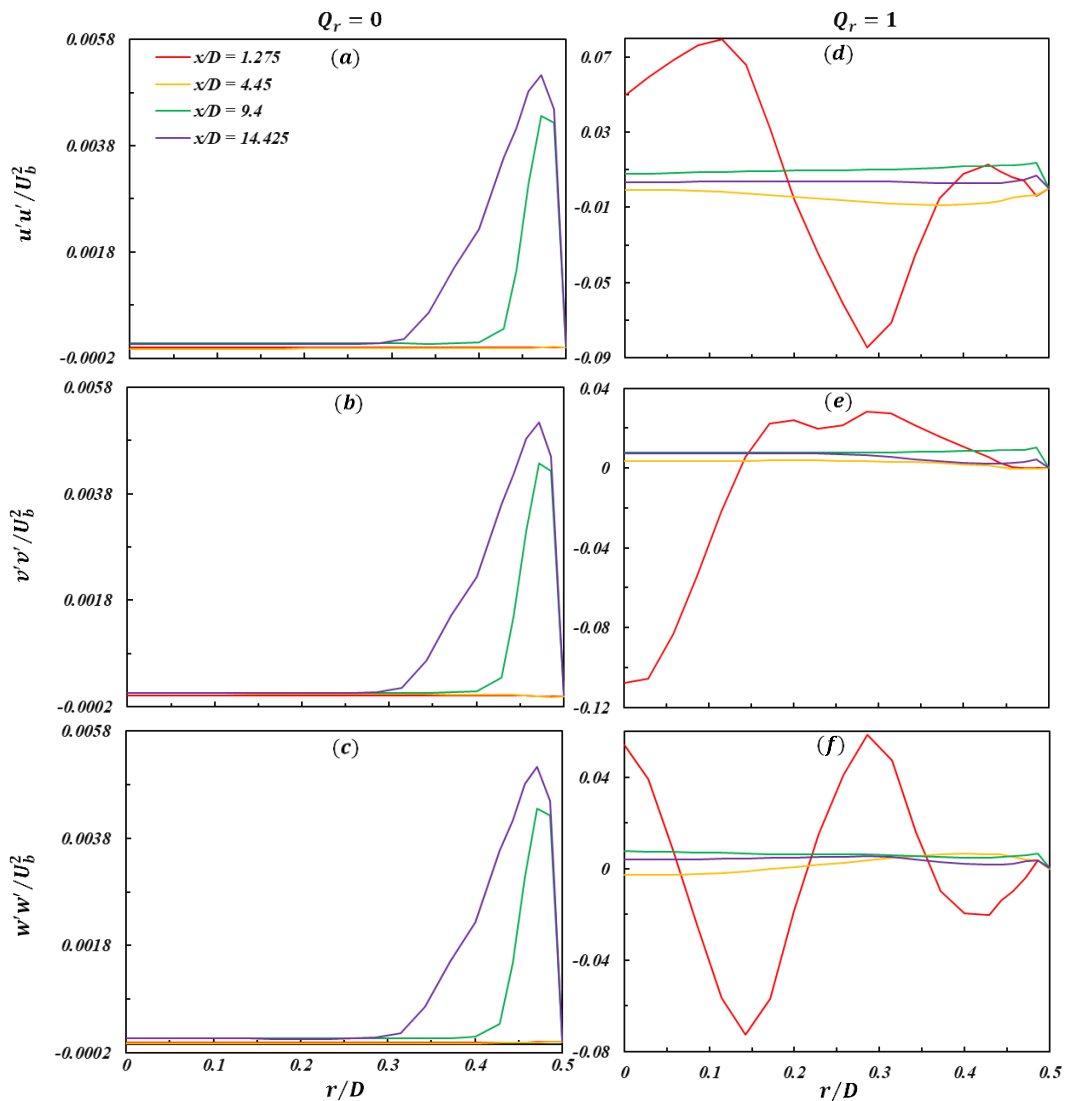


Fig. 12 Turbulent normal stress profiles at different axial locations.

Fig. 12 presents the radial distribution of normalized turbulent normal stress components at various axial locations. It is observed that the turbulent flow characteristic near the wall is very high at $x/D = 9.4$ and $x/D = 14.425$ at no swirl flow ($Q_r = 0$) although at the center of the nozzle the turbulent flow characteristic is very low. Moreover, near the inlet of the nozzle

at $x/D = 1.275$ and $x/D = 4.45$ the overall turbulent flow characteristic is very small in magnitude. On the contrary at swirl flow condition ($Q_r = 1$) near the inlet of the nozzle at $x/D = 1.275$ the overall turbulent flow characteristic is very high. However, the turbulent normal stress near the outlet section at $x/D = 9.4$ and $x/D = 14.425$ is small in these

locations. While at no swirl condition the turbulent normal stress characteristic at the center of nozzle is very low at swirl flow condition, the $u'u'$ and $w'w'$ component is very high at the nozzle center especially at $x/D = 1.275$ due to the

introduction of swirl flow. The overall magnitude of the turbulent normal stress is very small in no swirl flow condition but for swirl condition it is very high.

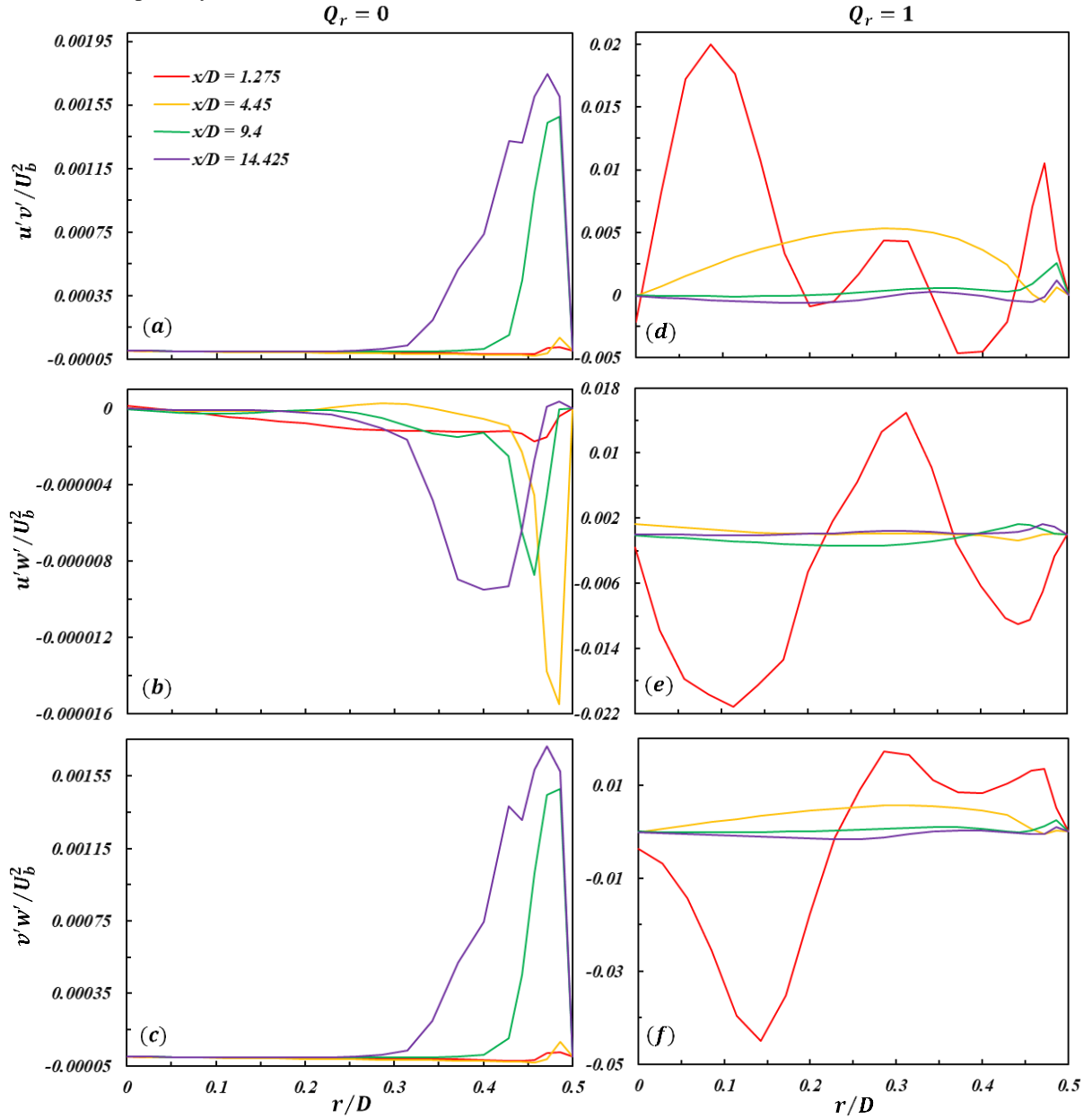


Fig. 13 Turbulent shear stress profiles at different axial locations.

Finally, **Fig. 13** presents the radial distribution of normalized turbulent shear stress components at various axial locations. It is observed that for no swirl flow ($Q_r = 0$) the turbulent shear stress component $u'v'$ and $v'w'$ near the wall is very high at $x/D = 9.4$ and $x/D = 14.425$ although at the center of the nozzle the turbulent shear stress component is very low (**Fig. 13a** and **Fig. 13c**). However, the $u'w'$ component at $x/D = 4.45, 9.4$ and 14.425 is reducing near the wall of the nozzle. Near the inlet of the nozzle at $x/D = 1.275$ the overall turbulent shear stress is uniform and does not deviate much for no swirl flow ($Q_r = 0$). On the other hand at swirl flow condition ($Q_r = 1$) near the inlet of the nozzle at $x/D = 1.275$ all the three component of turbulent shear stress is fluctuates highly and the magnitude of overall turbulent shear stress is

very high. However, the overall turbulent shear stress at $x/D = 9.4$ and $x/D = 14.425$ is very uniform along the radial location for swirl flow. The overall magnitude of the turbulent flow characteristic is very small in for swirl flow compared to the swirl condition.

4. Conclusion

An incompressible turbulent swirling air jet is investigated numerically. In this regard, an axial-plus-tangential swirl flow is considered for non-swirling ($Q_r = 0$) and highly swirling ($Q_r = 1$) cases. Finite volume based commercial software ANSYS Fluent v17 is used in the simulation to investigate mean flow and turbulence characteristics. Governing equations are approximated by the RANS equations and turbulence is

characterized by the SST $k-\omega$ model. The study examines the effect of number of tangential inlets on mean flow behaviors and turbulent characteristics. The magnitude of swirl decay is fluctuates highly before the nozzle converging section and after the nozzle converging section the swirl decay is nearly constant. The boundary layer thickness in swirl flow is found to be the smallest for 2TP. The skin friction coefficient along the nozzle axial position at no swirl flow is uniform and the magnitude is very small. For swirl flow, the skin friction coefficient along the nozzle axial position is fluctuating especially for 2TP. Moreover, the skin friction coefficient at the nozzle exit is the maximum for all the case. Due to the tangential flow introduction, the pressure drop near the nozzle center response quickly and near the wall vicinity this property changes slowly. The turbulent normal and shear stress for no swirl flow is nearly uniform, but for swirl flow it fluctuates the most near the section where the swirl flow is introduced.

Acknowledgements

The first author acknowledges the Department of Electronics and Communication Engineering at Khulna University of Engineering & Technology, Bangladesh for part of the computation facility provided during the study program.

References

- [1] Sloan, D.G., Smith, P.J. and Smoot, L.D., 1986. Modeling of swirl in turbulent flow systems. *Progress in Energy and Combustion Science*, 12(3), pp.163-250.
- [2] Rose, W.G., 1962. A swirling round turbulent jet, *Journal of Applied Mechanics*, vol.29, Trans. ASME, vol. 84, Series E, pp. 616-625.
- [3] Toh, K., Honnery, D. and Soria, J., 2010. Axial plus tangential entry swirling jet. *Experiments in Fluids*, 48(2), pp.309-325.
- [4] Ahmed, Z.U., 2016. An experimental and numerical study of surface interactions in turbulent swirling jets. PhD Thesis, Edith Cowan University, Australia.
- [5] Gore, R.W. and Ranz, W.E., 1964. Backflows in rotating fluids moving axially through expanding cross sections. *AIChE Journal*, 10(1), pp.83-88.
- [6] Jafari, M., Farhadi, M. and Sedighi, K., 2017. An experimental study on the effects of a new swirl generator on thermal performance of a circular tube. *International Communications in Heat and Mass Transfer*, 87, pp.277-287.
- [7] Markal, B., 2018. Experimental investigation of heat transfer characteristics and wall pressure distribution of swirling coaxial confined impinging air jets. *International Journal of Heat and Mass Transfer*, 124, pp.517-532.
- [8] Yajnik, K.S. and Subbaiah, M.V., 1973. Experiments on swirling turbulent flows. Part 1. Similarity in swirling flows. *Journal of Fluid Mechanics*, 60(4), pp.665-687.
- [9] Chang, F. and Dhir, V.K., 1994. Turbulent flow field in tangentially injected swirl flows in tubes. *International journal of heat and fluid flow*, 15(5), pp.346-356.
- [10] KITO, O. and KATO, T., 1984. Near wall velocity distribution of turbulent swirling flow in circular pipe. *Bulletin of JSME*, 27(230), pp.1659-1666.
- [11] Kitoh, O., 1991. Experimental study of turbulent swirling flow in a straight pipe. *Journal of Fluid Mechanics*, 225, pp.445-479.
- [12] Buschmann, M.H., Indinger, T. and Gad-el-Hak, M., 2009. Near-wall behavior of turbulent wall-bounded flows. *International Journal of Heat and Fluid Flow*, 30(5), pp.993-1006.
- [13] Ahmed, Z.U., Al-Abdeli, Y.M. and Guzzomi, F.G., 2016. Corrections of dual-wire CTA data in turbulent swirling and non-swirling jets. *Experimental Thermal and Fluid Science*, 70, pp.166-175.
- [14] Ahmed, Z.U., Khayat, R.E., Maissa, P. and Mathis, C., 2012. Axisymmetric annular curtain stability. *Fluid Dynamics Research*, 44(3), p.031401:1-23.
- [15] Ahmed, Z.U., Khayat, R.E., Maissa, P. and Mathis, C., 2013. Non-axisymmetric annular curtain stability. *Physics of Fluids*, 25(8), p.082104:1-37.
- [16] Lu, P. and Semião, V., 2003. A new second-moment closure approach for turbulent swirling confined flows. *International journal for numerical methods in fluids*, 41(2), pp.133-150.
- [17] Tsai, J.H., Lin, C.A. and Lu, C.M., 1995. Modelling dump combustor flows with and without swirl at the inlet using Reynolds stress models. *International Journal of Numerical Methods for Heat & Fluid Flow*, vol. 5, no. 7, pp. 577-588.
- [18] Gorman, J.M., Sparrow, E.M., Abraham, J.P. and Minkowycz, W.J., 2016. Evaluation of the efficacy of turbulence models for swirling flows and the effect of turbulence intensity on heat transfer. *Numerical Heat Transfer, Part B: Fundamentals*, 70(6), pp.485-502.
- [19] Saqr, K.M. and Wahid, M.A., 2014. Effects of swirl intensity on heat transfer and entropy generation in turbulent decaying swirl flow. *Applied thermal engineering*, 70(1), pp.486-493.
- [20] Nouri-Borujerdi, A. and Kebriaee, A., 2012. Simulation of turbulent swirling flow in convergent nozzles. *Scientia Iranica*, 19(2), pp.258-265.
- [21] Najafi, A.F., Saidi, M.H., Sadeghipour, M.S. and Souhar, M., 2005. Numerical analysis of turbulent swirling decay pipe flow. *International communications in heat and mass transfer*, 32(5), pp.627-638.
- [22] Islam, Md. M., Tasnim, S., and Ahmed, Z. U., 2017. Numerical study of a swirl nozzle at moderate swirl number, *International Conference on Mechanical Engineering and Renewable Energy*, 20-22 December, Chittagong, Bangladesh.
- [23] Islam, S. M., Khan, M. T., Ahmed, Z. U., 2020. Effect of design parameters on flow characteristics of an aerodynamic swirl nozzle, *Progress in Computational Fluid Dynamics*, In press.
- [24] Khan, M. H. U., and Ahmed, Z. U., 2019. Fluid flow and heat transfer characteristics of multiple swirling impinging jets at various impingement distances, *International Journal of Thermofluid Science and Technology*, vol. 6, no. 4, pp. 19060403:1-12.
- [25] Ahmed, Z. U., Al-Abdeli, Y. M., 2017. Flow characteristics due to jet impact at low intensity, In: *Proceedings of Int. Conf. Engineering, Research, Innovation and Education*, Sylhet, Bangladesh, 156, p. 1-6.
- [26] Debnath, S., Khan, M.H.U. and Ahmed, Z.U., 2020. Turbulent Swirling Impinging Jet Arrays: A Numerical Study on Fluid Flow and Heat Transfer. *Thermal Science and Engineering Progress*, p.100580.
- [27] Ahmed, Z.U., Khan, M.H.U., Khayat, R.E. and Tasnim, S., 2018, July. Effect of flow confinement on the hydrodynamics and heat transfer characteristics of swirling impinging jets. In *AIP Conference Proceedings* (Vol. 1980, No. 1, p. 040008). AIP Publishing LLC.
- [28] Thomas, B.K., Ahmed, Z.U., Al-Abdeli, Y.M. and Matthews, M.T., 2013. The optimisation of a turbulent swirl nozzle using CFD. *Proceedings of the Australian Combustion Symposium*, November 6-8, Perth, Australia.
- [29] Menter, F.R. and Egorov, Y., 2010. The scale-adaptive simulation method for unsteady turbulent flow predictions. Part 1: theory and model description. *Flow, Turbulence and Combustion*, 85(1), pp.113-138.
- [30] Ahmed, Z.U., Al-Abdeli, Y.M. and Matthews, M.T., 2015. The effect of inflow conditions on the development of non-swirling versus swirling impinging turbulent jets. *Computers & Fluids*, 118, pp.255-273.
- [31] Ahmed, Z.U., Al-Abdeli, Y.M. and Guzzomi, F.G., 2017. Flow field and thermal behaviour in swirling and non-swirling turbulent impinging jets. *International Journal of Thermal Sciences*, 114, pp.241-256.

Thermal Hydraulic Analysis of a Nuclear Reactor due to Loss of Coolant Accident with and without Emergency Core Cooling System

Pronob Deb Nath, Kazi Mostafijur Rahman, Md. Abdullah Al Bari*

Department of Mechanical Engineering, Khulna University of Engineering & Technology, Khulna-9203, BANGLADESH

Received: June 05, 2020, Revised: June 26, 2020, Accepted: June 26, 2020, Available Online: June 29, 2020

ABSTRACT

This paper evaluates the thermal hydraulic behavior of a pressurized water reactor (PWR) when subjected to the event of Loss of Coolant Accident (LOCA) in any channel surrounding the core. The accidental break in a nuclear reactor may occur to circulation pipe in the main coolant system in a form of small fracture or equivalent double-ended rupture of largest pipe connected to primary circuit line resulting potential threat to other systems, causing pressure difference between internal parts, unwanted core shut down, explosion and radioactivity release into environment. In this computational study, LOCA for generation III+ VVER-1200 reactor has been carried out for arbitrary break at cold leg section with and without Emergency Core Cooling System (ECCS). PCTRAN, a thermal hydraulic model-based software developed using real data and computational approach incorporating reactor physics and control system was employed in this study. The software enables to test the consequences related to reactor core operations by monitoring different operating variables in the system control bar. Two types of analysis were performed -500% area break at cold leg pipe due to small break LOCA caused by malfunction of the system with and without availability of ECCS. Thermal hydraulic parameters like, coolant dynamics, heat transfer, reactor pressure, critical heat flux, temperature distribution in different sections of reactor core have also been investigated in the simulation. The flow in the reactor cooling system, steam generators steam with feed-water flow, coolant steam flow through leak level of water in different section, power distribution in core and turbine were plotted to analyze their behavior during the operations. The simulation showed that, LOCA with unavailability of Emergency Core Cooling System (ECCS) resulted in core meltdown and release of radioactivity after a specific time.

Keywords: LOCA; VVER-1200; PCTRAN; ECCS; Thermal-hydraulic behavior.



This work is licensed under a [Creative Commons Attribution-NonCommercial 4.0 International](https://creativecommons.org/licenses/by-nc/4.0/)

1. Introduction

VVER-1200 is the utmost type of VVER pressurizer water reactor (PWR) meaning Vodo Vodyanoi Energetichesky Reaktor or water-water energetic reactor with improved safety features design and developed by OKB Gidropress, Russia. It is a thermal neutron pressurizer reactor used water not only as coolant but also as moderator. It consists of two circuit namely the primary circuit, where the primary coolant receives heat from reactor core and the secondary circuit where the heat supplied to produce electricity [1] with four cooling loops, main circulation pump, accumulator tanks of the ECCS, relief and safety emergency valves. It's said to be a generation III+ reactor with improved safety features like sacrificial concrete core catcher layer, passive heat removal system, etc. Inside the core, the primary coolant deposit at 155 bar so that it can avoid vaporization at high temperature [2]. Any leakage in the coolant circuit can lose large amount of coolant from Reactor Cooling System (RCS) result in Design Basis Accident or Beyond Design Basis Accident according to the flow from RCS.

Design-basis accident (DBA) is a postulated accident that a nuclear facility must be designed and built to withstand without loss to the systems, structure and components necessary to ensure public health and safety. DBA concept is very feasible for abnormal operations in a nuclear power plant to vindicate performance requirements for reactor system, structure and components after anticipated operational occurrence. Beyond

Design Basis Accident (DBA) which have extremely low probability of happening is a sequence of accident which may or may not lead to core degradations. DBA postulate for each type of reactor covering different type of failure combinations like reactivity-initiated accident, loss of flow transients, Loss of coolant accidents, fuel handling accidents and so on. The DBA is prescribed to different limiting condition for cladding temperature, local fuel cladding oxidation, ZrO₂ mass cladding, whole body dose and others [3].

LOCA is one of most important and common DBAs for each reactor design depending on size of break. LOCA assumed that one of inlet or outlet pipe from circulating pump to reactor vessel completely broken or partially broken and free discharge of primary coolant from both broken ends occur. LOCA can be happening for different reasons like, material defects of different systems, material fatigue in pipe/shell, external impacts like heavy loads or missiles, device failure during operation due to different reasons, inadvertent opening on primary system boundary and so on. The nuclear reactor core has different emergency system to mitigate different type of accident depend on the incident or accident type.

There are various safety features in VVER 1200 reactor plants. VVER 1200 reactors are capable of sustaining initiating events as well as their consequence under accident conditions during a long period within the boundaries of design safety criteria and assured by following structural and design features

*Corresponding Author Email Address: pronobdebnaathpartho@gmail.com

like (a) increased coolant volume above the core (b) increased coolant volume in the primary circuit in respect to fuel mass and thermal power of the core (c) increased capacity of pressurizer (d) reliable natural circulation (e) considerable water inventory in horizontal SGs on the secondary side [2].

The primary coolant system of reactor core is the system which is heated at reactor core flows into steam generator. The primary coolant flow through heat exchanger tube boiling the coolant in secondary cooling system which flow outside of heat exchanger tube that drive the turbine generator and creates mechanical energy from heat energy. After that, the primary coolant comes from steam generator flow back to reactor core using compressed pump.

The leakage size within reactor coolant pressure boundary divided into two group namely Large Break Loss of Coolant Accident (LBLOCA) and Small Break Loss of Coolant Accident (SBLOCA). Reduction of water temperature during Emergency core cooling system injection drop in about 50°C-70°C the break can be categorized as small breaks and for large break reduction of temperature about 120°C-150°C [4]. The primary system remains at high pressure after the occurrence of LOCA and the core remain covered. Coolant flows inside the primary system as soon as the pumps are tripped due to automatically or manually gravity control phase separation occurrence. The next subsequent events depend on the overall behavior of the primary and secondary system. Automatic and operator-initiated mitigation measurements influenced the overall behavior. Reactor design, break size, location of the break, core bypass system, operator interactions have influenced the scenario. Each alternative action has much impact to make a huge difference on the LOCA. The LBLOCA classical DBA for reactor core where one of the inlet pipes from the circulating pump is completely non-functional or free discharge of primary coolant from both broken ends which referred as Double Ended Guillotine break. LOCA have those following phase (a) BLOWDOWN PHASE, 0-20 seconds (b) BYPASS PHASE, 20-30 seconds (c) REFILL PHASE, 30-40 seconds (d) REFLOODING PHASE, 40-250 seconds (e) LONG TERM COOLING >250 seconds.

The VVER-1200 has following active and passive system to mitigate different accident: (i) The Primary Circuit Emergency with Planned Cooldown and Spent Fuel Cooling (ii) Low Pressure Emergency Injection System to supply Boric Acid Solution (iii) Emergency Core Cooling System (iv) Passive Core Flooding System (v) Emergency Boron Injection System (vi) Emergency Gas Removal System (vii) Primary Overpressure Protection (viii) Secondary Overpressure Protection (ix) Passive Heat Removal System (x) Steam Generator Emergency Cooldown System (xi) Main Steam-line Isolation System (xii) Double Envelope Containment and Core Catcher [1].

Personal Computer Transient Analyzer (PCTRAN) is a nuclear reactor transient and accident simulation tool that operates on a personal computer for learning different nuclear reactor behavior under different condition. Concepts of neutron multiplication, criticality, thermal hydraulic safety parameters, transient analysis, accidental dose estimation and Xenon poisoning and feedback in live simulation statistical analyses can be carried out. The PCTRAN-VVER1200 simulator version 1.2.0 available from Micro-Simulation Technology for VVER-1200 reactor for thermal output of 3200 MWt with two loops of

reactor coolant system represented as loop A and loop B use for the numerical simulation purpose. It has shown the major systems and components of the reactor like RCS, the Emergency Core Cooling System (ECCS), the Pressurizer with its components, the Low-Pressure Injection System (LPIS), Feed/bleed water system, Steam Generator, Accumulator, different safety valves and different components of the NPP. The components like pump, valves indicating red colored are operating and open system and white indicating colored indicate idle and closed in the mimic interactive. Those components can be switch on or off just by clicking on them in the interactive display. It has two interface, the main interface for different component and Dose mimic interface for radioactivity display.

Transient behavior simulation has been successfully benchmarked by using PCTRAN approved by International Atomic Energy Agency (IAEA). PCTRAN based on end-users input data with a reactor point kinetics model for analysis nuclear safety related concepts and phenomena that could be easily explained with the simulators along with understanding of valuable technological differences in various designs of PCTRAN products. A high-resolution color mimic of the Nuclear Steam Supply System (NSSS) and containment displays are the status of important parameters and allows simulation of operator actions by interactive control.

Though the main purpose of this simulator is operator training and a dynamic test to validate the control logics in reactor regulating system (RRS), this simulator is also used for research purposes. Like, Mollah review about PCTRAN simulator for safety and transient analysis of PWR [5]. Ibrahim et al. showed Simulation of Safety and Transient Analysis of a Pressurized Water Reactor using the PCTRAN [6]. Yi-Hsiang Cheng et al. integrated development of accident dose consequences simulation software for nuclear emergency response applications using PCTRAN software [7]. Also further they analyze the Improvement of accident dose consequences for nuclear emergency response applications using PCTRAN simulator [8]. Khan and Islam published an article on a PCTRAN based investigation on the effect of inadvertent control rod withdrawal on the thermal-hydraulic parameters of a VVER-1200 nuclear power reactor [9]. Fyza et al. analyzed the thermal-hydraulic parameters of VVER-1200 due to loss of coolant accident concurrent with loss of offsite power with PCTRAN and conclude with PSAR (Preliminary Safety Assessment Report) regarding LOCA [10]. Tube rupture in steam generator and transient analysis of VVER-1200 using PCTRAN simulation is conducted by Saha et al. [11].

Only a limited research works on VVER-1200 new generation III+ reactor related topic has been conducted. In this study, the thermal hydraulics behavior of VVER-1200 reactor due to LOCA with 500% area with and without ECCS are simulated by using PCTRAN software. Thermal hydraulic parameters like, coolant dynamics, heat transfer, reactor pressure, critical heat flux, temperature distribution in different sections of reactor core have also been investigated in the simulation. The flow in the reactor cooling system, steam generators steam with feed-water flow, coolant steam flow through leak level of water in different section, power distribution in core and turbine were plotted to analyze their behavior during the operations.

2. Methodology

The numerical analysis was carried out by PCTRAN VVER1200 v-1.2.0. By this software package one can simulate a variety of accident and transient condition for VVER-1200 reactor nuclear power plants. User can select initial conditions corresponding to different parameter and initiate malfunctions to analyze as desired. Following analysis had been conducted by this software- normal operating control, stream line break or LOCA, recirculation pump trip, turbine trip, station blackout, inadvertent rod withdrawal or insertion, Boron dilution transient, steam generator tube rupture, feedwater transient, anticipated transient without scram and any combination of above. The user can manually trip the reactor pump, open or close valve, override ECCS, change operational set points. The plant mimic system has the ability to freeze, back track, snap a new initial condition, change the simulation speed, trend plot by selected variable for conducting system analysis.

The simulator based on nuclear reactor theory and solution technique by Six- group point kinetics model which is a point kinetics equation with six delayed neutron groups and reactivity control from external sources and feedback. The model equations are described in the literature by A.S. Mollah [5]. The initial steady state conditions of the plant were Reactor Power at 100% with RC Pressure 155 bar and Core Average Temperature 306.9°C with BOC (Beginning of Cycle) of Steam Generator (SG) pressure 70 Bar. After setting up the initial and boundary conditions, the necessary operating parameters were measured for the analysis of reactor performance. Default values of VVER-1200 reactor were given which can be changed to initial value as required. Different type of malfunctions with initial value, fraction percentage, delay time will be set initially to run simulation.

After completion of simulation, transient plot of different variables like flow rate, coolant activity, concentration of materials, dose rate, fraction, energy, level of water, mass of different element, power of different system, pressure, radioactivity, enthalpy temperature, void fraction could be created with respect to time and other variables. The sequence of simulation of the whole process is shown in Fig. 1.

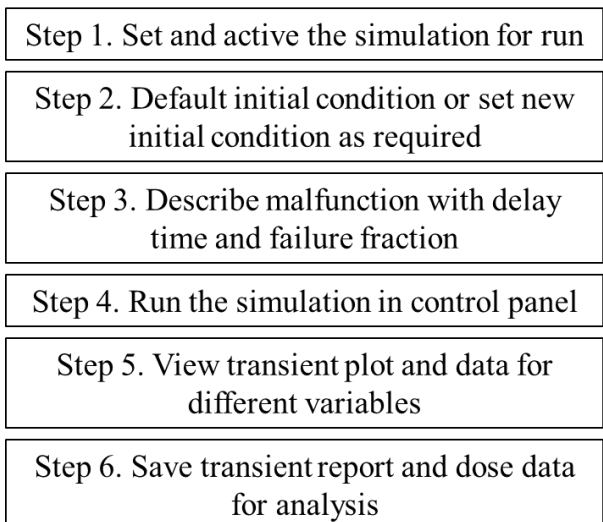


Fig. 1 Steps/order of simulation in PCTRAN.

3. Computational Results and Discussion

In this computational analysis two cases have been considered for investigation. First case accounted for a design basis loss of coolant accident where the ECCS was in operation and the second case was for a beyond design basis loss of coolant accident without any type of ECCS and passive cooling system. After conducting the computational analysis, the plot relevant to different parameters were discussed.

3.1 Analysis of LOCA at cold leg with all ECCS

In this simulation 500 cm² (25.23 cm diameter) break in cold leg simulation have been conducted. LOCA with break at cold leg has serious impact because safety injection system makeup water lost through this break. The simulation carried out using manually defined malfunction in the code control at cold leg with 500 cm² failure fractions after 5 seconds of the simulator to run at steady state condition as shown in Fig. 2. To minimize the coolant loss, the RCPs manually tripped. There was a rupture icon in the cold leg with primary coolant loss rate appears in the simulator. Safety injection systems started automatically after reactor trip signal generated on because of the low pressure.

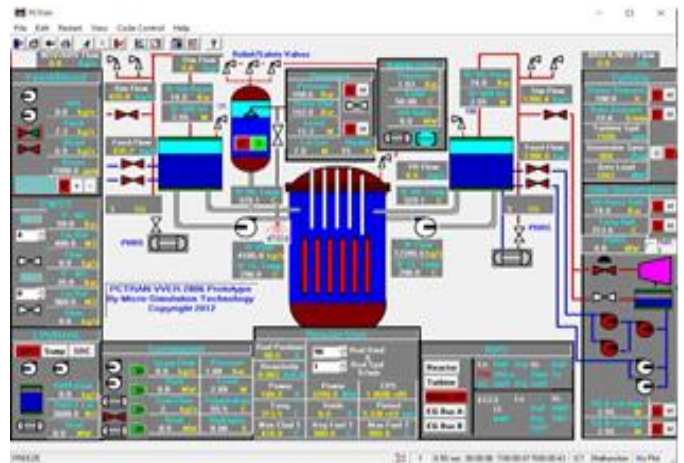


Fig. 2 Graphical user interface of PCTRAN: Initiation of 500 cm² cold leg LOCA.

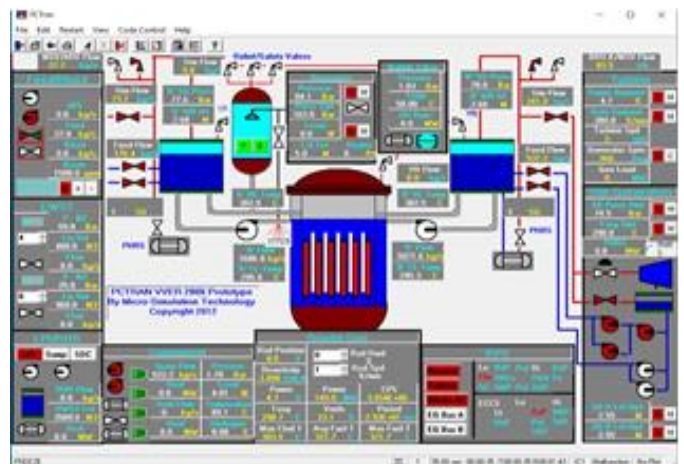
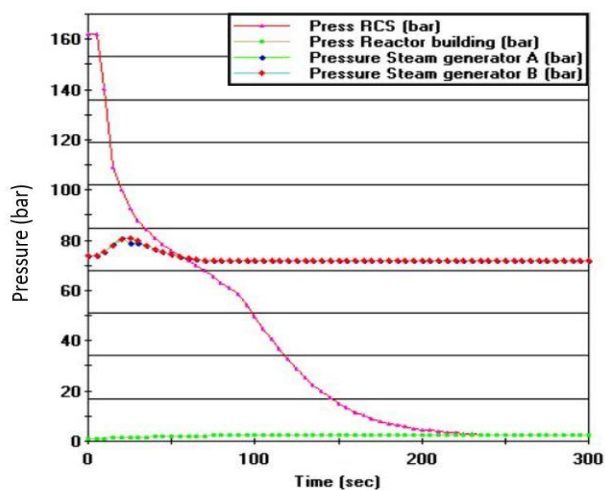
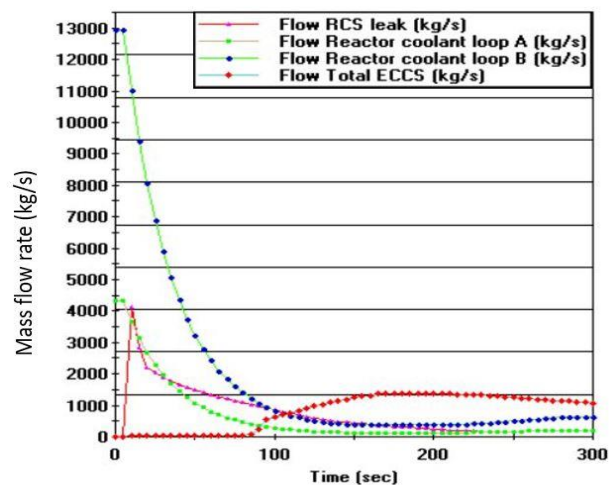


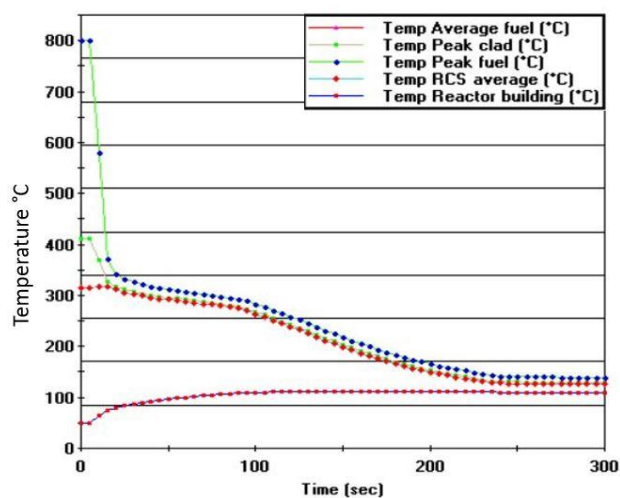
Fig. 3 Graphical user interface of PCTRAN: Reactor trip and actuation of HPIS, RB spray pump.



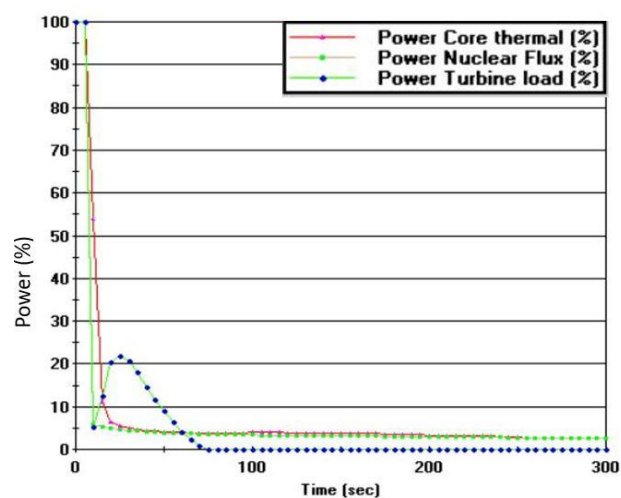
(a)



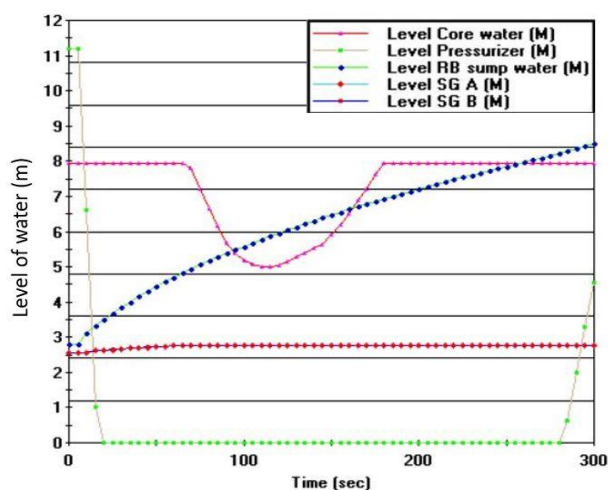
(b)



(c)



(d)



(e)

Fig. 4 (a) Pressure of RCS, RB, SGs (bar) for cold leg break (b) Mass flow rate of RCS leak, reactor coolant loops, ECCS flow water (kg/s) (c) Temperature of average fuel, RCS, peak clad, peak fuel, RB (°C) for cold leg break (d) Core thermal power (%), Nuclear flux power (%), Turbine Load power (%) for cold leg break (e) Water level of core, pressurizer, RB sump, SGs (m) for cold leg break.

Fig. 3 shows that, ECCS actuated High Pressure Injection System (HPIS) at 15s when the RCS pressure was lower than the nitrogen pressure accumulator tank. Although HPIS along with recovery refueling water storage tank, reactor building spray help to provide boronated water. LPIS provide enough water to maintain the core submerged and responsible for long term cooling of residual heat in reactor. Compared to large break LOCA, the depressurization occurs relatively slowly in SBLOCA. Upon actuation of accumulator, ECCS water flow started to exceed the coolant discharge rate and the reactor vessel water level slowly rose again and core level water restored as illustrated in **Fig. 4 (e)**. The RCS pressure fall down from initial steady 160 bar to about 3 bar after 200 second from the onset of accident. The Steam Generator A (SG-A) and SG-B pressure initially increased after accident from 74 bar to 81 bar in 30 second for sudden loss of coolant but after 65 second both SGs reached to equivalent pressure 72 bar as shown in **Fig. 4 (a)**. The process of depressurization was very rapid slowing down the reactor coolant leak rate. After being emptied the pressurizer during initial occurrence, RCS leak rapidly decreased as the pressure altitude change fast. RCS leak initially started after 5 seconds of the incident with 4150 kg/s mass flow rate which slowly decreased with respect to time after 40 seconds of the accident. The leak loss of mass flow become equal with reactor coolant loop B flow at 105 seconds which was about 390 kg/s. After 220 seconds the mass flow rate become very slow but it needed more time to stop completely. ECCS started after 85 seconds with gradual mass flow rate highest of 1390 kg/s. After 245 seconds, the ECCS slow down. The reactor coolant loop A has 4300 kg/s mass flow rate, coolant loop B has highest 13000 kg/s mass flow rate which decrease very rapidly and stable in 150 seconds to 225 seconds at 390 kg/s in **Fig. 4 (b)**. For SBLOCA initiation reactor coolant release very high flow rate through break, which loss rate decrease due to HPIS actuation and depressurization of primary system.

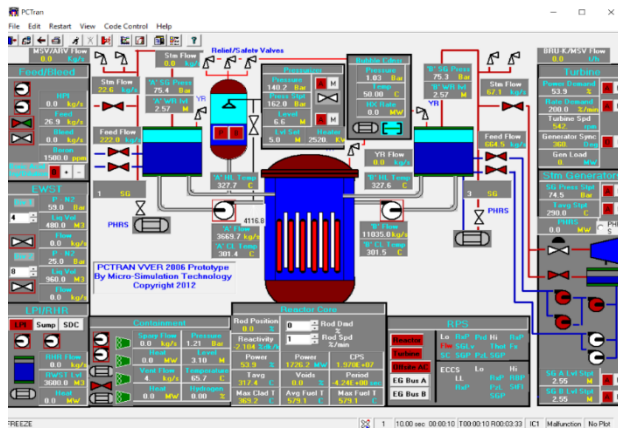
In the meantime, emergency accumulator water system active to provide enough makeup water in RCS to maintain the core submerged in water so that during the transient event, fuel and cladding temperature never rise to critical value shown in **Fig. 4 (c)**. Highest peak clad temperature and peak fuel temperature can't rise to critical value to melt the core as the control rods are fall down after 7s and huge makeup water from ECCS, HPIS active due to this transient event. Fuel peak temperature, clad peak temperature, average fuel temperature falls from respectively 800°C, 415°C, 320°C to 150°C, 140°C, 110°C after 300s. The sump water level in reactor building increase from 40°C to 100°C due to recirculation through RWST with LPIS. The accident is assumed to happened when the reactor operating at full 100% power. Due to the occurrence of LOCA in cold break, the simulation shows reactor trip after 40s which indicate core thermal power and nuclear flux fall to 5% and decay heat power continuously extend for next few cycles to cooled down to zero in **Fig. 4 (d)**. The turbine load initially dropped after LOCA which increase for following 20s and again decrease to zero as turbine trip after the malfunction.

3.2 Analysis of LOCA at cold leg without ECCS or any passive heat removal system

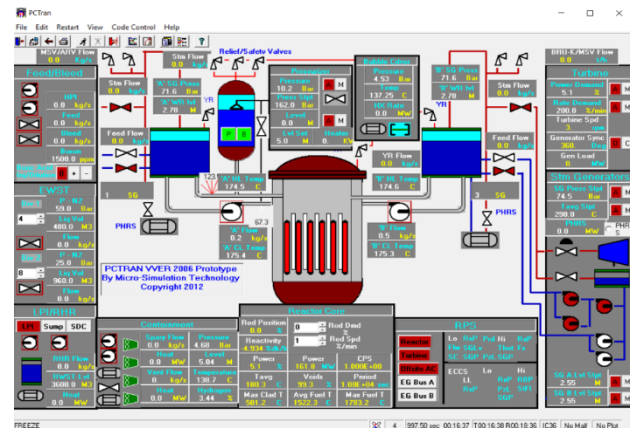
In VVER-1200, the emergency core cooling system is consisting with not only HPIS, but also it has LPIS, passive heat removal system, emergency accumulator water system, feed water system, reactor building spray pumps and refueling water storage tank with it to prevent all kind of accident including DBA and BDBA to tackle the situation in emergencies. Whenever ECCS face any kind of accident signal, it automatically got actuated to keep the core under water and cooled it down in order to eliminate any serious impact on the total system and environment with working personnel. When the ECCS can't operate as needed, then this scenario can turn into severe accident with core meltdown and fuel degradation.

In this case, all the ECCS equipment were disabled and reactor coolant pump was turned off manually, with a 500 cm² LOCA in cold leg. Though, it is a hypothetical cause with unavailability of all those ECCS equipment but following the Fukushima Daiichi accident caused by earthquake and tsunami where all the emergency system failed and level/class 7 disaster happened, possible consequences of this type of accident needs to be analyzed.

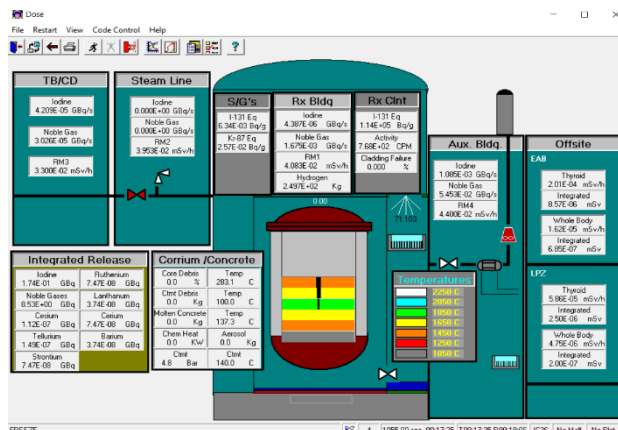
For LOCA accident without enabling the ECCS, the reactor trips instantaneously and after 9 seconds all the control rods trip down to reactor core with pressurizer emptied within 20 seconds due to very rapid depressurization as shown in **Fig. 5 (a)**. The fuel temperature continuously increases due to absent of all ECCS and passive heat removal system. With increased cladding temperature, the interaction between the cladding and steam was accelerated. Hydrogen concentration inside reactor increased with time and shortly after the core uncover, as depicted in **Fig. 5 (b)** about 980 seconds after the accident, the hydrogen concentration in the reactor building exceeded 5%. Fuel temperature increased as time goes by resulting the reactor core starts to melt. In Dose Mimic, the core melting process can be observed in **Fig. 5 (c)**. Molten fuel collapse into the bottom of the vessel as there is nothing that can cooled the core materials. The vessel lower head may then heat up to the melting point, too. **Fig. 5 (d)** illustrates that, the molten debris with molten core concrete interaction with vessel penetration may drop into the containment cavity floor takes around 3000 seconds for 500cm² LOCA at cold leg without ECCS. During the fuel damage process, first the fission gas in the cladding may leak out. Later, if the fuel and cladding continue their degradation, radionuclides will also be released. In addition to iodine and noble gases, there are alkali metals, tellurium, barium, cerium, lanthanides, etc. The elevated concentration of these radionuclides would find their ways through the vessel break, relief valves, and containment leakage into the environment. The molten metal interacts with concrete and forms a slump. At lower temperatures, degassing of concrete occurs and both steam and carbon dioxide can be released. At higher temperatures concrete can also be molten and mixed with metals. In the event that the molten core heats up the vessel bottom and melts through it, the debris, called corium, falls into the reactor cavity.



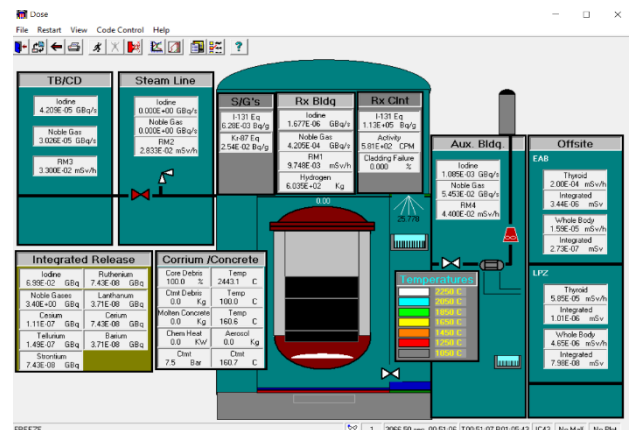
(a)



(b)



(c)

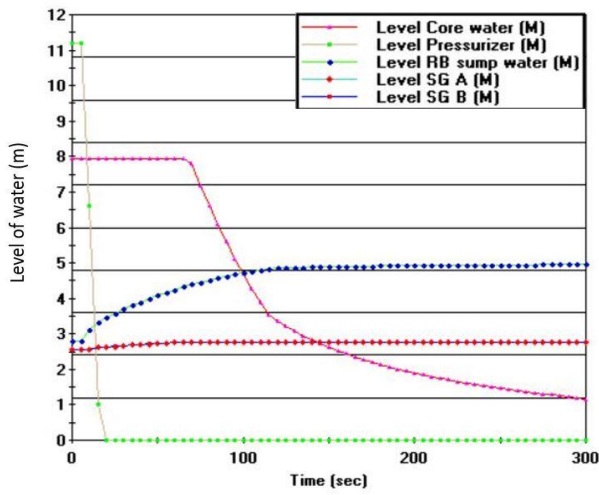


(d)

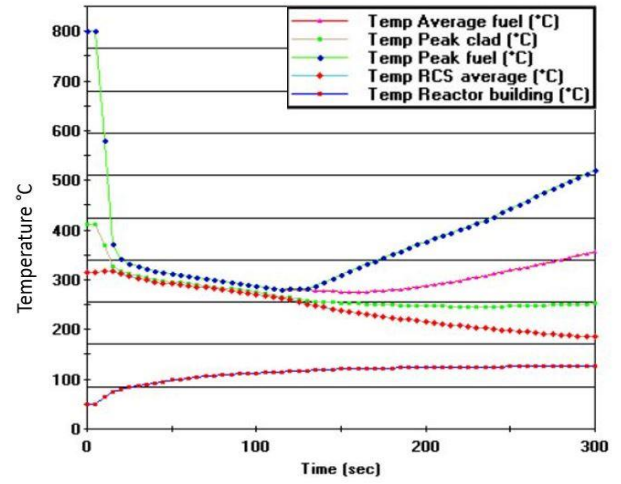
Fig. 5 Graphical user interface of PCTRAN: (a) Reactor trip for LOCA without ECCS (b) Complete core uncover (c) Beginning of core melt (d) Molten core-concrete interaction (MCCI) with vessel penetration.

For LOCA at cold break, the reactor coolant system leak and loops fluid decrease rapidly. At the time of emptying of pressurizer in first few seconds, coolant leak rate rapidly decreased as the pressure elevation of break firstly change. From **Fig. 6 (a)**, level of reactor building sump slowly grew up to a certain point until the recirculation process terminated and there left no water to carry the poison. Level of core water started to decrease very slowly at about 73 seconds. There created a tube rupture loop at cold leg after 350 seconds. In **Fig. 6 (b)**, different temperatures were plotted as respect to time for initial 300 seconds. Due to increasing the sump in reactor building, temperature also increased as followed by the sump. Initially after the accident, the control rod fell down to the core but without the activity of any coolant flow inside the core, the power slowly rose by chain reaction. Before that, the core water level and control rods minimized the temperature about 140 seconds until all the remaining water vaporized totally. After the core fuel emersion, temperature rapidly increased due to unavailability of coolant. Increase in Zircaloy cladding temperature with fuel temperature accelerated the reaction between Zirconium and water. Hydrogen gas accumulation inside reactor building occurred quickly at the top of building which can get exploded when it increased to 5%. The Zirconium cladding distortion increased very high; fraction rate about 42 in 1500 seconds whereas Hydrogen buildup was 8%

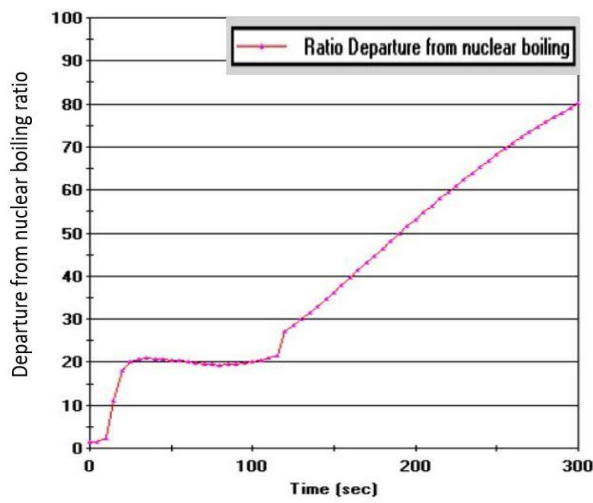
at that time. DNBR or departure from nuclear boiling is the ratio of critical heat flux at specific location to operating local heat flux at that location. In all NPP, DNBR must be greater than one but it can't allow to increase more than 95. From the **Fig. 6 (c)**, it is observed that the DNBR increased very slowly as local heat flux can't able to cross limit until all the coolant system loss and its critical value was about 80. When the local flux was higher than critical heat flux, the core materials melted down for increasing heat flux. Fuel Doppler reactivity is the fractional change in reactivity caused by fuel temperature. Until it's less than one, there was no harm of reactivity but after explosion of the reactor building beyond 980 seconds, reactive substance released to atmosphere. As it increased after the loss of coolant accident, it progressed very much and spread radioactive materials as shown in **Fig. 6 (d)**. **Fig. 6 (e)** shows the comparison between LOCA for different temperature in fuel (TF), average fuel (TAVG), peak fuel (TFPK), peak clad (TPCT) with and without ECCS for first 300s. Initially after the accident, all ECCS activated when the control rod submerged with fuel inside the core, hence temperature fell down for both conditions. But unavailability of ECCS in second case, temperature began to rise when all the water inside core vaporized and fuel with control rod became unstable due to active heat generation.



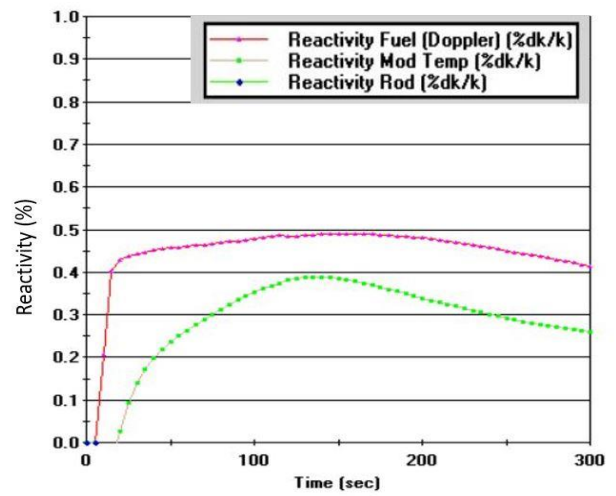
(a)



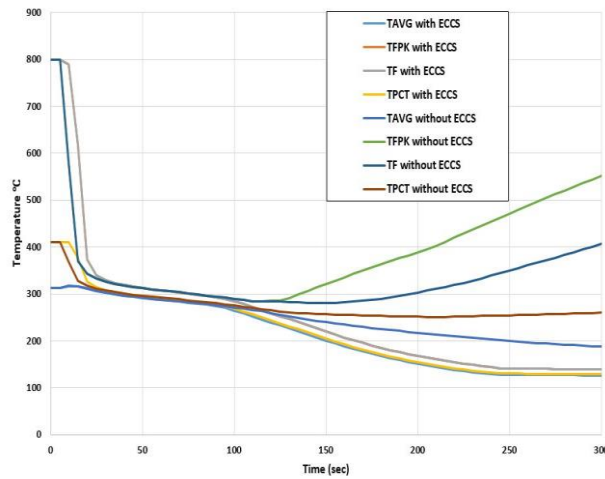
(b)



(c)



(d)



(e)

Fig. 6 (a) Level of core, pressurizer, SGs, RB sump water for LOCA at cold leg without ECCS (b) Temperature of average fuel, RCS, peak clad, peak fuel, RB (°C) for LOCA cold leg break (c) DNBR for LOCA without ECCS (d) Fuel Doppler (%), rod (%), modifier reactivity (%) for LOCA without ECCS (e) Temperature of different component with and without ECCS for LOCA at cold leg.

4. Conclusion

In this study, numerical study has been conducted to investigate the different thermal hydraulics characteristics of nuclear power plant due to loss of coolant accident with and without ECCS. Loss of coolant accident may be a type of postulate event but the probability of happening it in any kind of nuclear reactor plant have enough chance due to different reasons. LOCA accident with both design basis accident analysis and beyond design basis accident analysis are employed in this paper. From the results following conclusion could be drawn:

- Design Basis Accident and Beyond Design Basis Accident both must be mitigated before they are harmful for environment and mankind. A simple Design Basis Accident can turn into serious disaster if it won't handle properly. Risk of radioactive material can be spared if proper maintenance isn't taken care off. Serious accident is not only dangerous for human, but also for every life on that area.
- Different type of thermal hydraulics behaviors like pressure, flow rate, water level in different sections, clad fuel temperature, feed water cooling system, power and many things can be investigated through LOCA analysis. From numerical simulation for LOCA without ECCS transient behaviors and core degradation dose mimic it is found that it takes 3066 seconds to complete core meltdown for 500% area or (25.23 cm diameter) failure fracture. Different arbitrary failure fraction takes different time to conclude in MCCI but reactivity release must be controlled. Design basis LOCA show good agreements with Primary Safety Analysis Safety report (PSAR) but in case of BDB LOCA occurring without ECCS, the core melting process is not able to mitigate the accident.

References

- [1] Gidropress. "Status report 108 - VVER-1200 (V-491), [https://aris.iaea.org/PDF/VVER-1200\(V-491\).pdf](https://aris.iaea.org/PDF/VVER-1200(V-491).pdf)" 2011, Advanced Reactors Information System (ARIS).
- [2] Gidropress. "Status report 107 - VVER-1200 (V-392M), [https://aris.iaea.org/PDF/VVER-1200\(V-392M\).pdf](https://aris.iaea.org/PDF/VVER-1200(V-392M).pdf)" 2011 Advanced Reactors Information System (ARIS).
- [3] C. VITANZA, "DISCUSSION ON EXPERIMENTAL METHODS TO DERIVE LOCA SAFETY LIMIT" Journal: 經濟研究, 2018, Session 3, pages 224-232. https://wwwpub.iaea.org/MTCD/publications/PDF/te_1320_web/t1320_part2.pdf
- [4] Ghafari, M., Ghofrani, M.B. and D'Auria, F., 2018. Boundary identification between LBLOCA and SBLOCA based on stratification and temperature gradient in two-phase PTS. *Annals of Nuclear Energy*, 115, pp.430-441.
- [5] Mollah, A.S., 2018. PCTRAN: Education Tool for Simulation of Safety and Transient Analysis of a Pressurized Water Reactor. *International Journal of Integrated Sciences and Technology*, 3, pp.1-10.
- [6] Ibrahim, S.J., Ewim, D.R. and Edeoja, O.A., 2013. Simulation of Safety and Transient Analysis of a Pressurized Water Reactor using the Personal Computer Transient Analyzer. *Leonardo Electronic Journal of Practices and Technologies*, 22, pp.93-105.
- [7] Cheng, Y.H., Shih, C., Jiang, S.C. and Weng, T.L., 2008. Development of accident dose consequences simulation software for nuclear emergency response applications. *Annals of Nuclear Energy*, 35(5), pp.917-926.
- [8] Cheng, Y.H., Shih, C., Jiang, S.C. and Weng, T.L., 2008. Improvement of accident dose consequences simulation software for nuclear emergency response applications. *Annals of Nuclear Energy*, 35(10), pp.1864-1877.
- [9] Khan, A.H. and Islam, M.S., 2019. A Pctran-Based Investigation On The Effect Of Inadvertent Control Rod Withdrawal On The ThermalHydraulic Parameters Of A Vver-1200 Nuclear Power Reactor. *Acta Mechanica Malaysia (AMM)*, 2(2), pp.32-38.
- [10] Fyza, N., Hossain, A. and Sarkar, R., 2019. Analysis of the thermal-hydraulic parameters of VVER-1200 due to loss of coolant accident concurrent with loss of offsite power. *Energy Procedia*, 160, pp.155-161.
- [11] Saha, A., Fyza, N., Hossain, A. and Sarkar, M.R., 2019. Simulation of tube rupture in steam generator and transient analysis of VVER-1200 using PCTRAN. *Energy Procedia*, 160, pp.162-169.

The Effect of Various Types of Constant and Time Dependent Heating on Human Tissue: A Finite Element Approach

Mridul Sannyal* and Abul Mukid Md. Mukaddes

Department of Industrial and Production Engineering, Shahjalal University of Science and Technology, Sylhet-3114,
BANGLADESH

Received: May 31, 2020, Revised: June 29, 2020, Accepted: June 30, 2020, Available Online: July 01, 2020

ABSTRACT

Cancer is one of the most leading causes of death now worldwide. Most of the cancer therapy aims to raise the temperature of the cancerous tissue above a therapeutic value and thermally kill or destroy it. Minimizing the damage of the healthy cells surrounding the infected cells is one of the major concerns of these therapies. Precise acknowledgment of the temperature profile of living tissue during therapy is of utmost necessity for this purpose. Towards that direction, this paper presents an unsteady finite element model of the bioheat equation to analyze the temperature distribution during the thermal therapy. A C language based system has been developed to solve the unsteady part of the problem employing Crank-Nicolson method and to solve the linear problem employing the Gauss elimination technique. Using this system, we investigate thermal behaviors in human tissues subjected to constant, sinusoidal spatial and surface, point, and stochastic heating. It was found that surface heating is beneficial for treating skin surface cells, while laser heating for the cells that lie below the skin surface. Moreover, for deep cell, the point heating style can bring the most desirable outcome. Results describe in this paper could be useful for researchers and doctors to optimize the treatment procedure, even protocols.

Keywords: FEM; Bioheat Transfer; Human Tissue; Pennes Equation; Spatial Heating.



This work is licensed under a [Creative Commons Attribution-NonCommercial 4.0 International](https://creativecommons.org/licenses/by-nc/4.0/)

1. Introduction

Prior acknowledgment of the temperature distribution of thermal therapy could help optimize treatment procedures and take necessary precautions for probable danger during therapy. Undoubtedly experimental study is most welcome in this field. However, as human subject involves, the experimental approach often became very difficult to perform and result in a hazardous situation. Moreover, it is time-consuming and needs costly equipment setup. Hence mathematical modeling is preferred in that area instead of clinical trials. But the complexity of modeling biological systems and treatment procedures makes it so tough in practice even impossible. That's why computational modeling of the biological bodies has received considerable attention in the research community in the past decade. Rapid advancement in computational technology, which enables better accuracy with less computational cost, added a new era to this progress. Moreover, due to its simplicity in use and low cost, it is widely used in simulation of biomedical problems. With the help of computer technology and mathematical model, it is possible to calculate and visualize the stationary and transient temperature inside biological bodies during thermal therapy.

Heat transfer in living tissue has become a very interesting topic for scientists and engineers because of its broad application in bioengineering and designing of medical protocols. Many therapeutic applications need the proper thermal description of the human body. Not only that, but many medical operations also rely on engineering methods to determine the safety and risk level involved in many surgeries. At present, mathematical modeling of Bioheat transfer is widely used in treating tumors, cryosurgery, laser eye surgery, and many other applications. The

success of hyperthermia treatment much depends on the proper knowledge of heat transfer in blood perfused tissue [1]-[2].

Over the years, several mathematical models have been developed to describe the heat transfer within living biological tissues. The most widely used bio-heat model was introduced by Pennes in 1948 [3]. Pennes Bio-heat-equation has been widely used to approximate the overall temperature distribution in tissue. The Pennes model was initially used to predict the temperature distribution in the human forearm. Due to its simplicity (uniform thermal conductivity, blood perfusion, and metabolic heat generation), it was implemented in various biological research work such as for cancer hyperthermia, cryosurgery etc. Therefore, to obtain a flexible solution that can solve similar problems is very desirable. Reports on the analytical and numerical solutions of the bio-heat transfer problem are found in the literature. In some analytical cases, sinusoidal heat flux [4] and sometimes cooling of the skin [5] were considered as boundary conditions. In some numerical analysis, sinusoidal surface heat flux was used as boundary condition [6]. Researches related to the bio thermos- mechanical were reviewed in [7]. Monte Carlo method was used to solve the multidimensional problem in [8]. The result of boundary element method and finite element method for the numerical solution of the steady state bio-heat transfer model of the human eye were compared in [9]-[10]. The finite element method was used for the thermal-magneto static analysis in biological tissues in [11]. Some commercial software includes bio-heat transfer functions with limited boundary conditions. It is quite difficult to have the temperature profile of a particular point or a line within the biological tissue with different time intervals using that software. The development of a free finite element code of bio-heat

equations can meet the purpose. The objective of this research is to develop a one dimensional finite element code for the solution of both steady and transient bio-heat equation. The popular Crank-Nicolson method was used in time discretization of the transient analysis. The developed finite element code was used to simulate the thermal response of tissue during cancer hyperthermia, laser surgery, tissue heating with a hot disk, and point heating. Moreover, time-dependent spatial and surface heating were incorporated. The effect of surface heating, step heating, sinusoidal heating, and point heating was thoroughly investigated. The temperature profile for all cases is found with valuable information for the physicians and researchers.

2. Bio Heat Transfer

For the study of bio-heat transfer in human tissue, the most useful one is Pennes equation which can be expressed as

$$k \frac{\partial^2 T}{\partial x^2} + \omega_b \rho_b c_b (T_a - T) + Q_m + Q_r = \rho c \frac{\partial T}{\partial t} \quad (1)$$

For steady state case the Eq. 1(a) is reduced as

$$k \frac{\partial^2 T}{\partial x^2} + \omega_b \rho_b c_b (T_a - T) + Q_m + Q_r = 0 \quad (2)$$

Where ρ , c , k are respectively the density, the specific heat, and the thermal conductivity of the tissue; ρ_b , c_b denote density, and specific heat of blood, respectively. The ω_b is the blood perfusion, T_a the known arterial temperature, and $T(x, t)$ is the unknown tissue temperature. Where Q_m is the metabolic heat, and $Q_r(x, t)$ is the heat source due to spatial heating.

Let the one dimensional problem of length L , where the skin surface is defined at $x = 0$ and the body core at $x = L$. The constant body core temperature is defined as T_c , h_0 is the ambient heat convection coefficient between the skin surface and the surrounding air and T_0 is the ambient temperature. At the skin surface ($x = 0$), the thermoregulation between the skin and ambient air is governed by the thermal convection between air and skin. While as the tissue temperature remains constant within a narrow limit, i.e., 2-3 cm, the boundary conditions at the body core is considered as temperature boundary conditions. Thus the boundary conditions for this particular 1-D problem can be written as:

$$-k \frac{\partial T(x)}{\partial x} = -h_0 [T_0 - T(x)] \quad \text{at } x = 0 \quad (3)$$

$$T = T_c \quad \text{at } x = L \quad (4)$$

In some cases, force convection cooling is applied at the skin surface to remove excessive heat from the skin surface, in such case the boundary condition at the skin surface is defined as

$$-k \frac{\partial T(x)}{\partial x} = -h_f [T_f - T(x)] \quad \text{at } x = 0. \quad (5)$$

In some cases, the boundary condition is time dependent. So time dependent boundary conditions can be expressed as

$$-k \frac{\partial T(x)}{\partial x} = Q(t) \quad \text{at } x = 0. \quad (6)$$

Here $Q(t)$ is the time dependent heat flux.

2.1 Finite element discretization

The first step of the finite element discretization is to develop a weak form that is a weighted integral statement and

is equivalent to both the governing differential equation as well as a certain type of boundary condition. The simplest form of the Eq. (1) is

$$k \frac{\partial^2 T}{\partial x^2} - BT + q = \rho c \frac{\partial T}{\partial t} \quad (7)$$

Where $B = \omega_b \rho_b c_b$ and $q = BT_a + Q_m + Q_r$. The weak form of the differential equation (applying the Weighted Residual method) is derived as

$$\int_{x_a}^{x_b} \left[W \rho c \frac{\partial T}{\partial t} + k \frac{\partial T}{\partial x} \frac{\partial W}{\partial x} - BWT - Wq \right] + (WQ)_{x_a} + (WQ)_{x_b} = 0 \quad (8)$$

Where W is the weighted function, and Q is the secondary variable. A linear element is considered is this model whose temperature function is expressed as

$$T_h^e(x) = \sum_{j=1}^2 \varphi_j^e(x) T_j^e \quad (9)$$

Using the linear approximation of Eq. (9) finally a linear system was derived of the following form

$$[C]\{\dot{T}\} + [K]\{T\} = \{q\} + \{Q\} \quad (10)$$

Where C is the capacitance matrix, K is heat conductive matrix and T is unknown temperature and others are known vectors.

2.2 Time Discretization Scheme

A simple time integration scheme for the Eq. (10) is derived by assuming that C and K are constant. In such case, the matrix differential equation can be discretized with response to time as

$$C \frac{T^{n+1} - T^n}{\Delta T} + \alpha K T^{n+1} + (1 - \alpha) K T^n = Q + q \quad (11)$$

Where T^{n+1} and T^n are the vectors of unknown nodal values at times $n\Delta T$ and $(n + 1)\Delta T$, respectively and α is the weighting factor. The α must be chosen in the interval between 0 and 1. When the value of α is considered 0.5, the process is called the popular Crank-Nicolson method. The discretized Eq. (11) can be written as:

$$\left(C \frac{1}{\Delta T} + \alpha K \right) T^{n+1} = \left[C \frac{1}{\Delta T} - (1 - \alpha) K \right] T^n + Q + q \quad (12)$$

The Eq. (12) was solved using an iterative procedure. The initial temperature is known and then the temperature of the next step is calculated from the solution of Eq. (12) through the Gauss elimination technique.

2.3 Boundary Conditions and Input Parameters

Throughout the study at $X=L$, the temperature boundary condition is used.

However, depending upon the types of heating boundary condition (3), (5) and (6) is used at $X=0$.

In section 3.2, 3.3, 3.8, and 3.9 boundary condition (3) is used at the skin surface. Heat flux boundary condition Eq. (6) is used in sections 3.4 and 3.5 at $X=0$. Where the force convection boundary condition Eq. (5) is used in sections 3.6 and 3.7. The input parameters used in this study is summarized in Table 1 [12].

Table 1 Input Parameters.

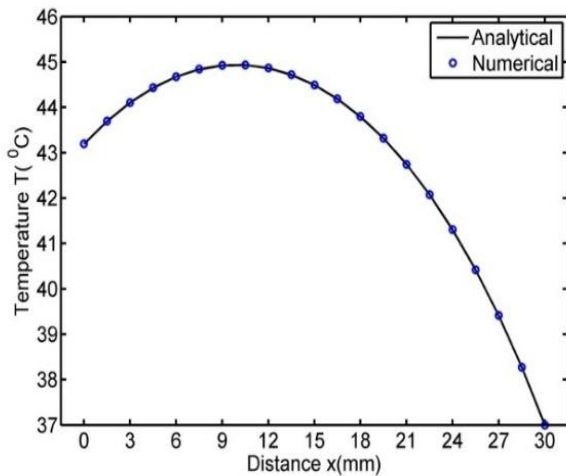
Parameters	Value
Thermal conductivity (k)	0.5 w/m ²
Convection Coefficient (h _o)	10 w/m ²
Forced convection coefficient (h _f)	100 w/m ²
Environmental Temperature (T ₀)	25 °C
Temperature of the Artery (T _a)	37 °C
Body core temperature (T _c)	37 °C
Metabolic heat generation (Q _m)	33800 w/m ²
Density of blood (ρ _b)	1000 kg/m ³
Density of tissue (ρ)	1000 kg/m ³
Specific heat of blood (c _b)	4200 J/kg.°C
Specific heat of tissue (c)	4200 J/kg.°C
Blood perfusion (ω _b)	0.0005 ml/s/ml

3. Results and Discussion

For the simple thermal analysis, from the skin surface to tissue body is enough to consider. So to avoid the computational complexity, a 1D tissue of length (L) of 30 mm is considered as a computational model.

3.1 Code Verification

Fig. 1 shows a comparison between numerical result and the analytical result obtained from [12] for the steady state case considering the Eq. (3-6). The comparison shows a better agreement. The boundary conditions are defined as describe in Eq. (3) and Eq. (4).

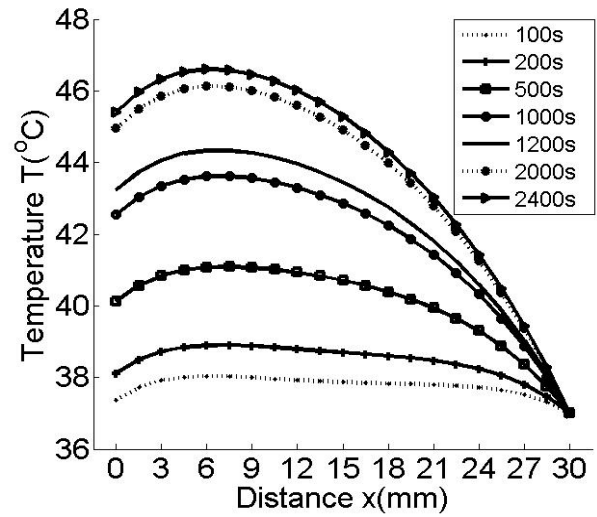
**Fig. 1** Comparison with analytical solution.

This figure shows that initially, tissue temperature increases along with distance due to metabolism, but after attaining the highest value, it decreases towards the body core as temperature boundary condition is applied to the body core. Here the maximum temperature is 45°C, which is located about 11 mm below the skin surface.

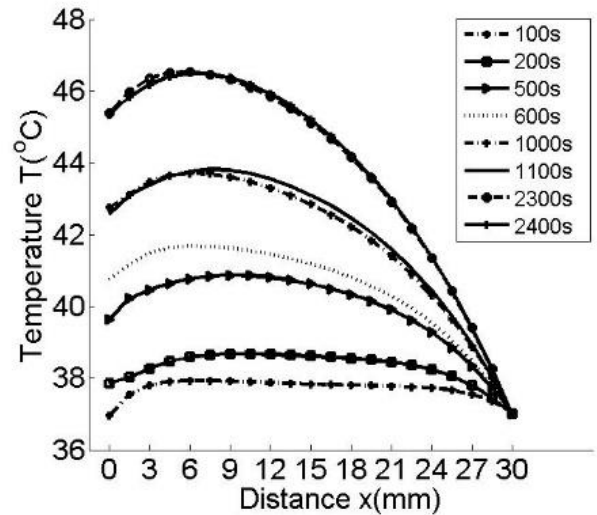
3.2 Spatial Heating

Laser and microwave therapy are some of the most widely used non-invasive techniques to destroy malignant cells. In this section, we aim to know the temperature distribution of human tissue during heating by laser or microwave.

In case of heating by laser and microwave, the heat absorption rate can simply be approximated by Beers Law, which can be expressed as $Q_r = \eta P_o(t)e^{-\eta x}$ in which heat flux decays exponentially with respect to distance from the skin surface [13]-[15]. Here $P_o(t)$ is the time-dependent heating power on the skin surface, and η is the scattering coefficient. Since $P_o(t)$ and η vary from one apparatus to another, so it is important to know the influence of these parameters on tissue temperature. $P_o(t)$ can be either constant and time-dependent. In our study, we have considered both cases.



(a)



(b)

Fig. 2 Temperature distribution at different times; ($\eta = 200 \text{ m}^{-1}$), (a) $P_o(t) = 250 \text{ W/m}^2$, (b) $P_o(t) = 250 + 200\cos(0.02t) \text{ W/m}^2$.

Fig. 2 depicts the transient temperature at different times when tissues subject to two different spatial heating. **Fig. 2 (a)** shows the case of constant spatial heating and while **Fig. 2 (b)** is for sinusoidal spatial heating. In both cases, at the early stage, the tissue temperature increases along with the distance from the skin surface due to external heating, but later it decreases towards the body core. Moreover, there is an inter-cross

between temperature curves at different times in Fig. 2 (b), which indicates the oscillation of the temperature inside the tissue due to sinusoidal spatial heating. These figures also reveal that the temperature within the tissue increases along with time and finally reached the steady state condition. Here the maximum temperature is about 47°C , and that lies 7 mm below the skin surface.

3.3 Effect of Scattering Co-efficient

Fig. 3 shows the effect of the scattering coefficient, where Fig. 3 (a) shows the result for constant heating, and Fig. 3 (b) depicts the result for sinusoidal heating. In both cases, the larger coefficient results in a higher temperature. Moreover, in the case of sinusoidal spatial heating, the larger coefficient returns higher amplitude. Fig. 3 (b) indicates the sinusoidal effect. Fig. 3 (a) shows that after about 3000 seconds (approximately), tissue temperature begins to stabilize.

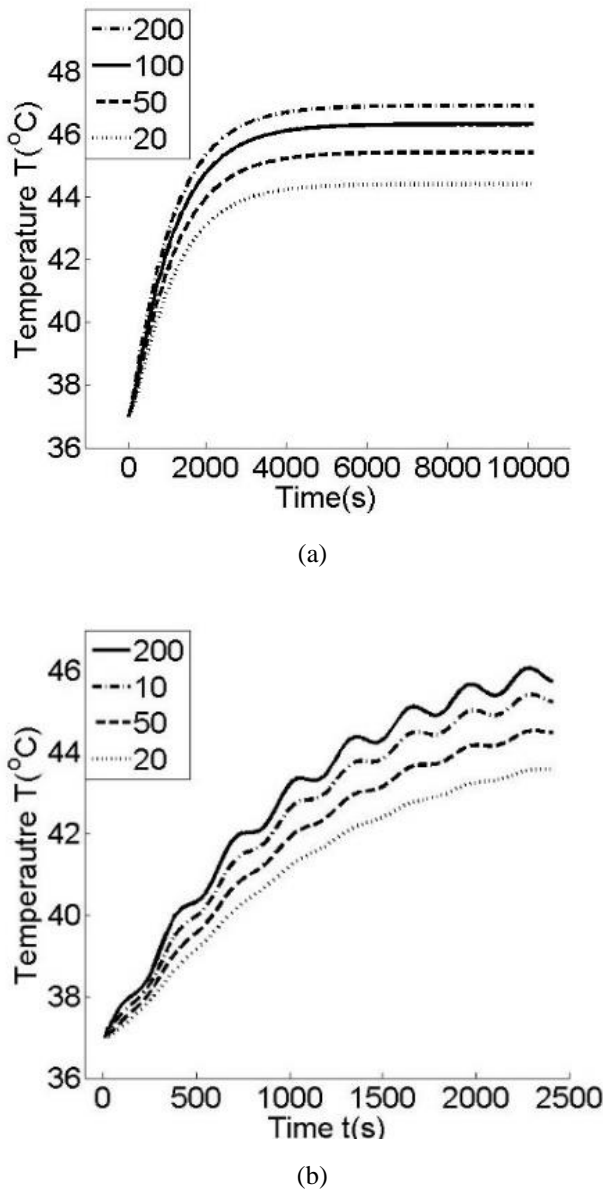


Fig. 3 Effect of scattering coefficient on temperature response at skin surface ($f(t) = 0$); (a) $P_0(t) = 250 \text{ W/m}^2$; (b) $P_0(t) = 250 + 200\cos(0.02t) \text{ W/m}^2$.

3.4 Surface Heating

Heating with a hot plate or pad is a traditional approach to retain from pain. Depending upon the temperature and thermal properties of heating disk, this approach can be used for cell repair or to destroy affected cells. In this section, we analysed the thermal behaviour of living tissue subjected to time-dependent surface heat flux. Both constant and step heating are considered in this study. In constant heating, human tissue is heated with a heating pad at a constant rate. In step heating after heating for a certain period heat source is removed and allows it to cool. Results are calculated at different heat flux and time. Here Eq. 3(a) is used for skin surface boundary conditions.

Constant Heating: The calculated tissue temperature for constant surface heating is shown in Fig. 4 (a) at different heat flux. And skin temperature at different times, along with the distance from the skin surface, is shown in Fig. 4 (b). From Fig. 4 (a) higher heat flux results in a higher temperature, and temperature increases as time increases. At the early stage, temperature increases rapidly, but as time increases, increasing rate decreases and tends to be stabilized. From Fig. 4 (b) it is clear that temperature decreases towards the body core.

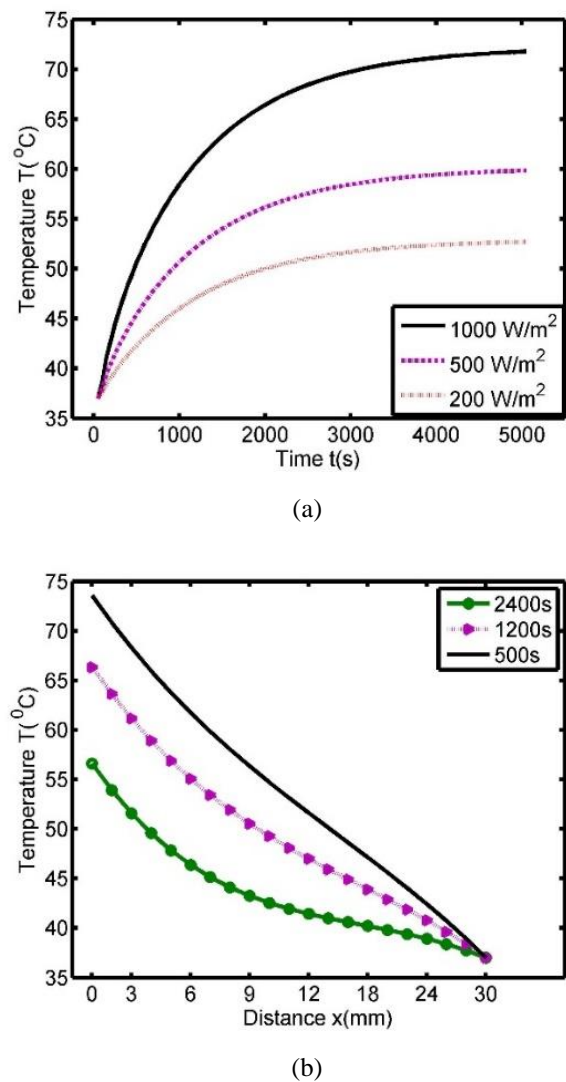
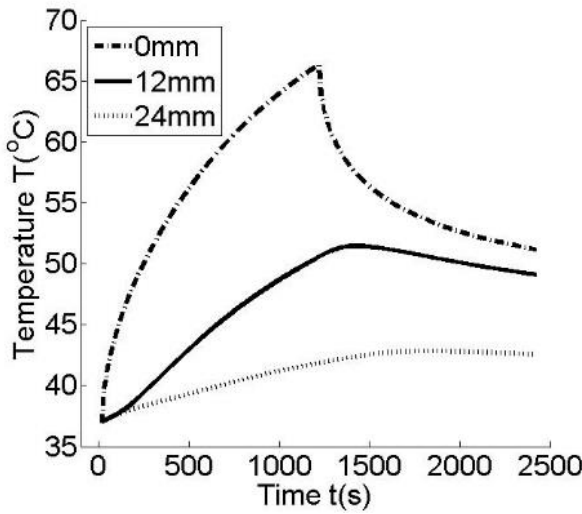


Fig. 4 Effect of surface heat flux to the skin surface temperature response.

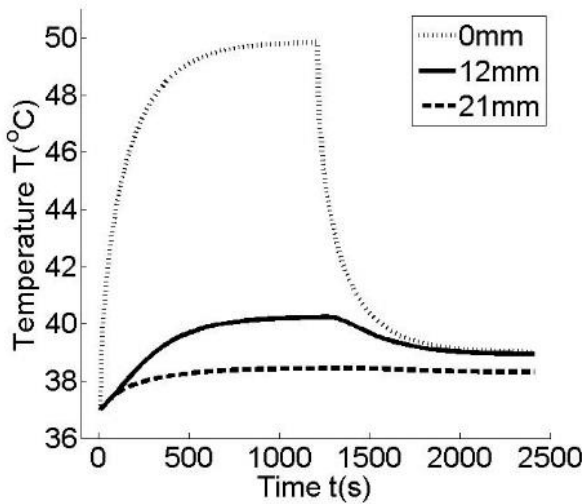
Step Heating: In this case, after heating for 1200 seconds the heat source is removed. In this section, temperature distribution at three different locations is obtained over time. It is very useful in eye surgery via a single laser pulse due to a flash fire, heating using a hot plate for a short period of time [10]. The heating power used in this particular type of investigation is expressed as

$$Q(t) = \begin{cases} 1000 \frac{W}{m^2}, & t \leq 1200 \text{ s} \\ 0 \frac{W}{m^2}, & t > 1200 \text{ s} \end{cases} \quad (13)$$

The transient temperature at three different locations of the skin is shown in Fig. 5. Where $Q_r=0$, in Fig. 5. The result also carried out for two different value of blood perfusion $\omega_b=0.0005 \text{ ml/s/ml}$ and $\omega_b=0.004 \text{ ml/s/ml}$.



(a)



(b)

Fig. 5 Transient temperature at three positions ($Q_r=0$); (a) $\omega_b=0.0005 \text{ ml/s/ml}$; (b) $\omega_b=0.004 \text{ ml/s/ml}$.

Both figures show that as time increases, temperature also increases, but after 1200 seconds when the heat source is removed, tissue temperature decreases as time passes. Moreover, these figures show us the effect of blood perfusion

in surface heating. Also the higher blood perfusion results in lower temperature and quick temperature loss (after 1200 seconds when $Q(t)=0$). This happens as a higher blood flow rate carried away excess heat. Such information is valuable in thermal comfort analysis. In practice, the temperature of the surrounding fluid temperature and duration should be in the safe range. A high temperature or long durable process may encounter pain, even burning of the skin.

3.5 Effect of Heating Frequency and Blood Perfusion

The calculated result for different heating frequency and blood perfusion is shown in Fig. 6 subjected to sinusoidal surface heating. The sinusoidal heating at the skin surface can be expressed as

$$Q(t)=q_0+q_w \cos(\omega_1 t) \quad (14)$$

Where q_0 and q_w are the constant terms, and the oscillation amplitude of sinusoidal heat flux and ω_1 represents the heating frequency.

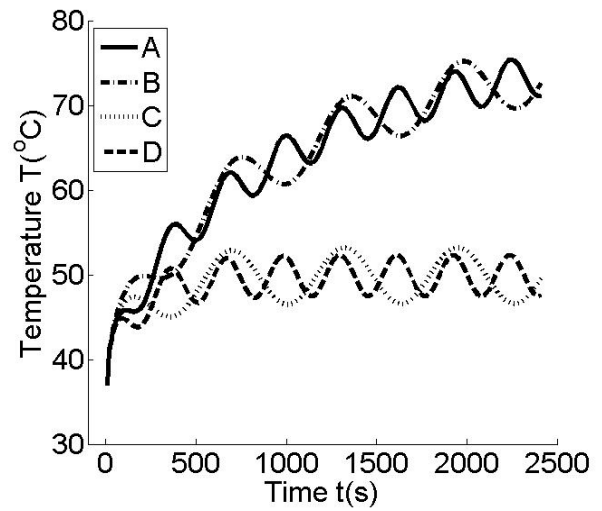


Fig. 6 Effect of heating frequency and blood perfusion on sinusoidal surface heat flux.

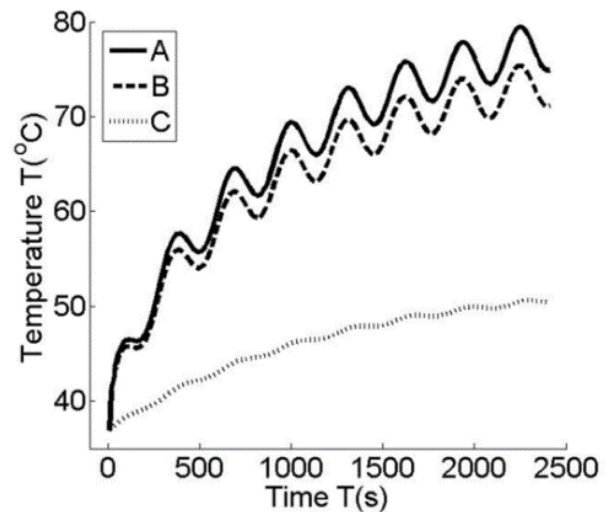


Fig. 7 Different heating condition and its impact on skin surface temperature.

In Fig. 6 curves A and B, we use blood perfusion as 0.0005, where in curve C & D it is 0.004. While in curve A and C, we use a heating frequency of value, 0.02 were in B & D, it is 0.01. From these figures, we can say that high blood perfusion results in lower temperatures where temperature response under two different heating frequencies almost negligible.

The calculated tissue temperature result subject to simultaneously surface and spatial heating is shown in Curve A of Fig. 7. While Curve B represents a single sinusoidal surface heating ($Q_r=0$), and curve C represents only sinusoidal spatial heating ($f_1(t)=0$). The applied surface and spatial heating are $Q(t)=1000+500\cos(0.02t)$ W/m² and $P_o(t)=250+200\cos(0.02t)$.

However, Fig. 8 illustrates the impact of frequencies of surface heating. Here the applied surface and spatial heating are $Q(t)=1000+500\cos(0.02t)$ W/m² and $P_o(t)=250+200\cos(0.01t)$ respectively. In curve A, we applied simultaneously sinusoidal surface and spatial heating. Curve B represents a single sinusoidal surface heating ($Q_r=0$) when curve C represents only spatial heating ($f_1(t)=0$).

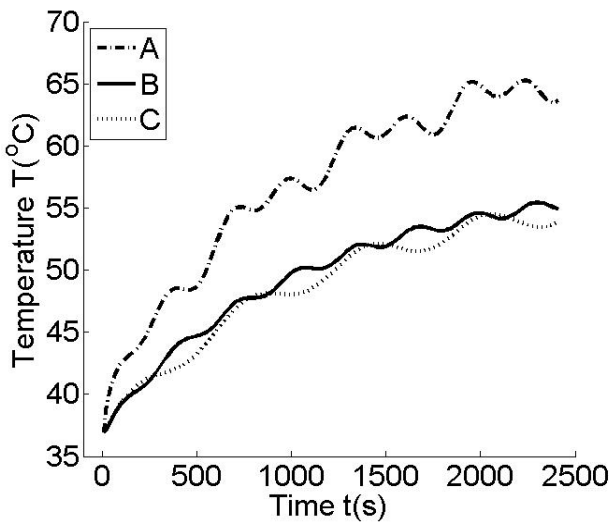


Fig. 8 Temperature distribution at different heating frequency.

In curve A of Fig. 8, the frequency of surface heating and spatial heating was the same, and thus, due to the same frequency, the resultant temperature appears having the same frequency as external heating. However, in curve A of Fig. 8, different heating frequency was applied to spatial and surface heating; that's why irregular frequency has appeared in tissue temperature.

3.6 Impact Forced Convection Boundary Condition

In this section, we concentrate on temperature profiles under different kinds of surrounding medium classified by their temperature. Fig. 9 depicts the tissue temperature distribution under different cooling medium temperature. Here force cooling significantly reduces the skin surface temperature. Moreover, lower cooling medium temperature results in lower skin surface temperature. However, the effect of forced cooling is negligible for the deep tissues, as shown in Fig. 9, the

temperature of the cells over approximately $x=12$ mm line remains changeless for different cooling temperature.

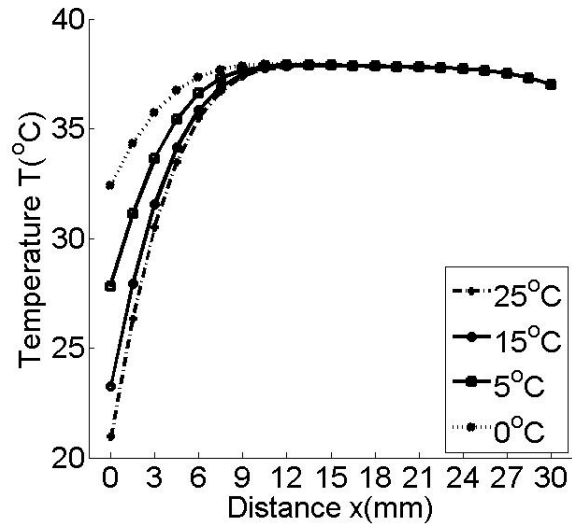


Fig. 9 Influence of cooling medium temperature on tissue temperature.

Using a cooling medium on the skin surface may be a good approach during hyperthermia treatment as it can reduce the skin temperature even below the core temperature, which may result in hypothermia. Hence, concentration should be given selecting proper cooling medium. Here the force convection coefficient of the cooling medium is considered as 100 W/(m². °C).

3.7 Point Heating

Treating deep tumors- located at kidney, lung, or rectum- it is very difficult to adopt surgical treatment. In such a case, point heating can be an alternative to surgery due to its ability to treat a tumor with a defined volume. In such a case, the total heating power is deposited at the tumor site with the help of a microwave probe, radio-frequency probe etc. In this heating type, the target region is heated more than 50°C within few minutes. This heating is very beneficial in the case of thermal ablation when a target tissue is destroyed, injecting thermal energy at the tumor site [5],[6]. There is an inverse relationship between elevated temperature and exposure duration. For the same amount of tissue necrosis, the high temperature needs low exposure duration. On the contrary, the low temperature needs high exposure duration. So for effective treatment, we need to know the required temperature and exposure duration precisely. Moreover, in some cases, to protect the skin surface cells from excess heat, the cooling medium is used on the skin surface during treatment, which is a very efficient approach to reduce the skin surface temperature. In this investigation, we calculate the tissue temperature at different times, cooling medium properties, and heating power. To deposit total heating power at the desired site, we use the expression of the external heating as [12],[13].

$$Q_r(x,t)=P_1(t)\delta(x-x_0) \quad (15)$$

Where $P_1(t)$ is the point, heating power, and $\delta(x-x_0)$ is the Dirac delta function. It has a value 1 at our desired point (x_0), and at all other points, its value is 0. That's why it allows depositing total heating power at the tumor site. Where x_0 is the distance of tumor site from the skin surface. Here we consider the distance of the tumor site from the skin surface is 21 mm (x_0). In this case, convection boundary condition is applied ($h_f=100 \text{ W}/(\text{m}^2\cdot^\circ\text{C})$ and $T_f=15^\circ\text{C}$) at the skin surface.

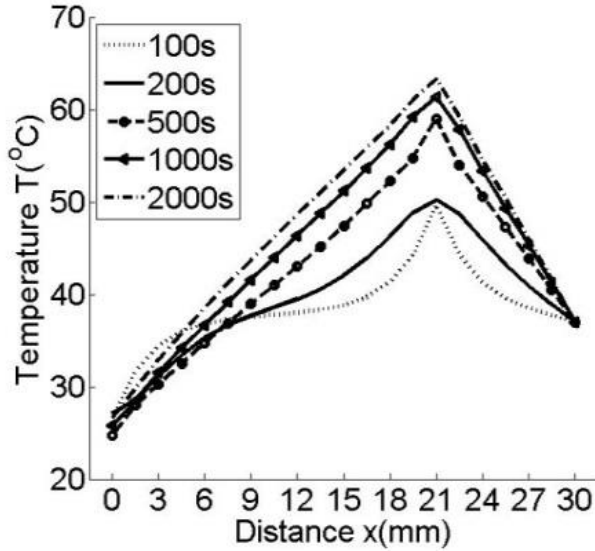


Fig. 10 Impact of point heating on tissue temperature distribution.

In Fig. 10, temperature distribution at different times is shown where point heating with a point heat source of $P_1(t)=2500 \text{ W}/\text{m}^2$ is applied. This figure demonstrates that due to point heat source, the position of the maximum temperature remains constant at the site of the point source at different times.

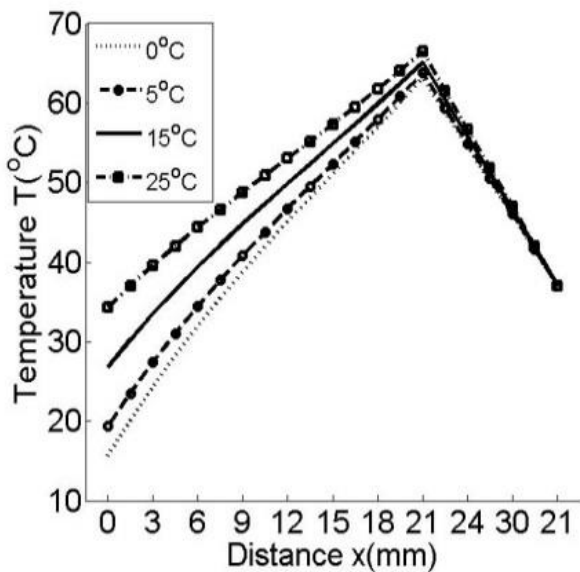


Fig. 11 Influence of cooling medium temperature to steady state temperature distribution.

In Fig. 11 the temperature response under different temperatures of cooling fluid is analysed where in Fig. 12 influence of tissue temperature under different heating power is shown. Both results are computed for the steady state condition. In Fig. 11, point source of $P_1(t)=2500 \text{ W}/\text{m}^2$ is used. Fig. 11 shows that the magnitude and position of the highest steady state temperature are changeless at different cooling medium temperature. It reduces skin surface temperature considerably.

From Fig. 12 it is clear that higher power of the point heat leads to a higher temperature. Moreover, tissue temperature sensitivity due to point heating power decreases along with the distance from point heat source.

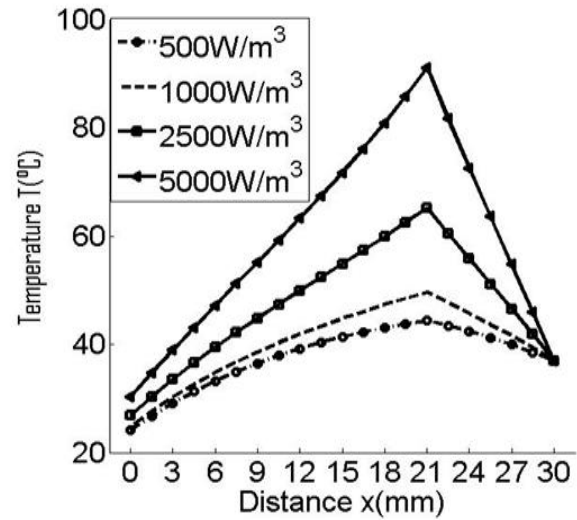


Fig. 12 Impact of point heating power on steady state temperature distribution.

3.8 Tissue Temperature Fluctuation under Stochastic Cooling Medium Temperature

Earlier, we consider the surrounding fluid temperature as constant. However, practically surrounding fluid temperature does not remain constant; rather, it fluctuates over time. So it is necessary to know the impact of such stochastic behavior. For this purpose, we use the following expression for flowing medium temperature.

$$T_e = T_f + \varepsilon(t) \quad (16)$$

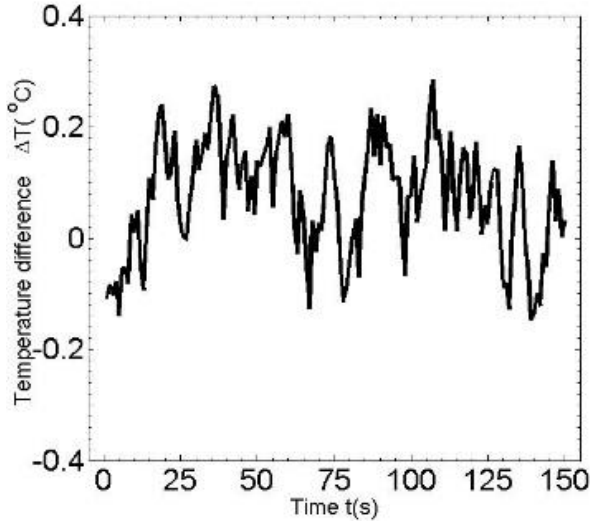
Where $\varepsilon(t)$ the stochastic variance in T_e and T_f is the equilibrium value if the environmental temperature. This variance gives the environmental temperature a stochastic value. We assume

$$\varepsilon_i = \lambda_i(0.05 - \sigma_i) \quad (17)$$

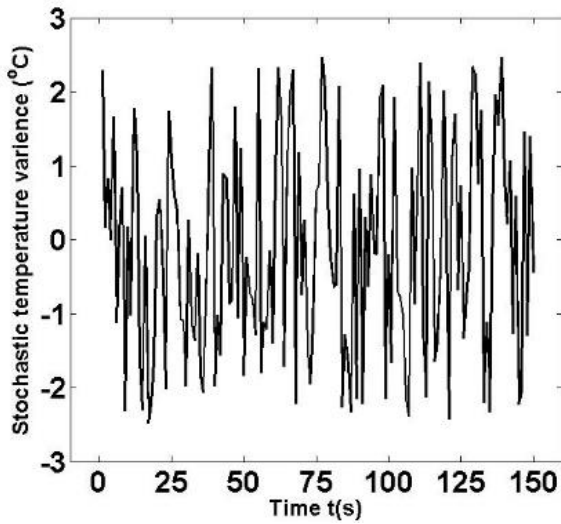
Where ε and t is the stochastic variance in environmental temperature and the discrete-time, respectively; σ_i is the random number between 0 and 1.

Fig. 13 and Fig. 14 depict the influences of variance in environmental temperature with different convection coefficient between the cooling medium and skin surface. Fig.

13 (a) and **Fig. 14 (a)** shows the tissue temperature fluctuation over time where **Fig. 13 (b)** and **Fig. 14 (b)** shows the fluctuation of stochastic variance. These figures demonstrate that due to irregular cooling medium temperature, the tissue temperature fluctuates within a certain range. Moreover, the frequency of the tissue temperature is much smaller than that of the stochastic variance. It may be noticed that as convection coefficient gets larger the temperature fluctuation magnitude also increases slightly.



(a)



(b)

Fig. 13 Impact of stochastic temperature variance on tissue temperature ($h_f=100 \text{ Wm}^{-2}$).

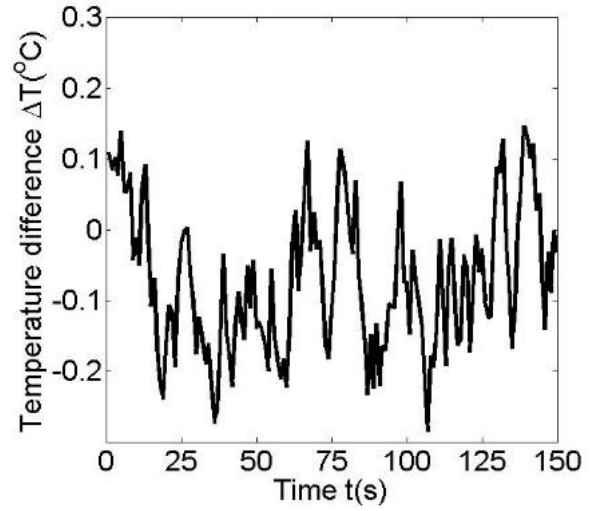
3.9 Tissue Temperature Fluctuation Due to Stochastic Heating

In this section, we will analyze about stochastic heating, which may be encountered for biological rhythm or stochastic external heating in hyperthermia treatment. This case corresponds to the spatial heating of the following type.

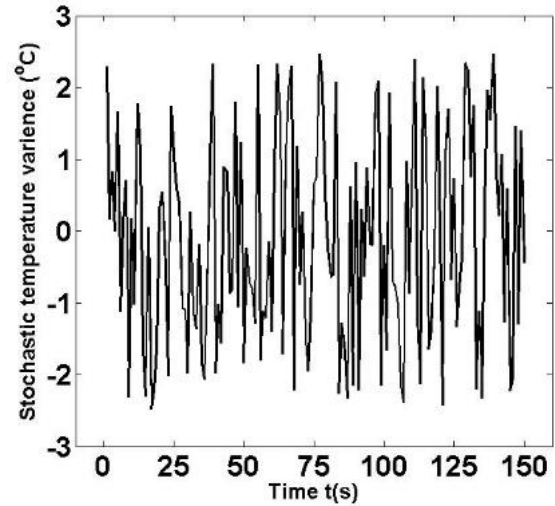
$$Q_r = Q'_m(t) \quad (18)$$

Where $Q'_m(t)$ is the stochastic variance in metabolic rate, and in the initial state, the metabolic rate was considered as constant Q_m . Here we assumed that

$$Q'_m(t) = \lambda_q(0.5 - \sigma_i) \quad (19)$$



(a)

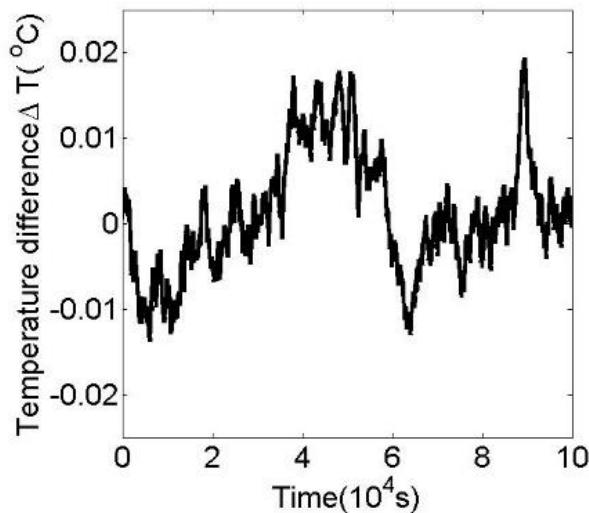


(b)

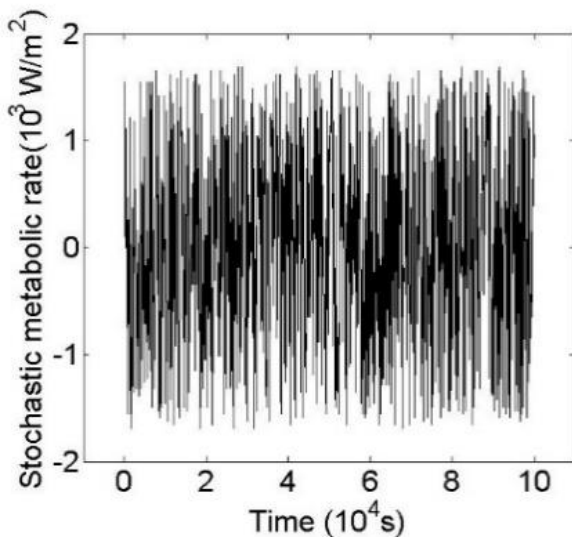
Fig. 14 Impact of stochastic temperature variance on tissue temperature ($h_f=25 \text{ Wm}^{-2}$).

Where Q'_m and t is the stochastic variance in metabolic heat generation and the discrete-time respectively; σ_i the random number between 0 and 1 and t is the discrete stochastic variance in environmental temperature. And λ_q is a constant, which was regarded as $Q_m/10$ in this study.

The calculated results are shown in **Fig. 15** which indicates that due to stochastic heating the temperature fluctuates within a small range ± 0.1 . **Fig. 15 (a)** shows the tissue temperature fluctuation over time where **Fig. 15 (b)** shows the fluctuation of stochastic variance. Section 4.8 and Section 4.9 clearly indicates that the biological body, tends to keep its temperature balance.



(a)



(b)

Fig. 15 Influence of variance in metabolic rate on tissue temperature.

4. Summary

In this paper, a one dimensional Finite Element Model was developed to know the temperature profile inside the human tissue subject to numerous heating pattern i.e., spatial heating, surface heating, point heating, and stochastic heating. Effect of heating frequency, blood perfusion, and scattering coefficient are also discussed briefly. Which can be used in parameter estimation. It is found that for destroying a target cell point, heating is more suitable than other heating as it increases the temperature of the target region, and it has a relatively low impact on nearby unaffected cells. Moreover, a higher scattering coefficient leads to a higher temperature, where higher blood perfusion leads to lower temperature. As heating apparatus such as laser or microwave may have different power and scattering coefficient. The results obtained in this paper can be used to select a suitable apparatus. During treatment, fluctuation of environmental fluid temperature may be out of consideration as its impact on tissue temperature is almost negligible, as shown in stochastic heating. The different heating

styles used for investigation in this study are generally carried out in clinical trials. Hence results described in this paper could be beneficial to predict the treatment outcome before the treatment. This will help to detect the possible risk as well as increasing the effectiveness of the treatment. Moreover, the developed Finite Element Model and computer code can be further use to solve more practical bio-heat transfer problems.

References

- [1] Kasevich, R.S., McQueeney, J.F. and Crooker, R.H., KASEVICH ASSOC Inc, 1988. *Method and apparatus for hyperthermia treatment*. U.S. Patent 4,776,086.
- [2] Khanafer, K. and Vafai, K., 2009. Synthesis of mathematical models representing bioheat transport. *Advances in numerical heat transfer*, 3, pp.1-28.
- [3] Pennes, H.H., 1948. Analysis of tissue and arterial blood temperatures in the resting human forearm. *Journal of applied physiology*, 1(2), pp.93-122.
- [4] Shih, T.C., Yuan, P., Lin, W.L. and Kou, H.S., 2007. Analytical analysis of the Pennes bioheat transfer equation with sinusoidal heat flux condition on skin surface. *Medical Engineering & Physics*, 29(9), pp.946-953.
- [5] Shen, W., Zhang, J. and Yang, F., 2005. Modeling and numerical simulation of bioheat transfer and biomechanics in soft tissue. *Mathematical and Computer Modelling*, 41(11-12), pp.1251-1265.
- [6] Xu, F., Lu, T.J. and Seffen, K.A., 2008. Biothermomechanical behavior of skin tissue. *Acta Mechanica Sinica*, 24(1), pp.1-23.
- [7] Deng, Z.S. and Liu, J., 2002. Monte Carlo method to solve multidimensional bioheat transfer problem. *Numerical Heat Transfer: Part B: Fundamentals*, 42(6), pp.543-567.
- [8] Ooi, E.H. and Ang, W.T., 2008. A boundary element model of the human eye undergoing laser thermokeratoplasty. *Computers in Biology and Medicine*, 38(6), pp.727-737.
- [9] Ooi, E.H., Ang, W.T. and Ng, E.Y.K., 2007. Bioheat transfer in the human eye: a boundary element approach. *Engineering Analysis with Boundary Elements*, 31(6), pp.494-500.
- [10] Hwang, S.C. and Lemmonier, D., 1970. Coupling numerical solution of bio-heat transfer equation and Maxwell's equations in biological tissues during hyperthermia. *WIT Transactions on Biomedicine and Health*, 2.
- [11] Reddy, J. N., 2006. *An Introduction to the Finite Element Method*, 3rd edition, McGraw Hill, Inc.
- [12] Deng, Z.S. and Liu, J., 2002. Analytical study on bioheat transfer problems with spatial or transient heating on skin surface or inside biological bodies. *J. Biomech. Eng.*, 124(6), pp.638-649.
- [13] Karaa, S., Zhang, J. and Yang, F., 2005. A numerical study of a 3D bioheat transfer problem with different spatial heating. *Mathematics and Computers in simulation*, 68(4), pp.375-388.
- [14] Sardari, D. and Verga, N., 2011. *Cancer treatment with hyperthermia*. INTECH Open Access Publisher.
- [15] Cheung, A.Y. and Neyzari, A., 1984. Deep local hyperthermia for cancer therapy: external electromagnetic and ultrasound techniques. *Cancer Research*, 44(10 Supplement), pp.4736s-4744s.

Indexed by:

Google Scholar



Volume 01 Issue 02

DOI: <https://doi.org/10.38032/jea.2020.02>